

THE STRUCTURE AND PHYSICAL PARAMETERS OF CHALCOGENIDE GLASS-LIKE SEMICONDUCTORS OF SYSTEM As- Ge – Se

S.I. MEKHTIYEVA, A.I. ISAYEV, R.I. ALEKBEROV, H.I. MAMEDOVA
Institute of Physics of Azerbaijan NAS, AZ 1143, H.Javid ave.,131, Baku, Azerbaijan
physics.humay@mail.ru

The parameters of local structure (correlation length and quasi-period in average order region) are defined by carrying out of experiments by X-ray beam diffraction and density of glass-like systems As – Ge – Se. The dependence of physical parameters (density, packing coefficient, compactness, molar volume average value, lone pair electron number, cohesion energy) on average coordination number and R parameter defining the bond character between atoms is established. The compositions corresponding to chemical percolation threshold and also compositions in which the glass state is flexible, highly-stressed and isostatically stressed are established using results of Phillips-Torp and Tichy theories.

Keywords: X-ray beam diffraction, coordination number, cohesion energy.

PACS: 81.05.Gc

INTRODUCTION

The chalcogenide glass-like semiconductors (ChGS) outperform other functional materials in their unique electronic properties used for applications [1 -6]. They are transparent in wide spectral region, have high photosensitivity, optical nonlinearity, high value of refraction index and also they differ from other materials by technological process simplicity at preparation of different details on their base and chemical stability [7 -9]. Advantage of ChGS also is caused by wide region of glass formation, possibility of unlimited doping and chemical composition variation that allows us to change the structure and obtain the material with optimal parameters [1,10- 12]. However, the successful realization of applied tasks requires the obtaining of material with predicted properties and optimal parameters necessary for concrete purpose.

It is known, that macroscopic properties of non-crystalline materials are controlled by micro-structure peculiarities, i.e. short-range order and average one in atom disposition. The change of parameters of short-range and average orders, in particular, coordination number, length and type of chemical bonds, relative part of heteropolar and homeopolar bonds, correlation length and etc. can be achieved by change of chemical composition that should be reflected on structure and electron properties [13 – 14]. ChGS are characterized by existence of structural elements forming the amorphous matrix and also by existence of free volume appearing at technological processes of sample preparation [15 – 22]. The change of chemical composition should lead to change of free volume part in sample that also should influence on electron properties. Thus, the correlation between structure and properties can be established and the possibility of expansion of given material application regions can be revealed by complex investigation of peculiarities of local structure and physical properties.

The investigation of local structure and physical parameters of ChGS of As – Ge – Se system is the goal of the present work. The numerical values of correlation length, quasi-period in average order region, packing coefficient, compactness, average value of atomic volume, average coordination number, limitation number,

cohesion energy are obtained using X-rays diffraction method and density measurement. The choice of the given composition as investigation object is caused by the fact that element atoms including into the given composition differ by the number of valency electrons. According to rule 8-N (atom with N-valency electrons, $N \geq 4$) forms 8-N bonds, i.e. has the 8- N neighbors) the coordination numbers of Ge, As and Se atoms are 4,3 and 2 correspondingly. Such difference in coordination number value allows us to change the glass matrix structure changing chemical composition, i.e. to obtain the glass with both one-, two- and three-dimensional structures. Such change in amorphous matrix should be accompanied by changing of electron properties that allows us to obtain the information on correlation between structure and electron properties and reveal the possibilities of their application.

EXPERIMENT TECHNIQUE AND SAMPLE PREPARATION

Synthesis of ChGS of As – Ge – Se system is carried out in the following sequence: especially pure elementary substances in required atomic percentages are filled into quartz ampoules from which air is evacuated to pressure 10^{-4} millimeter of mercury. After that ampoules are heated up to ~ 900 °C temperature during 3 hours and kept about 12 hours at this temperature. The synthesis is carried out in revolver to supply of sample homogeneity and cooling is carried out in switching off mode. The films by different thickness used in investigations are obtained by thermal evaporation with rate $0,2 \div 0,4$ μ /sec on glassy substrates in vacuum at pressure 10^{-4} millimeter of mercury.

The density (ρ) of investigated ChGS of As-Ge-Se systems is measured by Archimedes principle with use of liquid (water) and it is calculated using the following formula:

$$\rho = \left[\frac{w_0}{(w_0 - w_L)} \right] \rho_L \quad (1),$$

where w_0 and w_L are material heights in air and liquid (in water). Liquid (water) density ρ_L at room temperature is

1gr/cm³. The measurement accuracy isn't less than $\pm 0.02\text{gr/cm}^3$.

The investigations of aggregate state, local structure of synthesized substances and evaporated films are carried out by X-ray structural analysis on power diffractometer D8 ADVANCE (Bruker, Germany) in mode 40kV, 40mA, $0 < 2\theta < 80^\circ$. The diffraction pictures are analyzed using the special program Evaluation for the definition of such parameters of diffraction maximum as their square, amplitude, scattering angle 2θ and full width at half maximum ΔQ (FWHM).

EXPERIMENTAL RESULTS AND THEIR DISCUSSION

The intensity curves of X-ray beam diffraction in thermally evaporated films of As-Ge-Se system with different content of composite elements are shown in fig.1. The wide maximums observed in diffraction picture evidences on their amorphism. As it is seen from the figure corresponding to intensity distribution of X-ray diffraction of investigated ChGS as to majority of glasses [22 – 26] the so-called first sharp diffraction peak (FSDP) differing from other ones by anomalous dependence on temperature and pressure is observed.

FSDP characteristics defined from graph (fig.1) and calculated with the help of scattering vector Q_1 ($Q_1 = 4\pi \sin \theta / \lambda$, wavelength of X-rays $\lambda = 1,54056\text{\AA}$), corresponding to FSDP position and ΔQ

are shown in table 1. Using the given data of FSDP the local structure parameters are defined by formula:

$$d = 2\pi/Q_1 \quad (1)$$

$$L = 2\pi/\Delta Q \quad (2)$$

where d parameter either is called as repetitive distance defining the structural unit sizes or the distance between layers [32 – 34], or as quasi-period of density fluctuation [32 – 34]; L is correlation length, i.e. area size in which the density fluctuation periodicity is maintained. The values of the given parameters are also shown in table 1. As it is seen from the table ΔQ and d values increase and L decreases with the increase of relative part of As and Ge atoms in As-Ge-Se system. Increase of d is probably connected with high value of atomic radius of As and Ge atoms in comparison with Se atoms. Increase of ΔQ and decrease of L evidence on disorder degree increase at such change in chemical composition.

The existence of free volumes in amorphous materials is the recognized fact by all investigators interesting by the given region. The definition of parameter numerical values connected with given structure peculiarities plays the important role in both understanding of electron process mechanism taking place in them and establishment of the regions of their application.

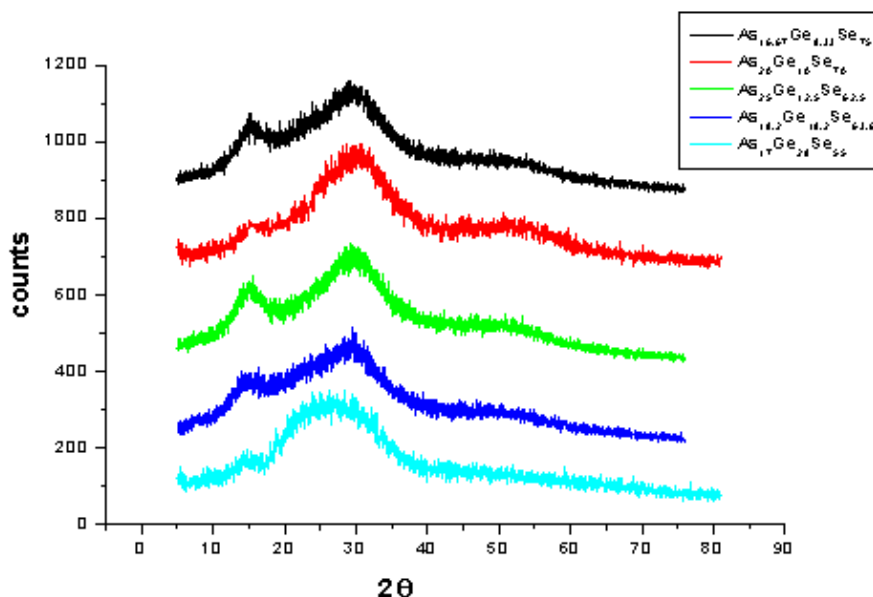


Fig.1. X-ray diffraction patterns of ChGS of As – Ge – Se system.

Table 1.

No	compositions	2θ , grad	Q_1 , \AA^{-1}	$d=2\pi/Q_1$, \AA	D , \AA	ΔQ , \AA^{-1}	$L=2\pi/\Delta Q$, \AA
1	As _{16.67} Ge _{8.33} Se ₇₅	15.27	1.084	5.796	4,72	0.257	24.455
2	As ₂₀ Ge ₁₀ Se ₇₀	15.05	1.092	5.751	4,67	0.242	25.95
3	As ₂₅ Ge _{12.5} Se _{62.5}	15.02	1.066	5.89	4,79	0.324	19.41
4	As _{18.2} Ge _{18.2} Se _{63.6}	14.78	1.049	5.99	4,87	0.238	26.44
5	As ₁₇ Ge ₂₈ Se ₅₅	14.85	1.078	5.826	4,74	0.234	26.838

FSDP origin is usually connected with cluster void model supposed by Elliot [20] according to which the structure regions divided from each other by voids (pores) or region with decreased atomic density are clusters. The contrast in atomic density between correlated-packed clusters and voids causes the FSDP revealing in diffraction picture. According to [7,20] FSDP is caused by correlation between cation structural units, for example of $\text{Ge}(\text{S},\text{Se})_4$ tetrahedron type in $\text{a-Ge}(\text{S},\text{Se})_2$ or AsS_3 (AsSe_3) pyramid one in $\text{a-As}_2\text{S}_3$ ($\text{a-As}_2\text{Se}_3$). Moreover, the analytic formula connecting FSDP position (Q_1) with nanovoid diameter (D)

$$Q_1 = \kappa\pi/D \quad (3)$$

in the case of correlation between tetrahedral structural elements $\kappa = 1.5$ [37]. «ab initio» estimation of Q_1 for different tetrahedral in ordered materials is carried out by application of cluster void model and it is shown that $\kappa = 1.5$ for them. Author of [36] using Eliot model on FSDP nature and experiments by positron annihilation lifetime spectroscopy (PALS) shows that $\kappa = 1.75$ in glass with pyramidal structural elements. Accepting the fact that both types of structural units (As_2Se_3 , GeSe_2) and selenium chain molecule taking under consideration the both coefficients take place in ChGS materials under consideration the nanovoid diameter average values are estimated by formula (3) and results are presented in table 1.

From table it is seen that D value increases with decrease of selenium part in ChGS of As-Ge-Se system. If take under consideration the fact that nanovoids form as a result of atom absence in them then it would be reasonable to connect the increase of their diameter with increase of average atomic radius of the given compositions. Indeed, the concentration increase of arsenic and germanium atoms with big atomic radius causes the increase of material average atomic radius.

Knowing the chemical composition and using the experimental data on density of obtained chemical compositions the numerical values of local structure parameters are calculated.

The average value of coordination number (Z), packing density (κ), atomic volume average value (V_a) are calculated by formulae 4-6 and the obtained results are presented in table 2.

$$Z = 4X_{\text{Ge}} + 3X_{\text{As}} + 2X_{\text{Se}} \quad (4)$$

$$\kappa = \frac{\rho N_A}{\sum_i X_i A_i} \quad (5)$$

$$V_a = \frac{1}{\rho} \sum_i x_i A_i \quad (6)$$

The relative part of free volumes is often characterized by parameter of so-called compactness (δ) and is defined by formula [35]:

$$\delta = \frac{\sum_i (x_i A_i) / \rho_i - \sum_i (x_i A_i) / \rho}{\sum_i (x_i A_i) / \rho} \quad (7),$$

where X_{Ge} , X_{As} and X_{Se} are molar parts in ChGS composition, x_i , A_i and ρ_i are molar parts, atomic masses and densities of elements including into ChGS composition, ρ are experimentally obtained density values of the investigated substances.

The heteropolar bond energy between atoms including in investigated compositions and their degree of covalency are defined by formulae (8) and (9) [38-39]. The obtained results are presented in table 2. The obtained results are presented in table 2.

$$E_{A-B} = (E_{A-A} E_{B-B})^{1/2} + 30 (\chi_A - \chi_B)^2 \quad (8)$$

$$C = 100 \exp \left[- (\chi_A - \chi_B)^2 / 4 \right] \quad (9),$$

where E_{A-A} and E_{B-B} are energies of homeopolar bonds of A and B atoms, χ_A and χ_B are their electronegativity. From table 2 it is seen that degree of covalency of all chemical bonds including into investigated ChGS materials is enough high one. That's why the obtained results can be interpreted by the theory developed for materials with covalent bond.

Table 2.

communications	E, kC/mol	DC %
As-As	146	
As-Ge	170.77	99,28
As-Se	147.37	96,64
Ge-Ge	188	
Ge-Se	163.6	92,97
Se-Se	172	

The knowing of such structure parameters as bond energy, cohesion energy (energy required for breakage of all bonds) is necessary for understanding of composition dependence of physical properties. The calculation of given parameters requires the knowing of existing chemical bonds and their quantity in the investigated composition. Chemical bond approaches model (CBA) is used with this goal [40-43]. According to CBA the probability of heteropolar bond formation exceeds the homeopolar bond one, moreover, the most strong bonds (bonds with high energies) forms at the beginning and consistency of given bond formation corresponds to consistency of energy decrease up to the moment whereas the accessible atom valency would satisfied and finally the bonds energy is additive one. The supposed chemical formulae of the investigated compositions taking under consideration the given principles are presented in table 3. In third composition the glass structure consists of totally stitched tetrahedral ($\text{Ge}[\text{Se}_{1/2}]_4$) and pyramidal ($\text{AsSe}_{3/2}$) structural units which consist of energy-advantageous heteropolar bonds. In 1st, 2nd and 4th compositions along with the given element the homeopolar bonds with chalcogens atoms also take part, i.e. the excess selenium atoms take part in binding of the given elements and also

they connect between each other in chain and ring formations. The chemical formulae of last composition differ by excess of non-chalcogen element atoms. The accessible germanium atom valency is satisfied because of high bond energy Ge-Se (bond energy is 49,42 kcal/mol), excess part of arsenic atoms form the homeopolar bonds As-As. Taking under consideration the expected chemical bonds and their percent part in the investigated materials presented in table 2 the cohesion energy is estimated by following formula [38-39].

$$CE = \sum_i c_i E_i \quad (10)$$

where c_i and E_i are quantity and energy of expected bonds.

According to theory of topological limitation formed by Philips and Torp the material glassy-forming ability is defined by ratio between the number of limitations of interatomic force fields and atom degree of freedom [44-46]. For system in 3D space the atoms have three degrees of freedom which partly or totally are eliminated by the presence of hard bond limitations. There is critical composition at which the number of limitations (N_{co}) is balanced by quantity of degrees of freedom (N_d) accessible in network, i.e. $N_{co} = N_d$. Moreover, glass formation tendency is maximum one and it is known as threshold of hardness percolation. There are two types for mechanical limitations: $N\alpha = Z/2$ is known as limiting the extension of bond per atom and $N\beta = 2Z - 3$ is known as the limitation of bond of bends per atom in network $N\beta$. The general quantity of limitations is $N_{co} = 5/2 Z - 3$. The glass state is considered as floppy state when limit number is less than the value of degree of freedom ($N_{co} < 3$). In conditions when limit number is bigger than accessible value of degree of freedom the glass state becomes stressed rigid state.

According to [44-46] the glassy semiconductors with polymer structure consisting of weakly-stitched chains become hard ones when the chain stitching takes threshold meaning. In covalent systems the stitching degree is also expressed in terms of average coordination number Z . The transition of glass from floppy state into stressed rigid one will takes place near $Z = 2,40$ ($N_{co} = 3$).

However, the continuing investigations in this direction show that indeed there are two transitions of rigidity but not one predicted by theory of topological

limitations on chalcogenide glasses [47-50]. Indeed, two types of transitions of rigidity are observed in binary chalcogenide glasses at Z different values [47-49]. Based on results of these investigations, authors of [51-53] works report about existence of the intermediate phase between floppy and stressed rigid states in disordered chains.

Parameter R defined by ratio of number of possible chalcogens atom covalent bonds of to the number of possible covalent bonds of non-chalcogenide atoms plays the important role in result analysis of structure percolation threshold investigation of disordered materials [54]. Thus, $R=1$ presents itself the case of stoichiometric composition consisting of only energy profitable heteropolar bonds which explicitly evidence on chemical threshold existence. $R > 1$ values correspond to chemical compositions rich by selenium (samples 1,2, table 3) in which there are homeopolar bonds Se-Se along with existence of heteropolar bonds As-Se, Ge-Se. And in $R < 1$ values the chemical compositions differ by lack of chalcogens atoms for total satisfaction of non-chalcogen atom valent requirements (samples 5, table 2).

This composition differs by the existence of homeopolar bonds As-As (the valent requirements are totally satisfied because of high bond energy value Ge-Se for germanium atoms).

The topological and chemical ordering of amorphous matrixes of disordered materials are characterized by such values as average coordination number Z and parameter R . That's why it is reasonable to consider the dependence of physical parameters characterizing the structure of these values.

The dependences of structural parameters of ChGS investigated materials such as density (ρ_a) (fig. 2), average value of atomic volume (V_a) (fig. 3), packing coefficient (χ_a) (fig.4), compactness (δ_a) (fig.5) and cohesion energy (CE) (fig. 6) on Z and R are shown in figures.

As it is seen from the figures all graphs of physical parameter dependences on Z and R (at $Z=2,5$; $R = 1$) have the extreme points which are either maximum (ρ_a, χ_a, δ_a) or minimum (V_a) or (CE) dependence changes that is considered as the existence of percolation chemical threshold corresponding to stoichiometric chemical composition of As-Ge-Se system $[0,625(As_{0,4}Se_{0,6})][0,379(Ge_{0,333}Se_{0,666})]$.

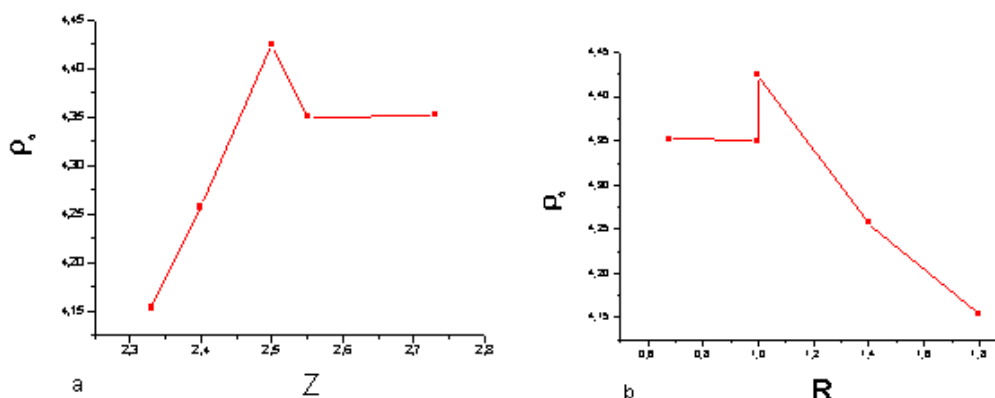


Fig.2. The density dependence (ρ_a) on Z (a) and R (b).

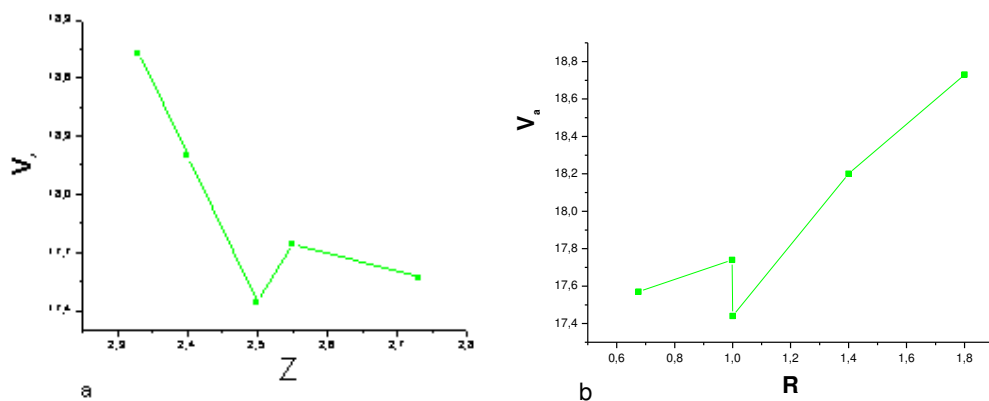


Fig.3. The dependence of atomic volume average value (V_a) on Z (a) and R (b).

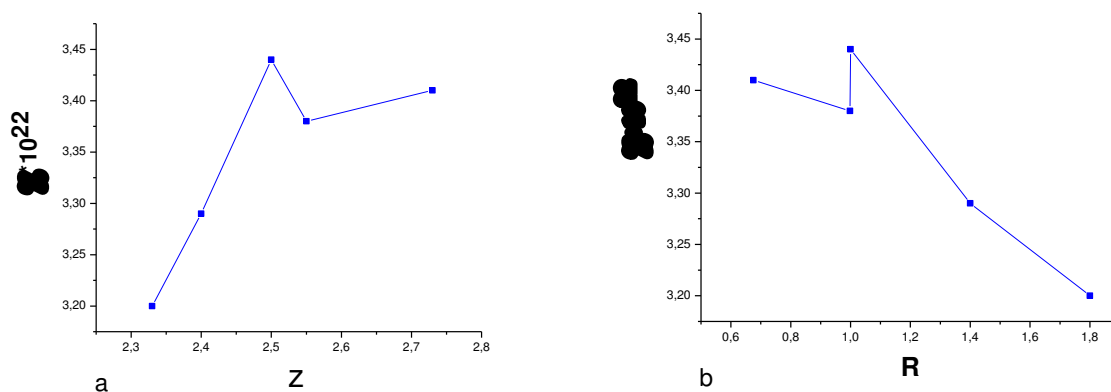


Fig.4. The dependence of packing index on Z (a) and R (b).

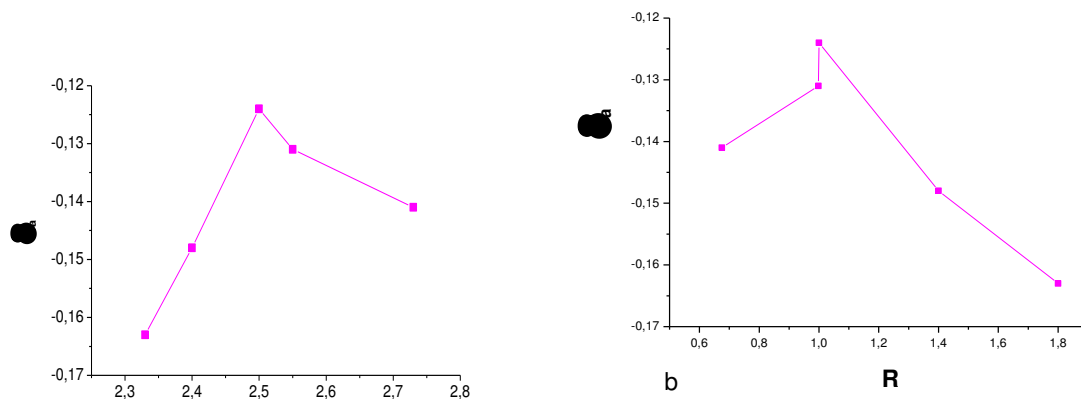


Fig.5. The dependence of compactness (δ_a) on Z (a) and R (b).

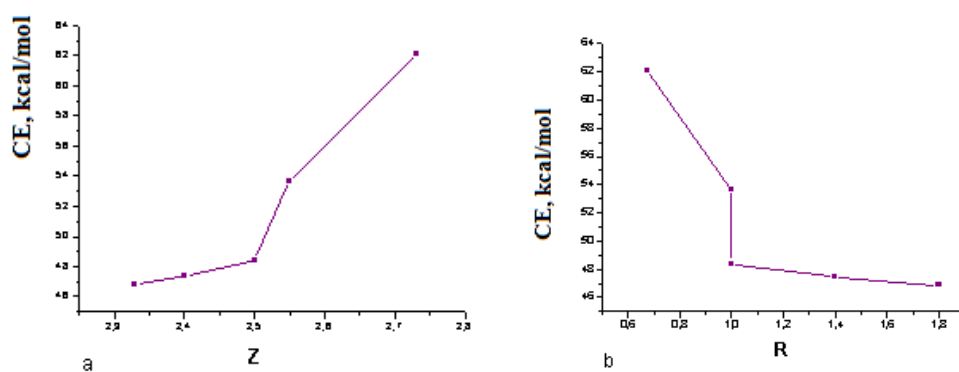


Fig.6. The dependence of cohesive energy (CE) on Z (a) and R (b).

At $Z=2,5 \div 2,55$ and $R=1 \div 0,998$ the dependences in figures 2-6 differ from other regions that evidences the existence of intermediate state corresponding to chemical composition of samples with serial numbers 3,4.

Finally, note that glassy-forming ability of noncrystalline materials is characterized by number of LP

electrons which are defined by formula $N_l = V - Z$ (V is average valency value) (table 3) for investigated compositions. $R > 1$ and $Z < 2,55$ values correspond to compositions with large number of LP electrons contributing to high glassy-forming ability of the given compositions.

Table 3.

№	compositions	Z	R	N_l	N_{eo}
1	$As_{16,67}Ge_{8,33}Se_{75}$ [0,417($As_{0,4}Se_{0,6}$)]·[0,252($Ge_{0,333}Se_{0,666}$)]·[$Se_{0,332}$]	2,33	1,8	3,34	2,83
2	$As_{20}Ge_{10}Se_{70}$ [0,5($As_{0,4}Se_{0,6}$)]·[0,303($Ge_{0,333}Se_{0,666}$)]·[$Se_{0,198}$]	2,4	1,4	3,2	3
3	$As_{25}Ge_{12,5}Se_{62,5}$ [0,625($As_{0,4}Se_{0,6}$)]·[0,379($Ge_{0,333}Se_{0,666}$)]	2,5	1	3,0	3,25
4	$As_{18,2}Ge_{18,2}Se_{63,6}$ [0,455($As_{0,4}Se_{0,6}$)]·[0,552($Ge_{0,333}Se_{0,666}$)]·[$Se_{0,016}$]	2,55	0,998	2,904	3,375
5	$As_{17}Ge_{28}Se_{55}$ [0,425($As_{0,4}Se_{0,6}$)]·[0,85($Ge_{0,333}Se_{0,666}$)]·[$-Se_{0,275}$]	2,73	0,675	2,54	3,825

The authors are thankful to professor I.R.Amiraslanov for help in experiment carrying out.

- [1] A.M. Andriesh, M. Bertolotti. Physics and applications of non-crystalline semiconductors in optoelectronics. Springer (1997). 481 p.
- [2] P. Houizot, C. Boussard-Plédel, A. J. Faber, L. K. Cheng, B. Bureau, P. A. Van Nijnatten, W.L. M. Gielesen, J.Pereira do Carmo, and J. Lucas. "Infrared single mode chalcogenide glass fiber for space," Opt. Express 15(19), 12529–12538 (2007).
- [3] J. S. Sanghera and I. D. Aggarwal. "Active and passive chalcogenide glass optical fibers for IR applications: a review," J. Non-Cryst. Solids 256–257(0), 6–16 (1999).
- [4] M. Churbanov, G. Snopatin, V. Shiryayev, V. Plotnichenko, and E. Dianov. "Recent advances in preparation of high-purity glasses based on arsenic chalcogenides for fiber optics," J. Non-Cryst. Solids 357(11), 2352–2357 (2011).
- [5] Zakery and S. Elliott. "Optical properties and applications of chalcogenide glasses: a review," J. Non-Cryst.Solids 330(1), 1–12 (2003).
- [6] A.B. Seddon. "Chalcogenide glasses: a review of their preparation, properties and applications," J. Non-Cryst.Solids 184(0), 44–50 (1995).
- [7] Elektronnie yavleniya v xalkogenidnix stekloobraznix poluprovodnikax, pod red. K.D. Chendina – SPB.; Nauka, 1996, 486 s.
- [8] J.A. Savage and S. Nielsen. "Chalcogenide glasses transmitting in the infrared between 1 and 20 μ — a state of the art review," Infrared Phys. 5(4), 195–204 (1965).
- [9] J.M. Harbold, F.O. Ilday, F.W. Wise, and B.G. Aitken. "Highly Nonlinear Ge-As-Se and Ge-As-S-Se Glasses for All-Optical Switching," IEEE Photon. Technol. Lett. 14(6), 822–824 (2002).
- [10] I.Kang, T. D. Krauss, F. W. Wise, B. G. Aitken, and N. F. Borrelli. Femtosecond measurement of enhanced optical nonlinearities of sulfideglasses and heavy-metal-doped oxide glasses," J. Opt. Soc. Amer.B, vol. 12, pp. 2053–2
- [11] W.A. Kamitakahara, R.L. Cappelletti, P. Boolchand, B. Halfpap, F. Gompf, D. A. Neumann, and H. Mutka. Phys. Rev. B 44, 94 ,1991!.
- [12] Z.U. Borisova. Glassy Semiconductors ~Plenum Press, NewYork, 1981.
- [13] J.K. Olson, H. Li, P.C. Taylor. Journal of Ovonic Research Vol. 1, No. 1, February 2005, p. 1 – 6.
- [14] Guang Yang, Bruno Bureau, Tanguy Rouxel, Yann Gueguen, Ozgur Gulbitten, Claire Roiland, Emmanuel Soignard, Jeffery L. Yarger, Johann Troles, Jean-Christophe Sangleboeuf, and Pierre Lucas. Phys. Rev. B 82,(2010), 195206 .
- [15] S.G. Bishop, N.J. Shevchik. Solid State Commun. 15, 629 (1974).
- [16] M.A. Popescu. J. Non-Cryst. Solids 35-36, 549 (1980).
- [17] S. Onari, T. Inokuma, H. Kataura, T. Arai. Phys. Rev. B 35 (9), 4373 (1987).
- [18] O.I. Shpotyuk, R.Ya. Golovchak, T.S. Kavetsky, A.P. Kovalskiy, M.M. Vakiv. Nucl. Instr. Meth. Phys. Res. B 166-167, 517 (2000).
- [19] O.I. Shpotyuk, T.S. Kavetsky, A.P. Kovalskiy, V. Pamukchieva. Proc. SPIE 4415 (2001)278
- [20] S.R. Elliott. Nature 354, 445 (1991)
- [21] S. Kokenyesi, J. Csikai, P. Raics, I.A. Szabo, S. Szegedi, A. Vitez. J. Non-Cryst. Solids 326&327, 209 (2003)
- [22] T.S. Kavetsky, O.I. Shpotyuk J. Optoelec. And Adv. Mat. V7,(2005), 2267-73.
- [23] T.S. Kavetsky, O.I. Shpotyuk, V.T. Boyko. J. of Phys. and Chem. of Solids, 68 (2007) 712–715
- [24] P.H. Gaskell. J. Non-Cryst. Solids 351 (2005), 1003–1013.
- [25] R.I. Alekberov, S.I. Mekhtiyeva, A.I. Isayev, M. Fábán. J. Non-Cryst. Solids, 470,(2017), p. 152-159.

- [26] T.S. Kavetsky, O.I. Shpotyuk, M. Popescu, A. Lorinczi, F. Sava. J. Optoelectron. Adv. Mater. , 9 (2007), 3079-3081.
- [27] L.E. Busse, S.R. Nagel. Phys. Rev. Lett., 47 (1981), 1848-1851.
- [28] K. Tanaka. Philos. Mag. Lett. , ISS3, 57(1988), 183-187.
- [29] S.R. Elliott. J. Non-Cryst. Solids 182 (1995), 1, 40–48.
- [30] J.E. Griffiths, J.C. Phillips, J.P. Remeika. Phys. Rev. B 20, 4140 (1979)
- [31] K. Tanaka. J. Non-Cryst. Solids 97-98, 391 (1987)
- [32] J.H. Lee, S.R. Elliott. J. Non-Cryst. Solids 192-193, 133 (1995)
- [33] S.R. Elliott. Phys. Rev. B 51, 8599 (1995)
- [34] S.R. Elliott. J. Non-Cryst. Solids 150, 112 (1992)
- [35] V. Pamukchieva, A. Szekeres, K. Todorova, M. Fabian, E. Svab, Zs. Revay, L. Szentmiklosi. J. Non-Cryst. Solids, 325 (2009), 2485-2490.
- [36] T.S. Kavetsky. Semiconductor Physics, Quantum Electronics & Optoelectronics, 2013. V. 16, N 2. P. 136-139
- [37] S.R. Elliott. Phys. Rev. Lett. 67 (1991) 711–714.
- [38] L. Pauling. The Nature of the Chemical Bond , Cornell University Press, Ithaca, NY, 1960.
- [39] Tauc, R. Grigorovici, A. Vancu. Phys. Status Solidi 15 (1966) 627.
- [40] A.A. Yadav, E.U. Masumdar. J. Alloys Compd. 505 (2015) 787.
- [41] A.A.M. Farag, M. Abdel Rafea, N. Roushdy, O. El-Shazly, E.F. El-Wahidy. J. Alloys Compd. 621 (2015) 434.
- [42] J. Bicerano, S.R. Ovshinsky. J. Non-Cryst. Solids 74 (1985) 75.
- [43] A.S. Hassanien, A. A. Akl. J. Non-Cryst. Solids, 428 (2015), 112-120.
- [44] J.C. Phillips. J.Non-Cryst. Solids 34,153-181 (1979).
- [45] M.F. Thorpe. J.Non-Cryst. Solids 57,355-370 (1983).
- [46] C. Phillips and M. F. Thorpe.” Solid State Commun., 53, 699–702 (1985).
- [47] P. Boolchand, X. Feng, W.J. Bresser. J.Non-Cryst. Solids, 293-295,348-356 (2001).
- [48] D.G. Georgiev, P. Boolchand, M. Micoulaut. Phys. Rev B 62, R9228-9231 (2000).
- [49] D.G. Georgiev, P. Boolchand, H. Eckert, M. Micoulaut, K.A Jackson. Europhysics Letters 62, 49-55 (2003).
- [50] Y.Wang, J. Wells, D.G. Georgiev, P. Boolchand, K. Jackson, M. Micoulaut. Phys. Rev. Lett. 87, 185503-1-4 (2001).
- [51] J.C. Phillips. Phys. Rev. Lett. 88, 216401-4 (2002).
- [52] M.F. Thorpe, D.J. Jacobs, M.V. Chubynski, J.C. Phillips. J.Non-Cryst. Solids,266-269,859-866 (2000).
- [53] M. Micoulaut, J.C. Phillips. Phys. Rev. B 67,104204-9 (2003).
- [54] L. Tichy, H. Ticha. Mater. Lett. 21 (1991) 313.

Receieved: 29.03.2018

NEW METHOD OF DECREASE OF TRANSIT-TIME BROADENING OF SPECTRAL RESONANCES

AZAD Ch. IZMAILOV

Institute of Physics, Azerbaijan National Academy of Sciences,

H. Javid av. 131, Baku, Az-1143, AZERBAIJAN

e-mail: azizm57@rambler.ru

I propose the new method of essential decrease of transit-time broadening of Doppler-free absorption resonances on transitions between long-lived quantum levels of atoms (or molecules) of a rarefied gas medium. This method is based on preliminary optical pumping of the ground term of atoms (molecules) by additional radiation which is spatially separated from the recording light beam. The proposed method may be applied in atomic (molecular) spectroscopy of ultra-high resolution and also in frequency and time standards.

Keywords: ultra-high resolution spectroscopy, transit-time broadening, optical pumping, frequency standards

PACS: 42.62.Fi, 42.62.Eh

1. INTRODUCTION

Development of effective methods of essential decrease not only Doppler but also transit-time broadening of recorded spectral resonances on optical transitions of atoms (molecules) in sufficiently rarefied gas media is very important for spectroscopy of ultra-high resolution and optimization of time and frequency standards [1,2]. Indeed, in many experiments in laser spectroscopy, the interaction time of atoms (molecules) with radiation fields is small compared with spontaneous lifetimes of quantum levels of resonance transitions. Then, in the absence of a Doppler broadening, linewidths of corresponding recorded spectral resonances are determined, mainly, by effective transit times of atoms (molecules) through the recording light beam. By now, two following methods of decrease of such a transit-time broadening are elaborated [1,2]: one may either enlarge the laser beam diameter, or one may slow down of atoms (or molecules) by corresponding “cooling” techniques.

In the present work, I propose the new method to achieve this goal, which is based on preliminary optical pumping of the ground quantum term of atoms (or molecules) by the additional radiation which is spatially separated from the recording light beam. This method may be applied both independently and along with the noted known methods for further decrease of transit-time broadening of recorded spectral resonances.

Indeed, let us consider sufficiently simple experimental scheme in Fig.1, which presents the cross section of the recording light radiation with the diameter d and the coaxial cross section of the beam of broadband optical pumping. It is considered that the central radiation in Fig.1 records the spectral resonance on a transition $a \rightarrow c$ from sublevel a of the ground atomic term to the long-lived (in particular metastable) excited quantum state c . Such ultra narrow spectral resonances, for example, may take place in Doppler-free multiphoton spectroscopy [1]. At the same time, the coaxial broadband optical pumping (Fig.1) is realized on a non-cyclic transition $a \rightarrow b$ from the same lower level a to the excited state b (Fig.2). In experiments we may directly distinguish a contribution of optically pumped atoms to the analyzed resonance on the transition $a \rightarrow c$. This is achieved by

recording of the difference between signals of absorption (or dispersion) of the central light beam, which are subsequently detected with and without the spatially separated optical pumping (Fig.1).

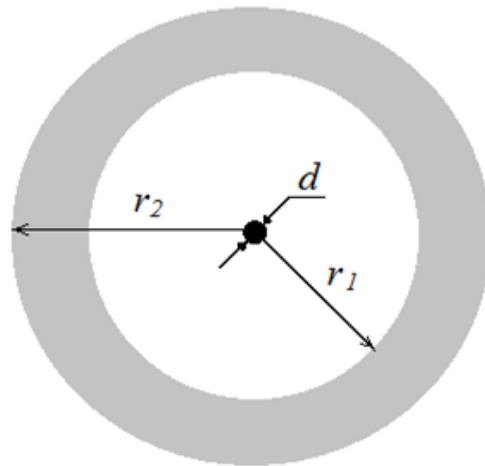


Fig.1. Scheme of cross section of the recording light beam with the diameter d and the coaxial spatially separated optical pumping radiation limited by radii $r_2 > r_1$.

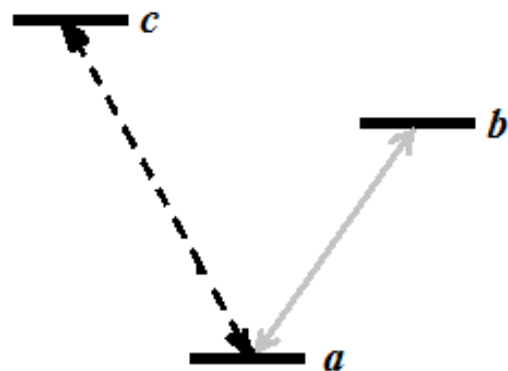


Fig.2. Diagram of atomic quantum levels and transitions, where $a \rightarrow c$ is the analyzed transition and $a \rightarrow b$ is the pumping transition from the ground level a .

Characteristic transverse components of velocities of optically pumped atoms, reaching the recording light beam, may be substantially reduce at lowering of the pumping rate. Thus, essential decrease of the transit-time broadening of the spectral resonance on analyzed transition $a \rightarrow c$ may be achieved, because of recording of such a resonance directly on these comparatively slow moving pumped atoms.

2. BASIC RELATIONSHIPS

Let us consider a sufficiently rarefied gas medium, where the free path of atoms (molecules) substantially exceeds the radius r_2 of the beam of broadband optical pumping (Fig.1). The pump intensity on the transition $a \rightarrow b$ is assumed to be so low that population of excited state b is negligibly small relative to that of initial level a (Fig.2). Then, from known balance relations [1] we receive the following equation for the population $\rho_a(\mathbf{R}, \mathbf{v})$ of atoms on the long-lived level a with the velocity \mathbf{v} and the coordinate vector \mathbf{R} :

$$\mathbf{v} \frac{\partial \rho_a}{\partial \mathbf{R}} = -W(\mathbf{R})\rho_a, \quad (1)$$

where $W(\mathbf{R}) = \epsilon_{ab}(\mathbf{R})(1 - B_{ba})$ is the rate of the broadband optical pumping, $\epsilon_{ab}(\mathbf{R})$ is the excitation probability of atoms by the pumping radiation on the non-cyclic transition $a \rightarrow b$, the constant B_{ba} is the probability of the subsequent radiative decay through the channel $b \rightarrow a$ ($B_{ba} < 1$). It is assumed, that atoms have equilibrium distributions both on their velocities and populations of quantum levels before interaction with the pumping radiation. Under the above conditions, the population $\Delta\rho_a(\mathbf{R}, \mathbf{v})$ of the optically pumped atoms in the lower level a is described by expression:

$$\Delta\rho_a(\mathbf{R}, \mathbf{v}) = n_a F(\mathbf{v}) - \rho_a(\mathbf{R}, \mathbf{v}), \quad (2)$$

where n_a is equilibrium density of atoms on the level a with the Maxwell distribution $F(\mathbf{v})$ on atomic velocities \mathbf{v} . We will consider the cylindrically symmetric distribution of the optical pumping rate $W(r)$ (1) on the distance r from the central axis of recording light beam (Fig.1). Then, from Eq.(1), we receive the following expression for the population $\Delta\rho_a$ (2) of optically pumped atoms, reaching the region of sufficiently narrow recording light beam with the diameter $d \ll r_l$ (Fig.1):

$$\Delta\rho_a(v_r, s) = n_a F_r(v_r) \left[1 - \exp\left(-\frac{su}{v_r}\right) \right], \quad (3)$$

where the dimensionless parameter s characterizes efficiency of the optical pumping and has the following form:

$$s = \left(\frac{1}{u}\right) \int_{r_1}^{r_2} W(r) dr, \quad (4)$$

and $F_r(v_r)$ is the Maxwell distribution on radial (transverse) component v_r of atomic velocity:

$$F_r(v_r) = 2v_r u^{-2} \exp(-v_r^2 u^{-2}), \quad (5)$$

with the most probable atomic speed u in the gas.

Let us consider, for example, Doppler-free absorption spectral line, whose profile has the following Lorentzian shape for atoms (molecules) with transverse velocity component v_r :

$$L(\delta, v_r) = \frac{\gamma(v_r)}{[\gamma(v_r)^2 + \delta^2]}, \quad (6)$$

where δ is the frequency detuning of the recording light beam (Fig.1) from the center of the analyzed quantum transition $a \rightarrow c$ (Fig.2). The characteristic width $\gamma(v_r)$ of the given line (6) is the sum of two terms:

$$\gamma(v_r) = \gamma_0 + \frac{v_r}{\langle v_r \rangle} \gamma_{tr}, \quad (7)$$

where γ_0 is the radiative width of this line, which is determined by the lifetime of the excited level c , and the value γ_{tr} (in the second phenomenological term) is the transit-time relaxation rate in the absence of the optical pumping at the average transverse component of atomic velocity $\langle v_r \rangle = \int_0^\infty v_r F_r(v_r) dv_r \approx 0.886u$.

From Eqs. (3), (6) we receive the integral absorption profile directly for optically pumped atoms with all possible velocity components v_r :

$$\Delta J(\delta, s) = \int_0^\infty \Delta\rho_a(v_r, s) L(\delta, v_r) dv_r. \quad (8)$$

In the absence of the optical pumping, corresponding profile for nonpumped atoms has the form:

$$J_0(\delta) = n_a \int_0^\infty F_r(v_r) L(\delta, v_r) dv_r. \quad (9)$$

3. DISCUSSION OF RESULTS AND CONCLUSION

Fig.3 presents dependences of the population $\Delta\rho_a$ (3) of optically pumped atoms on their transverse velocity component v_r at different intensities of the optical pumping. For sufficiently large values of the parameter $s \gg 1$ (4), effective pumping practically all atoms occurs and then corresponding dependence $\Delta\rho_a(v_r, s)/n_a$ (curve 4 in Fig.3), in fact, coincides with the equilibrium velocity distribution $F_r(v_r)$ (5). At the same time, we see in Fig.3 that lowering of this pumping parameter s causes not only decrease in the number of optically pumped atoms but also effective shift of the distribution $\Delta\rho_a(v_r)$ to smaller values of their velocity components v_r . Thus, it is possible significantly to reduce transit-time broadening of spectral resonances recorded directly on given pumped atoms.

Further we will consider situation when characteristic rate γ_{tr} of transit-time relaxation of atoms in the absence of the optical pumping is many times greater than the radiative relaxation rate γ_0 (7) of analyzed spectral resonance. Fig.4 presents spectral absorption profiles $\Delta J(\delta, s)$ (8), which are recorded directly on optically pumped atoms at various pumping parameters s (4). Lowering of the pumping intensity leads to decrease both amplitude A and width W of such spectral resonances. Indeed, Fig.5 presents corresponding values $A(s) = \Delta J(\delta = 0, s)$ and W (on the half-height)

versus the pumping parameter s (4). With the growth of the parameter s in the region $s > 1$, these quantities A and W asymptotically approach to values A_0 and W_0 corresponding to the spectral profile $J_0(\delta)$ (9) for atoms in the absence of the optical pumping. We see in Fig.5b that essential decrease of transit-time broadening of the recorded spectral resonance may be achieved at lowering of the optical pumping. For example, according to Fig.5, at the pumping parameter $s=0.02$, the width W of the resonance decreases about 5 times in comparison with the corresponding value W_0 obtained in the absence of the optical pumping, although amplitude A of this resonance is about 9% of the maximum value $A_0=J_0(\delta=0)$ (9).

Even more narrow sub-Doppler resonances may be observed at the frequency modulation of the recording light beam [1,2]. Then, directly the first frequency derivative of the absorption profile is detected (Fig.6). The characteristic width of such a resonance is determined by the frequency interval Γ between extreme values of corresponding spectral dependence.

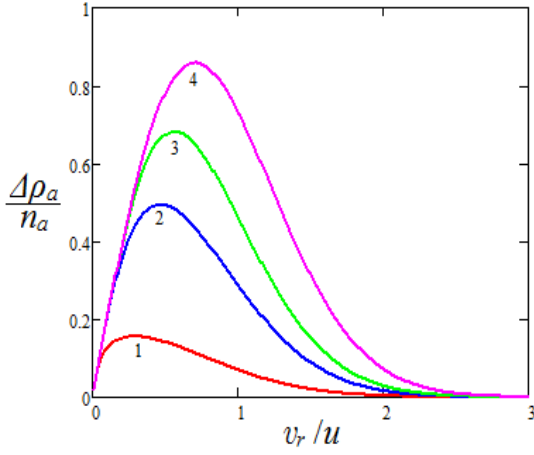


Fig.3. Distribution $\Delta\rho_a(v_r, s)$ of optically pumped atoms on the transverse component v_r of their velocity at the pumping parameter $s=0.1$ (curve 1), 0.5 (2), 1 (3), and 10 (4).

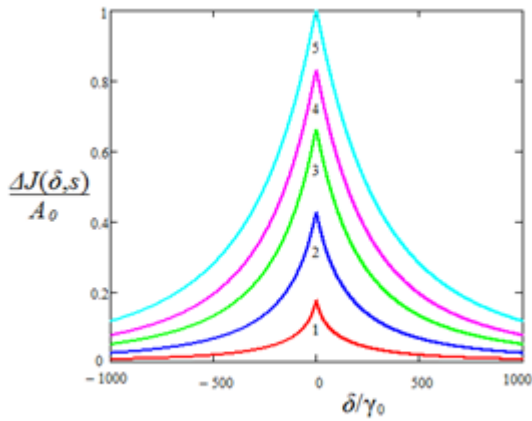


Fig.4. Spectral absorption resonance $\Delta J(\delta, s)$ of optically pumped atoms versus frequency detuning δ in units $A_0 = J_0(\delta=0)$ Eq.(9), when $\gamma_0 = 2 \cdot 10^{-3} \gamma_{tr}$ and the pumping parameter $s=0.05$ (curve 1), 0.2 (2), 0.5 (3), 1 (4) and 10 (5).

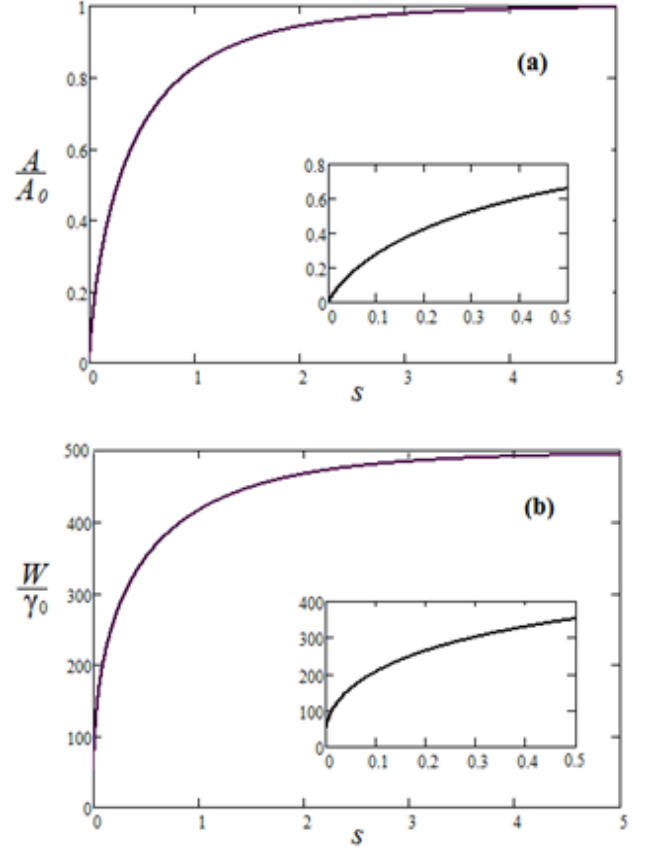


Fig.5. Amplitude A (a) and width W (b) of the spectral absorption resonance $\Delta J(\delta, s)$ (from Fig.4) versus the pumping parameter s , when $\gamma_0 = 2 \cdot 10^{-3} \gamma_{tr}$. Insets show corresponding dependences in the region of sufficiently small values $s < 0.5$.

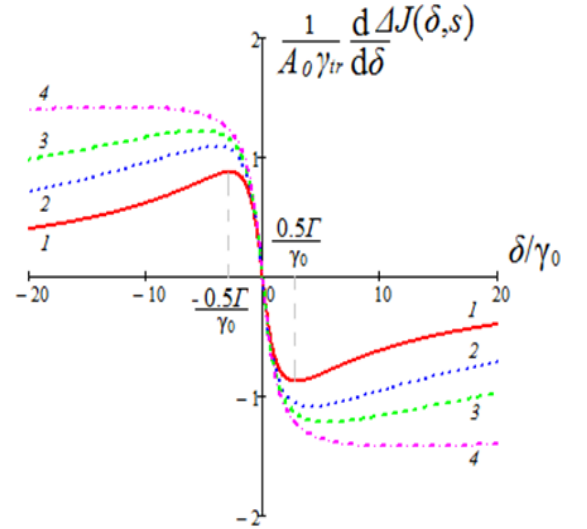


Fig.6. First frequency derivative of the absorption resonance $\Delta J(\delta, s)$ (Fig.4) of optically pumped atoms versus the frequency detuning δ , when $\gamma_0 = 2 \cdot 10^{-3} \gamma_{tr}$ and the pumping parameter $s=0.02$ (curve 1), 0.05 (2), 0.1 (3), and 1 (4). The value Γ determines the characteristic width of such a resonance.

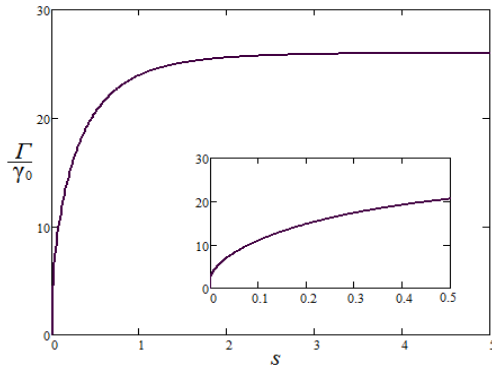


Fig.7. Width Γ of spectral resonance (from Fig.6) versus the pumping parameter s , when $\gamma_0 = 2 * 10^{-3} \gamma_{tr}$. Inset shows the corresponding dependence in the region of sufficiently small values $s < 0.5$.

This width Γ also may be significantly reduced by lowering of the optical pumping intensity in the proposed method (Fig.7).

We have considered comparatively simple experimental scheme (Fig.1) with the cylindrical symmetry of light beams. However, in the similar manner, it is possible to analyze theoretically and then to implement in practice another schemes with spatially separated beams of recording radiation and optical pumping for effective decrease of transit-time broadening of detected spectral resonances.

The proposed method may be applied in atomic (molecular) spectroscopy of ultra-high resolution and also in frequency and time standards.

[1] W. Demtroder. Laser Spectroscopy: Basic Concepts and Instrumentation. (Springer, 2003).

[2] F. Riehle. Frequency Standards-Basics and Applications. Berlin: Wiley-VCH, 2004.

Received: 26.02.2018

THE ANALYSIS OF DIELECTRIC ABSORPTION DISPERSION OF GLYCINE WATER SOLUTION

S.T. AZIZOV, O.A. ALIYEV

Institute of Physics of Azerbaijan NAS, AZ 1143, H.Javid ave.,131, Baku, Azerbaijan

Institute of Physics of Azerbaijan NAS, AZ 1143, H.Javid ave.,131, Baku, Azerbaijan

e – mail: samir_azizov@mail.ru

The analysis of glycine water solution measured by dielectric constant at temperature from 20 до 50 ° C on 5 frequencies in centimetric range is carried out.

The dielectric spectra are studied taking under consideration other frequencies given in scientific literature.

Keywords: dielectric spectroscopy, molecular spectroscopy, glycine, glycine dielectric properties, glycine water solution.

PACS: 61.20. – p; 77.22. – d; 77.22.Gm

INTRODUCTION

The analysis of obtained results of observable dielectric absorption dispersion of glycine water solution in [1] with calculated results, presented earlier in [2], reveals the divergences exceeding the measurement errors. That's why the necessity of conclusion review [2] based on model [3] in which the presence of two dielectrically active types of kinetic units in amino-acid water solutions are postulated, takes place.

THE RESULTS AND DISCUSSION

The presented analysis is related to results of measurements of dielectric constants ϵ' and absorption indexes ϵ'' at temperatures from 20 up to 50° C and wave length $\lambda = 66,7; 50,0; 39,5; 33,3$ [2]; 8,28 [4]; 5,83; 4,02; 3,23 [1]; 3,17 [4]; 2,10; 1,40 [1]; 0,85 cm [4]. The measurement errors don't exceed 1 and 4% [2]; 3 and 6% [1]; 2 and 5% [4] for ϵ' and ϵ'' . The error of equilibrium dielectric constant ϵ_0 is less than 0,5% [2,5].

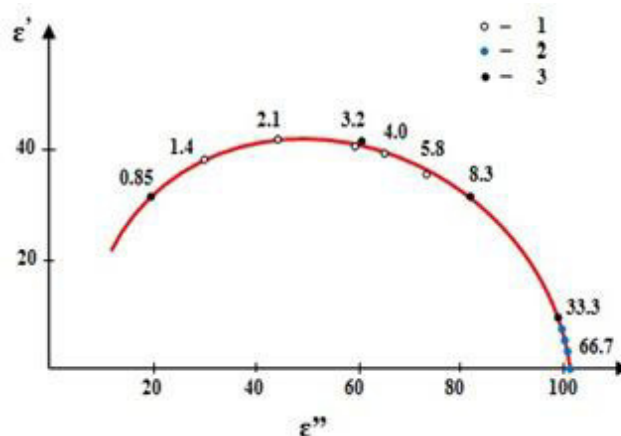


Fig.1. Arc diagram of glycine water solution at 20°C.

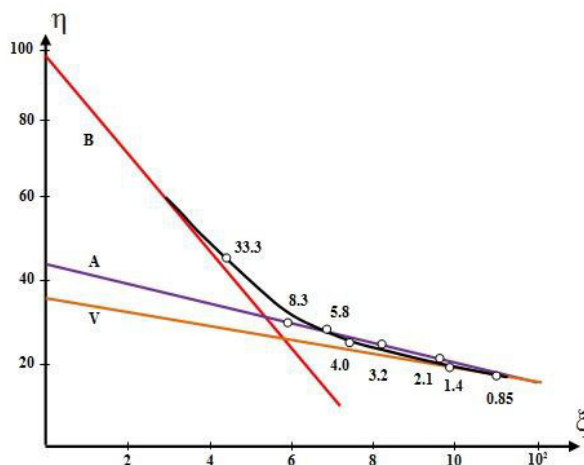


Fig.2. Line diagram of glycine water solution at 20°C.

THE ANALYSIS OF DIELECTRIC ABSORPTION DISPERSION OF GLYCINE WATER SOLUTION

The measurement results at 20° C character for whole studied temperature interval in arc representation are shown in fig.1. At it is seen that spectrum is characterized by strongly expressed asymmetry. Let's suppose that observable relaxation of oriented part of solution polarization can be described by linear superposition of arbitrary number of i Debye processes

$$\varepsilon' - j\varepsilon'' = \varepsilon_{\infty} + \sum (\varepsilon_{0i} - \varepsilon_{\infty i}) (1 + j\omega\tau_i)^{-1}, \quad (1)$$

where $\tau_i > \tau_{i+1}$; $\varepsilon_{\infty i} = \varepsilon_{0(i+1)}$; the rest designations have the usual meaning. For $i = 2$ this equation transforms into the following form:

$$[(\tau_1\tau_2)\tau_0^{-2}]\xi + \eta\eta = (\tau_1 + \tau_2)\tau_0^{-1}, \quad (2)$$

$$\xi = \omega\tau_0 (\varepsilon' - \varepsilon_{\infty}) (\varepsilon'')^{-1}, \quad (2a)$$

$$\eta = (\varepsilon_0 - \varepsilon')(\omega\tau_0\varepsilon'')^{-1}, \quad (2b)$$

where homogenization constant is $\tau_0 = 10^{-12}$ c. According to (2) the dielectric spectrum satisfying to equation (1) with $i = 2$ is presented in $\eta = f(\xi)$ graph by the line with inclination equal to $(\tau_1\tau_2)\tau_0^{-2}$ and point of intersection with ordinate axis equal to $(\tau_1 + \tau_2)\tau_0^{-1}$. The partial amplitudes $\Delta_i = \varepsilon_{0i} - \varepsilon_{\infty i}$ including in (1) are calculated with the help of experimental values ε' , ε'' , ε_0 and estimated τ_1 , τ_2 , ε_{∞} by the following formulae

$$\Delta_1 = (1 + \omega^2\tau_1^2)[(\varepsilon' - \varepsilon_{\infty})\tau_2 - \varepsilon''\omega^{-1}](\tau_2 - \tau_1)^{-1} \quad (3)$$

$$\Delta_2 = (1 + \omega^2\tau_2^2)[(\varepsilon' - \varepsilon_{\infty})\tau_1 - \varepsilon''\omega^{-1}](\tau_1 - \tau_2)^{-1} \quad (4)$$

which may be obtained from (1). The preliminary value can be found from equation from following equation

$$\varepsilon' = \varepsilon'' (\omega\tau)^{-1} + \varepsilon_{\infty}, \quad (5)$$

obtained from (1) at $i = 1$.

Δ_1 and Δ_3 values are calculated by (3)-(4) correspondingly. The characteristics of intermediate regions are obtained from the following expression:

$$\varepsilon'_2 - j\varepsilon''_2 = \varepsilon' - j\varepsilon'' - [(\varepsilon_{\infty} + \Delta_1(1 + j\omega\tau_1)^{-1} + \Delta_3(1 + j\omega\tau_3)^{-1})] \quad (6)$$

Note that such approach gives the only rough values of relaxation parameters and that's why the further fitting is required. The criteria of analysis satisfaction are: 1) approximate constancy of Δ_i partial amplitudes at different λ calculated by (3-4) [6,7]; 2) carrying out of condition [8]

$$S \leq S_m \quad (7)$$

where $S_m = 2n$ (n is number of used λ). The sum S of standard deviation of measured ε' , ε'' on estimated ε'_{cal} , ε''_{cal} is calculated by the formula:

$$S = \sum (S_1 + S_2) = \sum \left\{ \left[(\varepsilon' - \varepsilon'_{cal})(\varepsilon'v')^{-1} \right]^2 + \left[(\varepsilon'' - \varepsilon''_{cal})(\varepsilon''v'')^{-1} \right]^2 \right\} \quad (8)$$

where v', v'' are relative errors of ε' , ε'' measurements at given λ .

Table 1

The comparison of experimental and calculative spectra of glycine water solution at 20°C ($\varepsilon_0 = 102,5$; $\varepsilon_{\infty} = 5,0$; $\tau_1 \cdot 10^{12}$ s)

λ cm	ε'	ε''	A		[2]		B + V	
			$\tau_1=39,0$; $\Delta_1=22,2$	$\tau_2=8,3$; $\Delta_2=59,3$	$\tau_1=72,0$; $\Delta_1=22,2$	$\tau_2=9,0$; $\Delta_2=75,3$	$\tau_1=72,0$; $\tau_3=8,1$; $\Delta_2=28,5$; $\Delta_3=53,0$	$\tau_2=25,0$; $\Delta_1=16,0$; $\Delta_3=53,0$
			S_1	S_2	S_1	S_2	S_1	S_2
66,7	101,0	6,34	1,02	9,77	0,28	0,10	0,48	0,16
50,0	101,4	8,51	0,05	11,64	0,16	0,84	0,09	0,35
39,5	100,5	10,5	0,39	9,43	0,09	1,09	0,04	0,23
33,3	99,4	12,3	1,47	8,93	0,01	1,69	0,04	0,37
8,28	84,3	29,7	0,06	0,00	0,16	11,34	0,69	0,29
5,83	74,7	32,5	0,09	0,21	1,79	0,86	0,02	0,02
4,02	65,2	37,4	0,00	0,34	8,98	2,49	0,09	0,39
3,23	59,2	37,1	0,00	0,01	11,41	0,24	0,26	0,02
3,17	61,4	38,2	4,84	0,16	7,23	1,01	8,56	0,16
2,10	44,5	37,1	1,52	0,36	25,34	2,01	0,05	0,24
1,40	31,2	35,5	2,12	0,18	24,47	3,31	0,28	0,02
0,85	19,1	28,9	0,03	0,04	4,39	3,75	1,10	0,08
S	$S_m = 24,0$		52,7		113,0		14,0	

According to line diagram at $\lambda \leq 8,3$ cm the superposition of two Debye processes takes place.

The set of parameters (see 4,5 rows, table 1) corresponding to A line indeed allows us to reproduce this region of observable spectrum ($S=10,0$; $S_m=16,0$). However, $S = 40,3$ at $S_m = 16,0$ outside its limits ($\lambda \geq 33,3$ cm). All these facts prove the nonrandom nature of inclinations from linearity in fig.2 at $\lambda > 8,3$ cm. Unfortunately, the use of decimeter points for the definition of long-wave edge true shape of $\eta(\xi)$ graph is difficult because of the fact that the difference $\varepsilon_0 - \varepsilon'$ including in expression (2b) is comparable with measurement error. Thus, $\varepsilon_0 - \varepsilon' = 1,5$ at $\lambda = 66,7$ cm whereas $\varepsilon_0 = 102,5 \pm 1,0$; $\varepsilon' = 101,0 \pm 1,0$. The point at $\lambda = 33,3$ cm where $\varepsilon_0 - \varepsilon' = 3,1$ is the unique relatively reliable point. In this case $\eta(\xi)$ graph has the form of curve the one of the possible variants of which is shown in fig.2.

The approximation of low- and high-frequency regions of $\eta(\xi)$ curve by B and V segments allows us to find the previous values of equation parameters (1) with $i = 3$ with the help of above mentioned technique. As it is seen the interval of possible relaxation times is between 84 and 7ps. According to values $\tau_1' = 16,5$ ps and $\tau_3' = 27,7$ ps intermediate frequency process has $\tau_2 \sim 20$ ps. These estimates coincide with $\tau_1 = 39$ ps value corresponding to A

line which can be considered as relaxation time of sum process formed by contributions with $\tau \sim 80$ and ~ 20 ps.

The final results of spectrum treatment with $i = 3$ are given in 8,9 rows of table 1. The strong loss ($S=8,56$) of the point at $\lambda=3,17$ cm is caused by ε' value that is proved by independent data at $\lambda=3,20$ cm [9].

As the spectrum division in three regions leads to $S < S_m$ the further fitting of calculation to the experiment becomes the unfounded. Note that closeness of τ_3 value to τ_{water} pure water which is by data of different authors is from 8,9 up to 9,5ps (20°C). The high-frequency region at given τ_3 and τ_{water} is divided in two contributions [11, 12]. The best agreement is achieved at choice $\tau_{\text{water}} = 8,6$ ps.

CONCLUSION

According to [13, 14] the solvent polarity doesn't influence on orientational dynamics of glycine water solution. At the same time the partial contribution in spectrum of glycine water solution system at all studied concentrations and temperatures is characterized by values of relaxation times [8,15]. The intermediate-frequency process (2) in spectrum of water-glycine system reflects the existence of regions with undisturbed submolecular organization correspondingly.

-
- [1] S.T. Azizov, O.A. Aliev. Fizika, vol. XXIII, №4, section: En, p. 13 – 16., 2017.
 - [2] J.L. Salefran, D. Delbos, C. Marzat, A. Bottreau. - M. Ann.Scl. Univ. Clermont. Phys., 1977, № 17, 109.
 - [3] J.G. Kirkwood. In: "Proteins Amino Acides and Pertids", ed. Gohn E.J. Elsal J. T. Reinhold. N.Y., 1943, 294.
 - [4] A.-M. Bottreau, G. Delbos, C. Marzat, Y. Lacroix, J.-L. Salefran, Y. C. R. Dutuit. Acad. Sci., B 76, 1973, 373.
 - [5] J.T. Edvarde, P.G. Farell, J.L.Job. J. Amer. Chem. Soc., 96, 1974, 902.
 - [6] J.-L. Salefran. Chem. Phys. Lett., 45, 1977, 124.
 - [7] A.I. Rusanov, A.K. Shekin. Jurnal; fiziceskoy-ximii. – 2009q, t.83 -№2, s. 290 – 298. (In Russian).
 - [8] K.E. Zulfugarzade, G.A. Gadjiev, L.M. Imanov. "Izv. AN Azerb. SSR, seriya fiz.-texn. I mastem. nauk", 1969, № 1, 63. (In Russian).
 - [9] Ya.Yu. Axadov. Dielektriceskie svoystva binarnix rastvorov. M., "Nauka", 1977, 322. (In Russian).
 - [10] A.-M. Bottreau, J.-M. Moreau, J.-M. Laurent, C. Marzat. J.Chem. Phys. 62, 1975, 360.
 - [11] Ch.O. Gadjar, S.T. Azizov, Sh.K. Agamuradova. Fizika. t XIV, №2, s. 56 – 59, 2008. (In Russian).
 - [12] K.E. Zulfugarzade, L.A. Guliev, L.M. Imanov. "Izv. AN Azerb. SSR, seriya fiz.-texn. i matem. nauk", 1973, № 1, 42. (In Russian).
 - [13] S.T. Azizov, O.A. Aliev, K.E. Zulfugarzade. Fizika, Cild, № 4, s. 22 – 26, 2017.
 - [14] K. Dharmalingam, K. Ramachandran, Sivagurunathan, B.P. Undre, P.W. Khirade and S.C. Mehrotra. Mol. Phys., 104, 2835 (2006).
 - [15] 15. P. Jund and R. Jullien, Phys. Rev. B 59, 13 707 (1999).
 - [16] 16. J. Horbach and W. Kob. Phys. Rev. B 60, 3169 (1999).
 - [17] 17. W. Dewine, B.M. Lowe. J. Chem. Soc., A. 1971, 2113.

Received: 23.03.2018

INVESTIGATION OF SEMIPOLAR GaN TEMPLATES AND InGaN MULTIPLIES QUANTUM WELLS GROWN BY HVPE AND MOVPE

SEVDA ABDULLAYEVA^{1,2}, GULNAZ GAHRAMANOVA^{1,2}, RASIM JABBAROV^{1,2},
CESARE FRIGERI³

¹*Institute of Physics, Azerbaijan National Academy of Sciences, G. Javid av., 131,
Baku 1143, Azerbaijan*

²*Research and Development Center for High Technologies, Ministry of Transport, Communication
and High Technologies of Azerbaijan Republic, 2, Inshaatchilar ave., AZ1073, Baku*

³*Institute of CNR-IMEM, Parco Area Delle Scienze, 37/A, Fontanini, Italy*

Email: gulnaz.gehremanova@hotmail.com,

In this work semipolar GaN template was grown by HVPE and semipolar InGaN QWs were grown on GaN/sapphire template by MOVPE. In order to clarify the reasons for the poor crystal quality and surface defects of semipolar GaN structures grown on sapphire wafers and we have analyzed both of samples comparatively. Via microscopic analyzes it has been obtained that the numbers of different kind of hillocks on the top of InGaN QWs are more than GaN template. TEM images showing a decreasing concentration of indium, e.g. from $x=0.200$ to $x=0.197$, from the buffer to the top of the sample. Photoluminescence peak position is not shifted with increasing excitation source power but shifted with increasing temperature from 16 K to 300 K considerably.

Keywords: III-nitrides, heterostructures, multiple quantum wells, semipolar, photoluminescence, InGaN, Atomic Force Microscopy, Transmission Electron Microscopy, Hydride Vapour Phase Epitaxy

PACS: 78.20.+e, 81.05.Ea, 81.10.+h

1. INTRODUCTION

The group of III-nitrides is widely used in many areas of our modern life: light-emitting diodes (LEDs), lasers, high electron mobility transistors (HEMTs), different type of sensors and it is some of the list of all their possible applications for the current period. The epitaxially grown InGaN wafers usually have many dislocations due to the different lattice constants and thermal expansion coefficients between the epilayer and the substrate, while InGaN nanowires can be defect-free due to different growth mechanism. Last several decades many methods have been tried to fabricate GaN structures and InGaN quantum wells (QWs) [1–5]. The GaN growth technique by MOVPE was developed in 1986 by Akasaki and H2. Amano [7]. In the early 90's modifications were made to the design of existing MOVPE tools to prevent harmful precursor and reactor flows [8, 10]. Metal-organic chemical vapor deposition (MOCVD) and molecular beam epitaxy (MBE) [11–16] were also used to grow InGaN-based nanostructures.

The first deposition of gallium nitride (GaN) was grown by hydride vapor phase epitaxy (HVPE) and investigation for optical and electrical characterization was demonstrated by Maruska and Tietjen in 1969 [17]. Kim et al. also used hydride vapor phase epitaxy (HVPE) to grow InGaN nanorods and fabricated high-brightness LED [1–4].

It is important to compare GaN template and the InGaN QWs morphology dependence of growth methods. In our previous papers [18–21] we investigated semipolar InGaN QWs which were grown by MOVPE directly. In this paper, InGaN QWs was studied with growing on semipolar GaN template which was grown by HVPE.

2. EXPERIMENT

The r-plane (10-12) sapphire substrate is used as a substrate of semipolar (11-22) InGaN MQWs. The semipolar (11-22) QWs orientation and r-plane (10-12) sapphire substrate have a tilting angle with respect to the c-plane (0001), respectively $58,4^\circ$ and $57,6^\circ$ (Fig 1a).

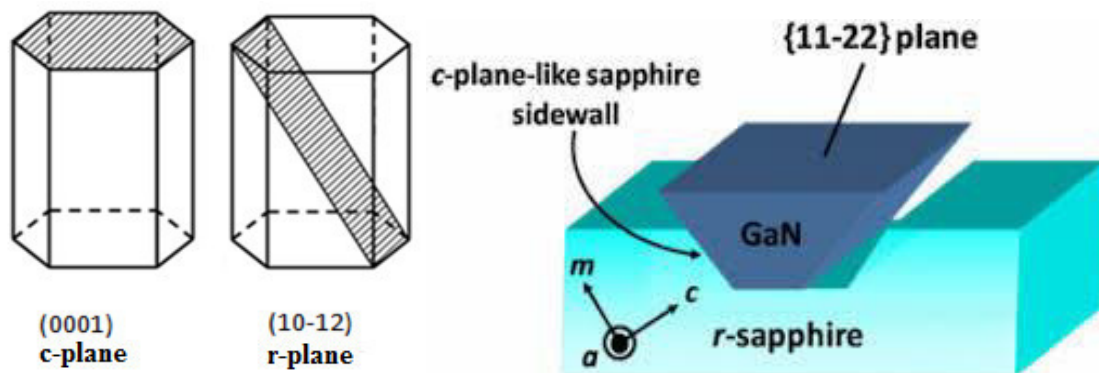


Fig. 1. a) Atomic c- and r- planes of the wurtzite crystal. b) Illustrate of semipolar (11-22) GaN growth direction at the inclined c-plane-like sidewalls (schematically).

The photolithography process was done for tilting the substrate. For this purpose a negative photoresist (PR) has been used on the rotated substrate and the thin photoresist was spread on the substrate. After covering about $1.7\mu\text{m}$ thick PR the substrate by photoresist it was baked during two minutes. In the next step the PR was exposed by the UV light. Therefore, the exposed parts of the photoresist become less soluble in chemical developer. The unexposed parts of the photoresist are removed by chemical developer. In the next step via Reactive Ion Etching (RIE) the samples were etched in chosen optimal pressure and etching time. Hence, the stripes get transferred into the sapphire substrate and the

desired angle ($58,4^\circ$) of trench side –wall was achieved (Fig. 1b). After RIE, in order to remove the photoresist mask stripes on the substrate first oxygen plasma cleaning was done. Then in the chemical solutions of KOH and H_2O and H_2SO_4 and H_2O_2 the substrate was cleaned completely from residuals. Then the silicon dioxide (SiO_2) was sputtered on top of the sample (or c-plane facet) a mask to get covered with SiO_2 to avoid parasitic growth. Thus, in order to structure the (10-12) oriented sapphire, at first about $1.7\mu\text{m}$ thick layer of a negative photoresist is spin-coated on it. The photoresist itself is patterned by optical lithography with a stripe shadow mask with an opening of $3\mu\text{m}$ and a period of $6\mu\text{m}$.

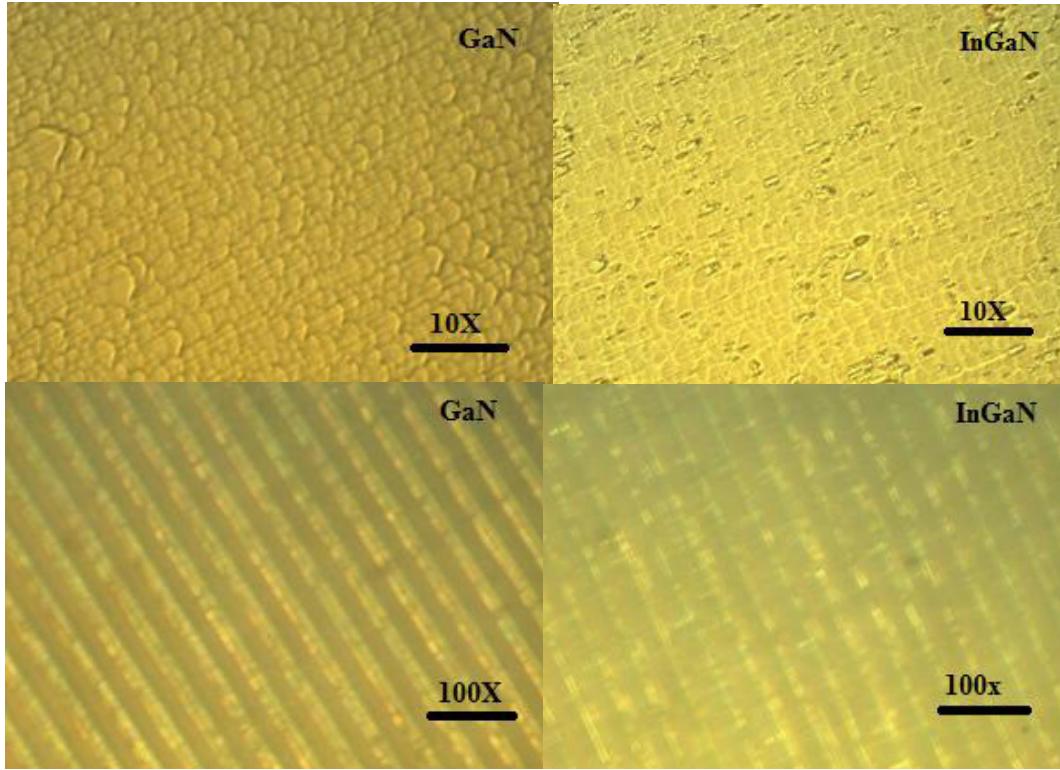


Fig. 2. Optic Microscopy images a)GaN- 10x, b)InGaN- 10x, c)GaN-100x, d)InGaN-100x.

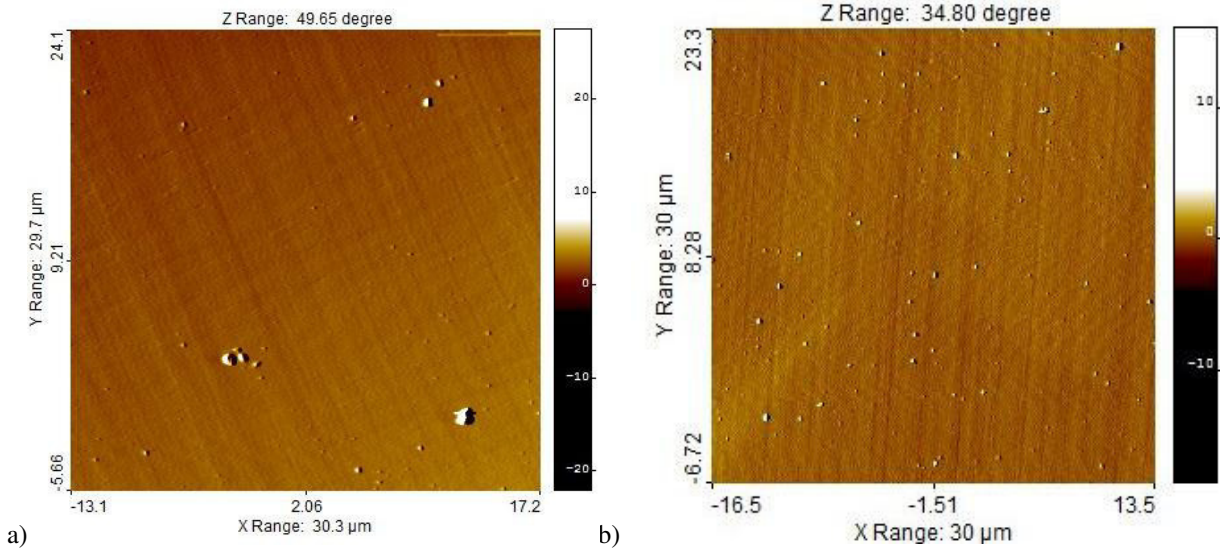


Fig. 3. Atomic force microscopy scans of structures. Morphology and surface defects of semipolar GaN template (left) and InGaN/GaN MQWs heterostructures (right) on $30 \times 30\mu\text{m}^2$ surface area.

The growth of GaN buffer layer on the patterned sapphire substrate was performed by HVPE. The growth was done in a commercial Aixtron single-wafer HVPE system with a horizontal quartz-tube [15, 16]. Approximately 4 μm thick GaN layer has been deposited at a fairly low growth temperature of 900– 970 °C. We called this template “GaN template”.

In the following stage the 5 period InGaN/GaN MQWs heterojunctions have been deposited on the top of HVPE growth GaN by MOVPE. The MOVPE growth was done in a commercial Aixtron-200/4 RF-S HT reactor using the standard precursors: ammonia (NH₃), trimethylgallium (TMGa), trimethylindium (TMIn) and triethylgallium (TEGa). In order to achieve fairly long wavelength above 500 nm, the InGaN MQWs were grown at a temperature of typically 720°C (58 s) , while the temperature was increased by about 35°C for the GaN barrier growth (104 s). At the end of growth process the thin GaN top layer was deposited during 10 second on top of 5 period InGaN/GaN heterojunctions.

3. RESULTS AND DISCUSSIONS

In figure 2, the Optical Microscopy images were described for GaN template and InGaN MWQs. As shown in Fig. 2 c and d the c-directions patterns is visible on GaN before growing InGaN QWs, but after growing InGaN MQWs because of QWs cover on the top of GaN template the pattern lines were disturbed. It is usually accepted that the high defect density in GaN leads to poor optical property and also affects the structural and optical quality of the active layer composed of the InGaN/GaN MQWs. Well-defined, uniform and long crystallographic steps could be observed on the surface by AFM. The undesirable growths with surface hillock can be seen from AFM 2D images (Fig. 3). The intersection of a screw-component dislocation with the film surface creates an atomic step termination that may lead to hillock formation (Burton et al 1951).

The presence of clustered defects with the screw component of the Burgers vector is a reason of formation of the growth hillocks. More growth hillocks located at the top and some pits located away from the hillock peaks, are shown in Fig. 3(a, b). On the top of InGaN QWs the numbers of different kind of hillocks are more than GaN template. It means them come from MOVPE growth conditions. Remarkable morphological differences are noticeable for GaN template and InGaN QWs on the same GaN template.

The semipolar InGaN MQWs have been investigated by TEM. TEM observations were carried out on a cross sectional specimen, i.e. along a direction orthogonal to the growth direction. This is the only way to detect the QW layers individually and measure their individual composition. To this aim two different TEM

operation modes were used, namely HR-TEM (high resolution TEM) and HAADF (high angle annular dark field) modes. The HR-TEM mode is the usual way to get images with atomic resolution, by exploiting the interference of all the electron beams diffracted by the lattice planes of the specimen, according to the Bragg law. In HR-TEM mode the parallel illumination of the specimen is used.

The HAADF mode is instead based on the Rutherford-like scattering, by the atoms of the specimen, of the electrons of the incident beam when it crosses the specimen. Here the TEM electron beam is focused to a small size (0.5-0.7 nm in our case) and is scanned across the sample, like in an SEM: the TEM is operated in the Scanning mode, i.e. STEM mode. Most importantly in our case, the mentioned scattering goes as Z^n , with Z the average atomic number of the investigated region and $1.7 < n < 2$. The higher Z the higher is the scattering angle [18]. The most accepted value is $n=2$. By using a post-specimen annular detector around the TEM optical axis one can collect the scattered beams whose intensity increases with increasing Z. Materials with high average Z give brighter contrast than those with low average Z. HAADF thus gives a chemical information about the specimen (sample) composition.

The InGaN QWs region (including the cap) is between the 2 yellow arrows (Fig 4a, b). The blue encircled bright lines in the GaN beneath the QW layers are very likely twins. Such defects generally originate at the interface (IF) with the substrate. However, it is not possible to confirm this here as the GaN/Al₂O₃ IF is not visible. On this sample the HAADF intensity is proportional to Z^n (Z atomic number of the analysed sample).

Hence it is

$$\begin{aligned} \text{- for In}_x\text{Ga}_{1-x}\text{N} \quad I_{\text{IGN}} &= x Z_{\text{In}}^n + (1-x) Z_{\text{Ga}}^n + Z_{\text{N}}^n \\ \text{- for GaN} \quad I_{\text{GN}} &= Z_{\text{Ga}}^n + Z_{\text{N}}^n \end{aligned}$$

The concentration x of In in an In_xGa_{1-x}N layer can be obtained from the ratio A of the two net experimental intensities,

$$A = I_{\text{IGN}} / I_{\text{GN}}$$

and is given by, for $n=1.7$, $x = 0.915 (A-1)$. Results on x are reported in the table. The error was 7-10%.

This may support the calculations performed on the HAADF images showing a decreasing concentration of In, e.g. from $x=0.197$ to $x=0.200$, from the buffer to the top of the sample. : Intensity profile from bottom to top of the QWs structure along the arrow in numbers help to establish the link between image and profile (Fig 5).

In _x Ga _{1-x} N (Number of QWs)	1	2	3	4	5
X (concentration of In)	0.200	0.209	0.199	0.174	0.197

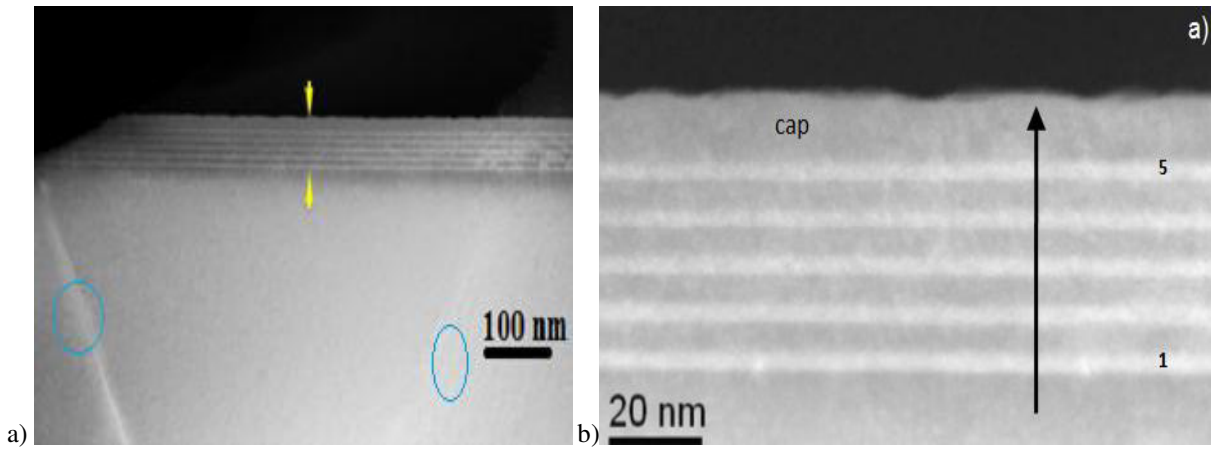


Fig. 4. TEM images: High angle annular dark field (HAADF) scanning transmission electron microscopy (STEM) of semipolar InGaN QWs on the top of GaN template.



Fig. 5. HAADF image: Intensity profile from bottom to top of the QWs structure along the arrow in numbers help to establish the link between image and profile.

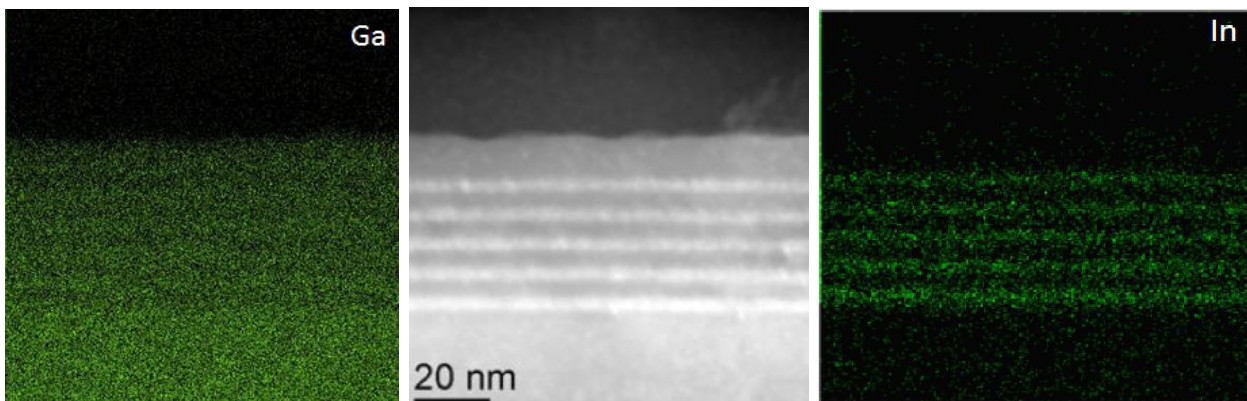


Fig. 6. Energy-dispersive X-ray spectroscopy (X-EDS) maps of InGaN QWs.

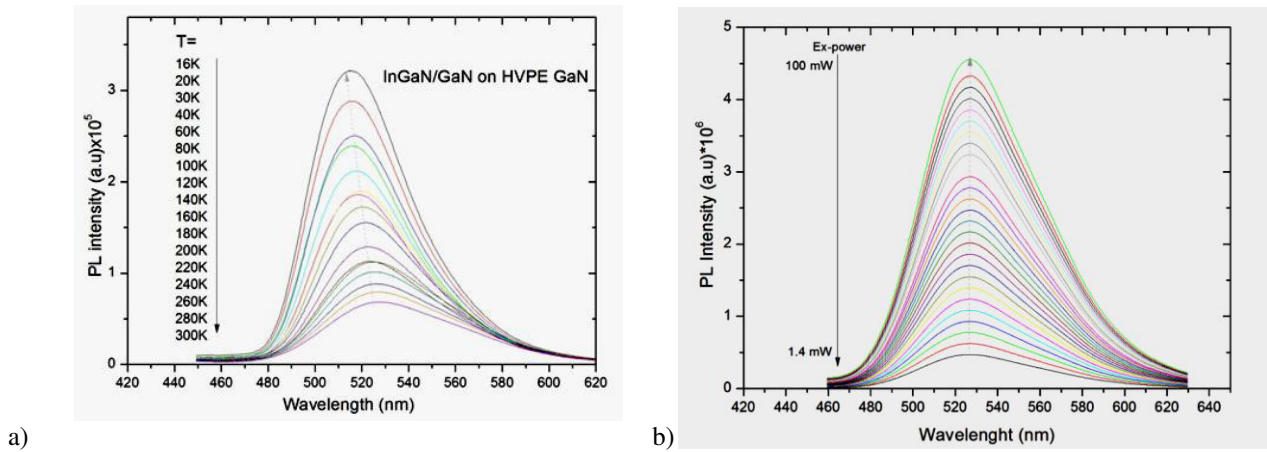


Fig. 7. PL characterization of InGaN QWs sample at different temperatures (a) and excitation power sources (b).

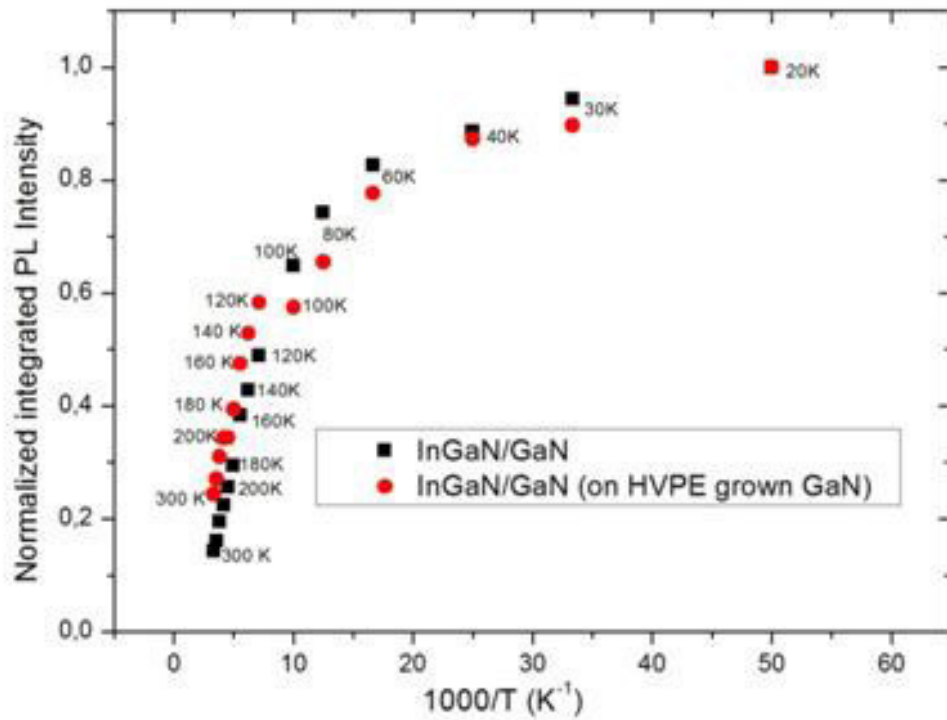


Fig. 8. Arrhenius plot of the normalized integrated PL intensity of InGaN MQWs samples.

X-EDS (Energy-dispersive X-ray spectroscopy) is a method able to give chemical information about the composition of a specimen investigated by TEM. Here the middle image is the HAADF image of the InGaN QWs like the one in fig. 6 a). On the left is the X-EDS map of Ga while on the right is the one of In. Pretty evident is the correspondence between the In rich layers and the 5 brighter layers in the HAADF image, confirming the identification of the brightest layers as InGaN as deduced from the HAADF measurements. A weak depletion of Ga in correspondence of the In rich layers is also detectable. In the X-EDS map for In (right) the 1st InGaN layer from the buffer is brighter than all the others. The other 4 ones are also less and less bright on moving to the top (Fig. 6).

PL emission intensity was significantly decreased linearly with increasing measurement temperature and excitation power respectively Fig. 7a and Fig. 7b. PL peak³.

position is not shifted with increasing excitation source power but shifted with increasing temperature from 16 K to 300 K considerably.

At the end we compared the temperature dependence of the normalized integrated PL intensity of this sample with other InGaN QWs sample with was grown by MOVPE directly. (Fig. 8). The integrated PL intensity falls gradually in two samples with increasing temperature. These results could be explained due to increasing non-radiative recombination path in these structures. Assuming that the internal quantum efficiency (η_{int}) identical and equals unity at 16 K, we obtain η_{int} of 0.15 and 0.24 at room temperature for our current investigated InGaN QWs sample (on HVPE grown GaN/Al₂O₃ template) and other InGaN QWs (grown directly on sapphire by MOVPE) respectively.

4. CONCLUSION

We have investigated surface defects of semipolar GaN template grown on patterned sapphire wafers by HVPE and semipolar InGaN QWs on the top of this GaN/sapphire template. AFM, TEM, X-EDS and PL characterizations were done of QWs. Via microscopic analyzes it has been obtained that on the top of InGaN QWs the numbers of different kind of hillocks are more than GaN template. HAADF images showing a decreasing concentration of In, e.g. from $x=0.197$ to $x=0.200$, from the buffer to the top of the sample. PL peak position is not shifted with increasing excitation source power but shifted with increasing temperature from 16 K to 300 K considerably. The internal quantum efficiency for our current investigated InGaN QWs

sample (on HVPE grown GaN/sapphire template) and other InGaN QWs (grown directly on sapphire by MOVPE) are identical and equals unity at 16 K. At the room temperature the internal quantum efficiency of our current investigated InGaN QWs (on HVPE grown GaN/sapphire template) was higher than second sample, 0.24 and 0.15 respectively.

ACKNOWLEDGMENT

We are grateful to Prof. Dr. Ferdinand Scholz (Ulm University, Germany) for the possibility to carry out the main part of this work in his GaN group at the Institute of Optoelectronic and for him strong technical and scientific support. This work has been partly financially supported by the German Academic Exchange Service (DAAD).

-
- [1] H.M. Kim, T.W. Kang, K.S. Chung. J. Ceram. Proc. Res. 5 (2004) 241–243.
 - [2] H.M. Kim, Y.H. Cho, H. Lee, S. Kim II, S.R. Ryu, D.Y. Kim, T.W. Kang, K.S. Chung. Nano Lett. 4 (2004) 1059–1062.
 - [3] H.M. Kim, H. Lee, S. Kim II, S.R. Ryu, T.W. Kang, K.S. Chung. Phys.Stat. Sol. (b) 241 (2004) 2802–2805.
 - [4] Y. Sun, Y.H. Cho, H.M. Kim, T.W. Kang. Appl. Phys. Lett. 87 (2005), 093115-1-093115-3.
 - [5] F. Qian, S. Gradečak, Y. Li, C.Y. Wen, C.M. Lieber. Nano Lett. 5 (2005) 2287–2291.
 - [6] F. Qian, Y. Li, S. Gradečak, D. Wang, C.J. Barrelet, C.M. Lieber. Nano Lett. 4 (2004) 1975–1979.
 - [7] T.H. Hsueh, H.W. Huang, C.C. Kao, Y.H. Chang, M.C. Ou-Yang, H.C. Kuo, S.C. Wang. J. J. Appl. Phys. 44 (2005) 2661–2663.
 - [8] H. Amano, N. Sawaki, I. Akasaki and Y. Toyoda. Appl. Phys. Lett. 48, 353(1986).
 - [9] S. Nakamura and G. Fasol. The Blue Laser Diode (Springer Verlag, 1997).
 - [10] S. Nakamura. Jpn. J. Appl. Phys. 30, 1348 (1991).
 - [11] Y. Wang, K. Zang, S. Chua, M.S. Sander, S. Tripathy, C.G. Fonstad. J.Phys. Chem. B 110 (2006) 11081–11087.
 - [12] A. Chen, S.J. Chua, P. Chen, X.Y. Chen, L.K. Jian. Nanotechnology 17 (2006) 3903–3908.
 - [13] P. Chen, S.J. Chua, Y.D. Wang, M.D. Sander, C.G. Fonstad. Appl. Phys.Lett. 87 (2005), 143111-1-143111-3.
 - [14] A. Kikuchi, M. Kawai, M. Tada, K. Kishino. J. J. Appl. Phys. 43 (2004) L1524–L1526.
 - [15] G. Pozina, J.P. Bergman, B. Monemar, V.V. Mamutin, T.V. Shubina, V.A. Vekshin, A.A. Toropov, S.V. Ivanov, M. Karlsteen, M. Willander. Phys.Stat. Sol. (b) 216 (1999) 445–450.
 - [16] T. Kouno, A. Kikuchi, K. Kishino. Phys. Stat. Sol. (b) 243 (2006) 1481–1485.
 - [17] Y.H. Kim, J.Y. Lee, S.H. Lee, J.E. Oh, H.S. Lee, Y. Huh. Chem. Phys. Lett. 412 (2005) 454–458.
 - [18] Caliebe, T. Meisch, B. Neuschl, S. Bauer, J. Helbing, D. Beck, K. Thonke, M. Klein, D. Heinz and F. Scholz. Phys. Status Solidi C 11, 525–529 (2014).
 - [19] T. Walther, J. Microsc. 221, 137 (2006) and C. Frigeri et al., Nano. Res. Lett. 6, 194 (2011).
 - [20] H.P. Maruska. Appl. Phys. Lett., vol. 15, no. 10, p. 327, 1969.
 - [21] F. Scholz, M. Caliebe, G. Gahramanova et. al. Phys. Status Solidi B, 2016, v.253, No1, pp. 13–22
 - [22] S. Abdullayeva, G. Gahramanova, R. Jabbarov. Azerbaijan Journal of Physics, 2015, v. XXI, No 4, Section: En, pp. 47-51.
 - [23] S. Abdullayeva, G. Gahramanova, R. Jabbarov, T. Orujov. Azerbaijan Journal of Physics, Volume XXII, No 1, Section: En, 2016, p. 49–51.
 - [24] S. Abdullayeva, G. Gahramanova, Cesare Frigeri, N. Musayeva, R. Jabbarov. International Scientific Conference on Sustainable Development Goals-2017, 24-25 November, Baku, 2017, pp. 391-395

Received:

MAGNETORESISTIVE PROPERTIES OF DIRAC SEMIMETAL Cd_3As_2 FERROMAGNETIC SEMICONDUCTOR AT HIGH PRESSURE

M.M. GADJIALIEV, L.A. SAIPULAEVA, A.G. ALIBEKOV, A.YU. MOLLAEV,
V.S. ZAKHVALINSKY, S.F. MARENKIN, T.N. EFENDIEVA

*Amirhanov Institute of Physics, Dagestan Scientific Centre,
Russian Academy of Sciences, 367003 Makhachkala, Russia*

The composite samples of $\text{Cd}_3\text{As}_2+\text{MnAs}$ (MnAs – 20 mole per cent) are prepared. We investigate the structure of samples using the X-ray powder diffraction, differential thermal, and energy dispersive analyses. The research of electric and magnetic properties of $\text{Cd}_3\text{As}_2+\text{MnAs}$ (MnAs – 20 mole per cent) under high hydrostatic pressure reveals that the phase transitions appear on pressure dependences of the resistivity and the Hall coefficient. Pressure-induced negative magnetoresistance is observed on magnetic-field dependences.

Keywords: composite, ferromagnetic semiconductor, hall effect, magnetoresistance, magnetoresistive properties.

PACS: 61.82.Fk, 62.23.Pq, 62.50.P

INTRODUCTION

A crucial problem is preparation of Cd_3As_2 - based ferromagnetic semiconductors [1, 4, 5]. For instance, Cd_3As_2 with Cr provided the suppression of near zero effective mass ultra-relativistic states at the substitution of Cr atoms for Cd [6].

Manganese dissolves in Cd_3As_2 forming a wide region of triple solid solutions $(\text{Cd}_{1-x}\text{Mn}_x)_3\text{As}_2$. An increase in Mn-content results in formation of Cd_3As_2 – based composite containing MnAs inclusions along with $\text{Cd}_{1-x}\text{Mn}_x)_3\text{As}_2$ solid solution. The MnAs ferromagnetic phase crystallizes on a hexagonal lattice P63/mmc with unit cell parameters $a=3.72$ Å and $c=5.71$ Å. The hexagonal structure of NiAs-type P63/mmc symmetry in MnAs changes to orthorhombic structure of MnP-type Pnma symmetry at room temperature with increasing the pressure up to 0.45 GPa [7].

MnAs compound possesses the ferromagnetism with a Curie temperature 318 K. This makes it a promising material for different elements of the spin electronics operating in a terahertz range [8,9,10]. Solid solutions of diluted magnetic semiconductors $(\text{Cd}_{1-x}\text{Mn}_x)_3\text{As}_2$ possess InSb-type band structure; the forbidden band width at low temperatures follows the linear dependence $E_0 = -0.095+1.45x$ (x is the Mn concentration) [11]. The band structure of Cd_3As_2 semiconductor is studied for long period of time and in series of works the band inversion along with the gapless-state is suggested [12]. The evolution of bands in Cd_3As_2 - based ternary and quaternary solid solutions is attractive as a separate problem [13] and enlightens the understanding of Cd_3As_2 properties as 3D Dirac semimetal [1]. The study of physical parameters dependence of Cd_3As_2 – MnAs system on a composition and pressure allows us to determine the points of Dirac semimetal (DSM) and semiconductor phase transition.

For the first time, in this work we perform complex researches of $\text{Cd}_3\text{As}_2+\text{MnAs}$ crystal structure, MnAs – 20 mole per cent, and an influence of the temperature, magnetic field, and pressure on the charge transport.

METHOD AND TECHNIQUE

The hydrostatic pressure $P \leq 9$ GPa was produced in a toroid-type device improved in such a way as to perform simultaneous measurements for few kinetic coefficients. For the purpose of simultaneous measuring the resistivity, Hall effect, and magnetoresistance, we used a multiturn solenoid allowing for generating the magnetic field of $H \leq 5$ kOe. A fluoroplastic cell of ~ 80 mm³ fitted with 12 electric contacts was used for measuring the resistivity and the Hall effect and pressure control at compression and decompression. A manganin manometer was graduated against Bi, Ti, and other standards. The parallelepiped samples had sizes of $2.8 \times 0.7 \times 0.5$ mm. As a pressure transmitting medium, we used ethanol and methanol mixture (4:1), which is hydrostatic up to 10 GPa. The electrical contacts were made by tin-based solders. The uncertainties in the resistivity, Hall effect, and pressure measurements didn't exceed ± 3 , ± 3.5 , and ± 3 per cents, respectively. A detailed description of the method is presented in [14, 15].

RESULTS AND DISCUSSION

We research the structure of a ferromagnetic semiconductor of $\text{Cd}_3\text{As}_2+\text{MnAs}$ (MnAs – 20 mole per cent) at room temperature by means of PDA, DTA, the energy dispersive analysis (EDA), scanning electron and optical microscopy, and the Raman spectroscopy. The Hall effect, resistivity, and magnetoresistance measurements are performed under hydrostatic pressure up to 9 GPa at room temperatures. Figure 1 depicts the PDA results for $\text{Cd}_3\text{As}_2+\text{MnAs}$ (MnAs – 20 mole per cent). The line diagram of powder pattern shows that the crystal is composite, with prevailed α' -phase of Cd_3As_2 . Previously, Pietraszko, Lukaszewicz [16] reported that relatively high crystallization rates used at the Cd_3As_2 synthesis can be responsible for few inclusions of high-temperature phases of that at room temperature. The same is observed for heavily doped samples, for instance, in $\text{Cd}_3\text{As}_2+\text{MnAs}$ both α' - Cd_3As_2 and α'' - Cd_3As_2 phases were revealed [17]. The diffraction peak for magnetic MnAs phase is clearly determined only in the (101) plane

(Fig. 1) that was confirmed by the scanning electron microscopy (SEM) (see below). Dashed diagrams stand for different polymorphous modifications of cadmium arsenide.

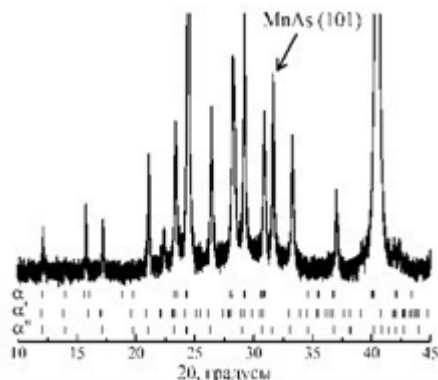


Fig. 1. X-ray patterns of $\text{Cd}_3\text{As}_2+20$ modifications of cadmium arsenide.

The multiphase composition of samples was confirmed when investigating the surfaces by SEM and the confocal microscopy (CM) (Fig. 2).

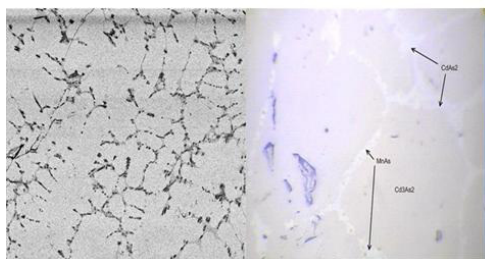


Fig. 2. The SEM (left inset) and confocal microscopy (right inset) images of $\text{Cd}_3\text{As}_2+20$ mole per cent MnAs sample.

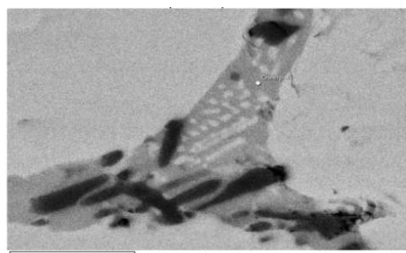


Fig. 3. The enlarged segment of the microstructure pictured in Fig. 2 (left) presents the images of $\text{Cd}_3\text{As}_2+\text{MnAs}$ (MnAs – 20 mole per cent) surface.

The greater part of the sample is homogeneous that, according to the elemental analysis, is corresponded to Cd_3As_2 . Additional inclusions occupy less than 5 per cent of a sample surface area, in which the content of arsenic is higher than cadmium as opposed to the main sample bulk. An enlarged segment of the image (Fig. 2 (left) and Fig.3) clearly displays a complex nature of the inclusion, which in turn contains submicron inclusions similar in composition to Cd_3As_2 . The elemental analysis in a dark area of the inclusion shows a second phase to be CdAs_2 . Since the grown samples are the polycrystals, the

inclusions, apparently, are the eutectic composition of $\text{Cd}_3\text{As}_2 - \text{CdAs}_2$ on the Cd_3As_2 crystallite boundaries. The spreading of manganese in the sample at the submicron level is homogeneous. That means, a part of Mn is dissolved in Cd_3As_2 matrix and, besides the $\text{Cd}_3\text{As}_2 - \text{CdAs}_2$ eutectics, the Mn inclusions are found on crystallite boundaries and don't exceed micrometer dimensions, according to PDA (Fig. 1).

In Fig. 4, we show differential thermal analysis of $\text{Cd}_3\text{As}_2 + \text{MnAs}$ samples. The DTA results for 80 mole per cent $\text{Cd}_3\text{As}_2 - 20$ mole per cent MnAs are interpreted as follows: 584 °C is the temperature of polymorphous transformation $\alpha \rightarrow \beta$ Cd_3As_2 ; 610°C is the melting point of the eutectics; 713 °C is the liquidus point.

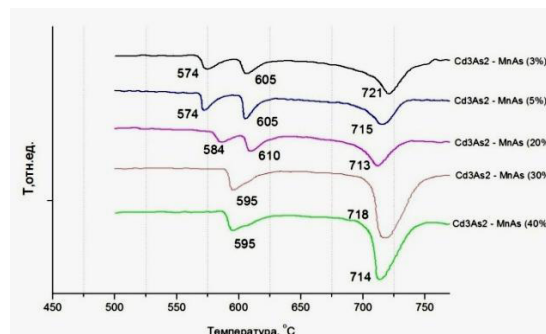


Fig. 4. DTA results of $\text{Cd}_3\text{As}_2 + \text{MnAs}$ samples.

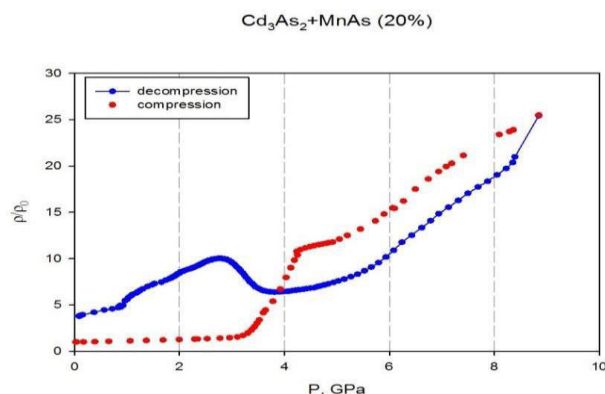


Fig. 5. The resistivity versus pressure curve for $\text{Cd}_3\text{As}_2+20$ mole per cent MnAs under MnAs.

The pressure measurements results for the resistivity, Hall coefficient, and magnetoresistance are depicted in Figs 5,6,7. The pressure dependence of the resistivity and Hall coefficient in $\text{Cd}_3\text{As}_2+\text{MnAs}$ (MnAs – 20 mole per cent) is illustrated in Figs 6, 7.

With increasing the pressure, the resistivity doesn't change up to $P \approx 2.8$ GPa, after that it sharply rises (approximately by a factor of 12) achieving a maximum at $P=4.2$ GPa (Fig. 5). When decreasing the pressure, it drops with different baric coefficients and gains a maximum at $P=2.75$ GPa. The discrepancies in resistivity values before and after pressure application can be associated with the structure of the composite or with a probable second phase transition under $P > 8$, a nature of which needs a further analysis.

The dependence the Hall coefficient $R_H(P)$ on the pressure is illustrated in Fig. 6. The Hall coefficient passes through a maximum up to $P \approx 3.65$ GPa (Fig. 6).

The Hall coefficient versus pressure curve correlates well with the pressure dependence of $\rho(P)$, which also has a clear peak.

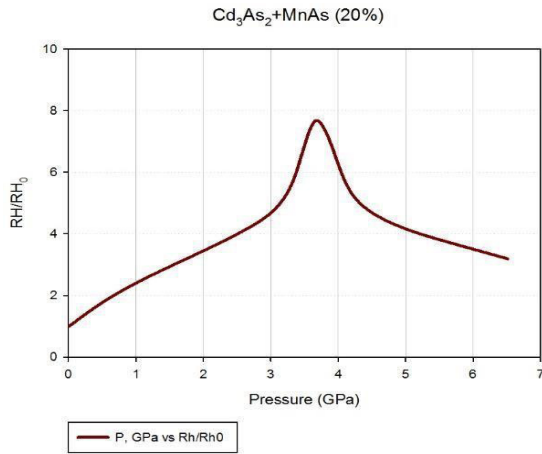


Fig. 6. The pressure dependence of the Hall coefficient for Cd_3As_2 +20 mole per cent compression and decompression.

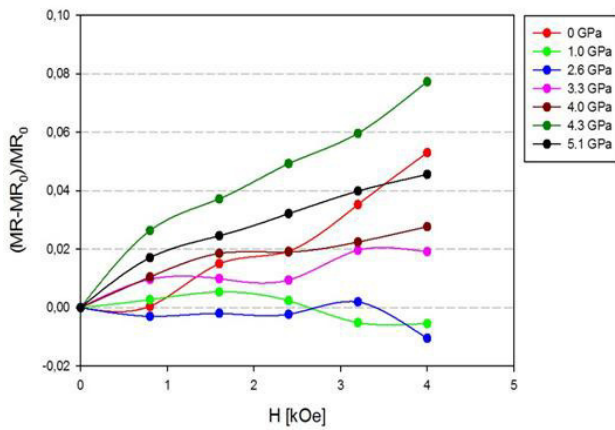


Fig. 7. magnetic field dependence of the magnetoresistivity under fixed pressures.

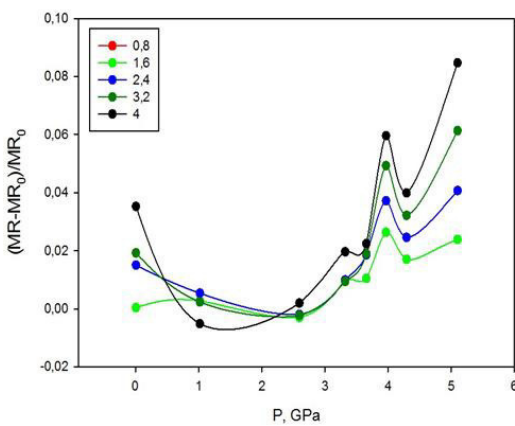


Fig. 8. The pressure dependence of the magnetoresistivity under fixed pressures.

The magnetic field dependence of the magnetoresistance under fixed pressures of $P \approx 0 \div 5.1$ GPa for Cd_3As_2 +MnAs (MnAs–20 mole per cent) is

shown in Fig. 7. The magnetoresistance, positive at zero pressure, is suppressed with increasing the pressure. Starting from $P \approx 1$ GPa and $P \approx 2.6$ GPa, it drops achieving maxima, which shift towards high magnetic fields with raising the pressure.

The magnetoresistance versus pressure curves in Fig. 8. demonstrate a phase transition emerged at $P \approx 4$ GPa, a value of which, on a high pressure scale, agrees with phase transition values on $\rho(P)/\rho_0(P)$ and $R_h(P)/R_{h0}(P)$ curves in Figs 5, 6. The value of the transition maximum on the magnetoresistance versus pressure curve rises with growth in a magnetic field intensity.

CONCLUSION

The values of phase transitions emerged on pressure dependences of the resistivity, Hall coefficient, and magnetoresistance under high pressure agree well with phase transition values on $\rho(P)/\rho_0(P)$ and $R(P)/R_0(P)$ curves. Such a good agreement of experimental pressure dependences can be interpreted by a spin-reorientation magnetic phase transition in intermetallic compound of MnAs resulting from a change in structure parameters under high pressures. It is known, that magnetic and structural properties of MnAs and alloys are closely related [15]. The technology of Cd_3As_2 +MnAs (MnAs–20 mole per cent) synthesis leads to the generation of granular structures (composite), which is a semiconducting (non-magnetic) matrix with ferromagnetic nanoclusters. In Ref. [18], the spin-reorientation transitions in MnAs were revealed on exposure to high pressure. It was determined that the position of manganese atoms in the magnetic cell (by additional superstructure magnetic reflex) at $P = 3.8$ GPa can be described by space group $P21/c$. In ferromagnetic hexagonal MnAs structure under normal pressure and $T_c = 318$ K, the manganese atoms form layers perpendicular to a axis. Manganese nearest neighbor magnetic exchange interactions at 2.85 \AA range in adjacent layers are dominant, while Mn next-to-nearest neighbor interactions inside the layers at about 3.7 \AA range are noticeably weaker. The structural changes induced by hexagonal-to-orthorhombic transition have a little effect on a distance between nearest neighbors, that is about 2.81 \AA at $P = 3.8$ GPa, however, the ranges between next-to-nearest neighbors substantially change to about $2.98, 3.39, 4.43 \text{ \AA}$ at the same pressure. Thus, the observed magnetic phase transition can be explained within the framework of the Kittel model [19] due to the change in sign of Mn next-to-nearest neighbor exchange interactions under compression [20]. Basing on the data of works [2, 3, 20, 21] and our measurements, we can suggest that two phase transitions in Cd_3As_2 and MnAs, emerged in Cd_3As_2 +MnAs (MnAs–20 mole per cent) nanocomposite under high pressure, influence on the carrier transport and the magnetoresistance. The composite matrix is solid $(\text{Cd}_{1-x}\text{Mn}_x)_3\text{As}_2$ due to the subsolution of manganese. The matrix of narrow gap semiconductor and structural phase transition Cd_3As_2 and the spin-reorientation magnetic transition in MnAs nanoclusters contribute to the pressure dependence of the magnetoresistance of Cd_3As_2 +MnAs (MnAs–20 mole per cent).

- [1] A.V. Galeeva, I.V. Krylov, K.A. Drozdov, A.F. Knjazev, A.V. Kochura, A.P. Kuzmenko, V.S. Zakhvalinskii, S.N. Danilov, L.I. Ryabova, D.R. Khokhlov. Electron energy relaxation under terahertz excitation in $(\text{Cd}_{1-x}\text{Zn}_x)_3\text{As}_2$ Dirac semimetals. *Bellstein J. Nanotechnol.* 8 (2017) 167.
- [2] Lanpo He, YatingJia, Sijia Zhang, Xiaochen Hong, Changqing Jin and Shiyang Li. Pressureinduced superconductivity in the three-dimensional topological Dirac semimetal Cd_3As_2 , *npj Quantum Materials*, 1 (2016) 16014.
- [3] S. Zhang, et al. Breakdown of three-dimensional Dirac semimetal state in pressurized Cd_3As_2 . *Phys. Rev. B* 91, 165133 (2015).
- [4] E.K. Arushanov. II_3V_2 Compounds and Alloys, *Prog. Crystal Growth and Charact.* 1992, Vol. 25, pp. 131-201.
- [5] J. Cisowski. Semimagnetic Semiconductors Based on II-V Compounds, *Phys. Stat. Sol. (b)* 200, 311 (1997).
- [6] X. Yuan, P. Cheng, L. Zhang, Ch. Zhang, J. Wang, Y. Liu, Q. Sun, P. Zhou, D.W. Zhang, Z. Hu, X. Wan, H. Yan, Z. Li, F. Xiu. Direct observation of landau level resonance and mass generation in Dirac semimetal Cd_3As_2 thin films *Nano Letters*. 17 (2017) 2211.
- [7] I.F. Gribanov, E.A.Zavadsky, A.P. Sivachenko. The low-temperature transformations in orthorhombic arsenide manganese. *Fiz. Nizkh. Temp.*, 1979, v. 5, pp.1219-1223. (1979).
- [8] C. Spezzani, E. Ferrari, E. Allaria, F. Vidal, A. Ciavardini et. al. Magnetization and Microstructure Dynamics in Fe/MnAs/GaAs (001): Fe Magnetization Reversal by a Femtosecond Laser Pulse *Physical Review Letters*. 2014. V. 113. Iss. 24. P. 247202.
- [9] J. Hubmann, B. Bauer, H.S. Korner, S. Furthmeier, M. Buchner, G. Bayreuther et. al. Epitaxial Growth of Room -Temperature Ferromagnetic MnAs Segments on GaAs Nanowires via Sequential Crystallization *Nano Letters*. 2016. V. 16. iss. 2. p. 900-905.
- [10] V.M. Novotortsev, S.F. Marenkin, I.V. Fedorchenko, A.V. Kochura. Physicochemical Foundations of Synthesis of New Ferromagnets from Chalcopyrites $\text{A}^{\text{II}}\text{B}^{\text{IV}}\text{C}^{\text{V}}_2$. *Russian Journal of Inorganic Chemistry*. 2010. V. 55. No.11. P. 1762-1773.
- [11] M.J. Aubin, L.G. Caron and J.-P. Jay-Gerin. Band structure of cadmium arsenide at room temperature, *Phys. Rev B*. 15, (1977) p.p.3872-3878.
- [12] R.J. Wagner, E.D. Palik, and E.M. Swiggard. In *Physics of Semimetals and Narrow-Gap Semiconductors* D.L. Carter and R.T.Bate, eds.), p.471. Pergamon, New York, 1971.
- [13] E.K. Arushanov, A.F. Knyazev, A.N. Nateprov, S.I. Radautsan. Composition Dependence of the Energy Gap in $\text{Cd}_3\text{-xZnxAs}_2$ *Fiz. Tekh. Poluprovodn.*, 1983, v.17, N7, pp.1202-1204.
- [14] A.Yu. Mollaev, L.A. Saipulaeva, R.K. Arslanov, S.F. Marenkin. Effect of hydrostatic pressure on the transport properties of cadmium diarsenide crystals. *Inorganic Materials*. 2001. V. 37. № 4. P. 327-330.
- [15] L.G. Khvostantsev, L.P.Vereshchagin, A.P. Novikov. *High Temperatures - High Pressures*. 1977. V. 9. № 6. p. 637.
- [16] A. Pietraszko, K. Lukaszewicz. Thermal Expansion and Phase Transitions of Cd_3As_2 and Zn_3As_2 . *Phys. Stat. Sol. (a)*. 1973. V. 18. P. 723.
- [17] A.I. Ril, A.V. Kochura, S.F. Marenkin, A.E. Kuzko, B.A. Aronzon. Crystall Microstructure of $\text{Cd}_3\text{As}_2 - \text{MnAs}$ system, *Proceeding of Southwest State University. Technics and Technologies*, 2017, vol. 7, no. 2(23), pp. 120–134.
- [18] S.K. Asadov, E.A. Zavadskii, V.I. Kamenev, E.P. Stefanovskii, A.L. Sukstanskii, B.M. Todris. Relation of Magnetic and Structural Factors in the Course of Phase Transitions in MnAs- Based Alloys, *Physics of the Solid State*, 2000, Volume 42, issue 9, pp 1696–1704.
- [19] C. Kittel. Model of exchange-inversion magnetization. *Phys. Rev.* -1960. -V. 120. -P. 335- 342.
- [20] D.P. Kozlenko. Magnetic and orientational ordering in systems with competing interactions at high pressures: dis ... Doctor of Physical and Mathematical Sciences, Yekaterinburg, 2008. 350.
- [21] A.D. Izotov, V.P. Sanygin, V.F. Ponomarev. Genetic relation between crystal structures of polymorphic modifications of $\text{A}^{\text{II}}\text{B}^{\text{IV}}_2$ - type compounds. *Crystallography*, 1978, 23, 767. (1978)

Received: 02.04.2018

METHOD TO DETERMINE THE INVERTED LAYER

M.M. GADJALIEV, Z.SH. PIRMAGOMEDOV, T.N. EFENDIEVA,
L.A. SAYPULAEVA

*Amirhanov Institute of Physics, Dagestan Scientific Centre, Russian Academy of Sciences,
367003 Makhachkala, Russia*

The thermoelectromotive force (thermal emf) for p-InSb surface layer of MOS (metal- oxide – semiconductor) structure is calculated depending on the voltage applied to gate. We propose a method for the experimental detection of a gate voltage value, at which the inverse layer appears by a change in a sign of the thermal emf of the semiconductor surface layer.

Keywords: thermoelectromotive force, inverse layer, structure, barrier, gate voltage, length of Debye

PACS: 73.40QV

RESULTS AND DISCUSSION

In light of increasing investigations on electric and thermal properties of semiconductor structures in the recent years, the experimental determination of a field, at which the inverse layer arises from the field effect, remains to be an actual question.

It is known that the inverse layer occurs at the semiconductor surface in the MOS structures when the gate voltage increases [1] in case of:

$$|E_c| \geq \frac{\sqrt{\varepsilon_g kT}}{e \ell_d}, \quad (1)$$

where ε_g is the forbidden band width; k is the Boltzmann constant; T is the absolute temperature; e is the electron charge; ℓ_d is the Debye length.

In this study, we propose a method providing the detection of the value of a field applied to gate, which excites the occurrence of the inverse layer, by changing the thermal emf sign from “+” to “-” for MOS structure prepared on with p -semiconductor.

Since we experimentally did not measure thermal emf in the dependence on the gate voltage, the value of electrons and holes concentrations and corresponding voltage value are taken from work [2].

Authors [2] measured electrical properties of p -InSb MOS structure with $p = 10^{13} \text{ cm}^{-3}$ in the dependence on a gate voltage from 0 to 200 V at 4.2K and reported that the hole concentration decreased in the surface layer from $2 \cdot 10^{13} \text{ cm}^{-3}$ to $3 \cdot 10^{11} \text{ cm}^{-3}$ while the electron concentration increased in the inverse layer from $3 \cdot 10^{11} \text{ cm}^{-2}$ to $7 \cdot 10^{12} \text{ cm}^{-2}$.

We first calculate thermal emf at 4.2K for a volume material p -InSb with $p=10^{13} \text{ cm}^{-3}$ in the dependence on the gate voltage from 0 to 50 V using Pisarenko formula:

$$\alpha(0) = -\frac{k}{e} \left[r + 2 - \ln \frac{4\pi^{3/2} \hbar^3 p}{(m_p kT)^{3/2}} \right], \quad (2)$$

for three concentrations of holes:

$\rho_1 = 2 \cdot 10^{13} \text{ cm}^{-3}$; $\rho_2 = 4 \cdot 10^{12} \text{ cm}^{-3}$; $\rho_3 = 3 \cdot 10^{11} \text{ cm}^{-3}$ (r is scattering mechanism-dependant coefficient, p is the hole concentration, m_p is the effective hole mass, T is the absolute temperature).

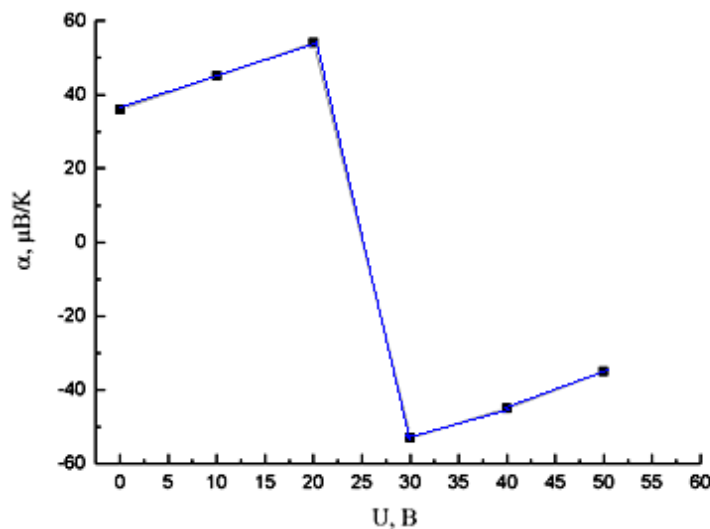


Fig. 1. Dependence of thermal emf of the p -InSb surface layer on the gate voltage of MOS structure estimated at 4.2 K.

Then, thermal emf for three concentrations of electrons was calculated for electrons of degenerate statistics in the inverse layer using formula:

$$\alpha(0) = -\frac{\pi^2}{3}(r+1)\frac{k}{e}\frac{2m_n kT}{(3\pi^2 n)^{2/3}h^2}, \quad (3)$$

$n_1 = 3 \cdot 10^{11} \text{ cm}^{-2}$; $n_2 = 4 \cdot 10^{12} \text{ cm}^{-2}$, $n_3 = 7 \cdot 10^{12} \text{ cm}^{-2}$ (n is the electron concentration, m_n is the effective electron mass). The impurity ion scattering is accepted when calculating thermal emf by Formulae (1) and (2).

Figure 1 depicts estimated values of thermal emf at increasing the voltage up to 50 V.

As the figure demonstrates, hole thermal emf first increases with the decrease of the hole concentration in the surface layer and then that changes the sign at appearance of the inverse layer. Further increasing in the electron concentration results in decreasing in thermal emf due to rise in the electron concentration.

The figure depicts that at a certain gate voltage (in our case ~26 V) a field value, at which the inverse layer occurs, can be detected by measuring thermal emf of the surface layer.

CONCLUSION

For comparison, a field value, at which the inverse layer appears, is determined from Formula (1). According to Formula (1) the transverse field of beginning the inverse layer generation is of 912 V/cm at semiconductor thickness of 0.04 cm and at gate voltage of 36 V. The difference of a field value, at which the inverse layer appears, obtained at experimental measurement of thermal emf using both methods will disappear with increasing in experimental points. The goal of the study is to show that the occurrence moment of the inverse layer in MOS structure can be accurately determined by this method.

[1] *T. Ando, A.B. Fowler, F. Stern. Revs Mod. Phys.*, 1982, v. 54, p. 437;

[2] *K.F. Komatsubara, H. Kamioka, Y. Kabayana. J. Appl. Phys. Lett.*, 1969, **40**, 2940.

Received: 28.03.2018

ELECTRON STRUCTURE OF GRAPHENE BASED MATERIAL

ARZUMAN G. GASANOV, AZAD A. BAYRAMOV

War College of Armed Forces of the Azerbaijan Republic

E-mail: hasanovarzuman@hotmail.com

In the paper, the theoretical models of shockproof material based on double layers graphenes have been constructed, and the electronic structure has been investigated by using semi empirical Extended Hukkel method, which is one of the variant of molecular orbital method. Based on the theoretical models the orbital energies, ionization potentials, full electron's energies etc. of graphene-based materials have been calculated. These materials can be used in military area, for example, for bulletproof vest making.

Keywords: Mathematical modeling, graphene, quantum mechanical methods, shockproof material, electronic structure.

PACS: 03.65.Ge; 71.15.Ap; 61.48.Gh

INTRODUCTION

Consuited by carbon atoms a graphene is presented as one atom thickness layer in hybridized sp^2 state and 2D-crystal lattice connected by σ and π bands [1]. In the graphene level carbon atoms are connected each of other by strong covalent band. Three carbon's valent electrons of four are taken part in formation of σ -band, and one of them is taken part in formation of π -band. The overlap of electron's cloud in π -band state is less than in σ -band. Therefor, the π -bands are broken easily and π -electrons move in lattice around all atoms' nucleuses. And it provides a conductivity of graphene.

Graphene has a very interesting band structure. Its conduction band crosses a valent band in 6 points. It provides graphene possession of many electron properties. Graphene is a semiconductor without pores. In the same time, the finite energy pore is formed in crossed points of conductivity and valent bands, that is, graphene has a property of little pore semiconductor. And this, like a quantum well, is connected with graphene possession of planar heterostructure and at low temperature it creates a possibility to use this energy pore as energy barrier.

Graphene has a high hardness [2, 3, 4]. These properties provide to use graphene in wide areas, and now it is very interesting to investigate of graphene based shockproof material. At this point of view, an investigation of graphene based materials by theoretical methods is very interesting and necessary.

In the presented paper, the theoretical models of two layers graphene based material have been constructed and its electron structure has been investigated by semiempiric extended Hückel method (EHM).

THEORETICAL METHODOLOGY

The mathematical modelling and quantum-mechanical investigation of graphene based shockproof materials are carried out usually by molecular orbitals (MO) method [5-11]. It is known, that semiempiric EHM is one of the simple semiempiric variant of the MO method. In MO the state of the electron is described with one electron wave function so-called molecular orbital. In according of MO method each electron in molecule moves in certain effective field created by atoms and electrons of molecules not depended on other electrons. The electron's state in molecule is described by one

electron wave function (molecule orbital) [8, 9, 12]. These functions are multicentered ones. That is, its expressions include a distance of electrons from nucleuse of various atoms.

There are various variants of seaching of the molecule's orbites. The MO LCAO method of the seaching of U_i molecule orbits as the atoms' orbits linear combination is one of them [11]:

$$U_i = \sum_{q=1}^m c_{qi} \chi_q \quad (1)$$

Here: c_{qi} are unknown factors, χ_q are atoms' orbits as basis functions. In (1) equation Gauss functions were used as χ_q atoms' orbits [13]. c_{qi} - factors are determined from solution of below equations system:

$$\sum_q (H_{pq} - \varepsilon_i S_{pq}) c_{qi} = 0 \quad (2)$$

Here:

$$H_{pq} = \int \chi_p^* \hat{H}_{ef} \chi_q dV \quad (3)$$

$$S_{pq} = \int \chi_p^* \chi_q dV \quad (4)$$

S_{pq} are overlap integrals between χ_p and χ_q atom orbits. \hat{H}_{ef} is effective Hamiltonian for one electron moved irrespective of other electrons in effective field created by molecule:

$$\hat{H}_{ef} = -\frac{1}{2} \nabla^2 + U(r). \quad (5)$$

The full formule of $U(r)$ is unknown, therefore, it is impossible to cakculate H_{pq} . These values are evaluated by use some experimental parameters. In EHM H_{pq} matrix diagonal elements are taken equal to ionization potential of atom valent state with opposite sign [13].

$$\begin{aligned}(1s | H | 1s) &= -0.499786 \text{ amu} \\ (2s | C | 2s) &= -0.772096 \text{ amu} \\ (2p | C | 2p) &= -0.419161 \text{ amu}\end{aligned}\quad (7)$$

The nondiagonal elements of H_{pq} are calculated by Wolfsberg – Helmholtz method [7,11]:

$$H_{pq} = 0.5 \cdot K \cdot S_{pq} (H_{pp} + H_{qq}) \quad (8)$$

k is determined by comparison of experimental facts or by condition of energy minimum. In given work it was taken $k = 1.75$. The equation (2) is linear homogeneous equations' system. Bu tənliklər məlum qaydalara əsasən həll olunaraq The values of \mathcal{E}_i and C_{qi} are determined by

solution of equations' system (2). By using of \mathcal{E}_i values for graphen based materials we can calculate the full electron energy, ionization potentials, and investigate mechanical, electrical, magnit properties.

RESULTS AND DISSCUSIONS

In given paper we have calculated orbital energy, ionization potentials, full electron energies of hraphene $C_{62}H_{20}$ and two layers graphene $C_{124}H_{40}$ [14] by semiempiric EHM. The dependence of orbital energies \mathcal{E} on atom mass for two layers graphene $C_{124}H_{40}$, when the distance between layers is taken as $D=0.142$ nm, is shown in figure 1.

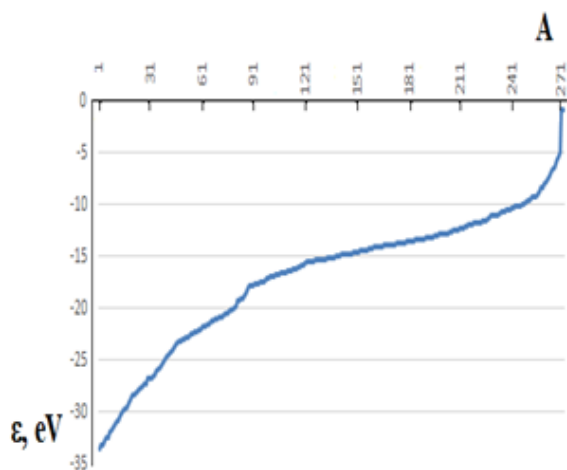


Fig. 1. The dependence of orbital energies \mathcal{E} on atom mass for two layers graphene $C_{124}H_{40}$.

As we can see from figure 1, the dependence till $A=257$ is expressed by formule

$$\mathcal{E} = -b_1 \exp(-b_2 A) \quad (9)$$

here: b_1 and b_2 are some factors.

Bu, when beginning from $A=257$ (it is Fermiy element and its electron structure of $5f^{12}6d^07s^2$) the curve is sharply down, that is, the law (9) is broken.

In presented paper, there is a graphene fragment consisted of 62 carbon atoms in each layer. The edges of fragment are locked by 20 hydrogen atoms.

For each object, electrons are located two by two on energies levels beginning of lowest level. It was determined trapped by electrons the highest molecular orbital energy \mathcal{E}_{HOMO} and the lowest empty molecular

orbital energy \mathcal{E}_{LUMO} . There is an ionization potential

formule $I_p = -\mathcal{E}_{HOMO}$, a band gap formule $E_g =$

$\mathcal{E}_{LUMO} - \mathcal{E}_{HOMO}$ and a strength parameter formule

$$\eta = \frac{1}{2} E_g \text{ [5-11].}$$

The wavelength of radiated photon of this material is

calculated by formula $\lambda = \frac{c \cdot h}{1.6 \cdot E_g} \cdot 10^{28} \text{ nm}$. Here: h

is the Planck constant, c is the speed of light in vacuum.

When λ is calculated then the values of E_g in eV are used. It is considered that when $\eta < 1$ eV the material is soft and when $\eta > 1$ eV one is solid.

The stability of material is calculated by formula

$$\Delta E = E - \sum_A E_A \text{ [11-14]. Here: } E \text{ is total energy of}$$

system, E_A is total energy of A atom in system and ΔE is a parameter characterizing the stability of system. It is considered that when $\Delta E > 0$ the material is unstable and when $\Delta E < 0$ one is stable. The results are presented in table 2.

The theoretical models of graphene fragment of $C_{62}H_{20}$ are shown in figure 2: a-by lines, b-by lines and spheres, c-by spheres. The theoretical models of two layers graphene fragment of $C_{124}H_{40}$ are shown in figure 3: a-by lines, b-by lines and spheres, c-by spheres. From comparison of figures 2 and 3 we can conclude that two layers graphene is more hard than one layer one.

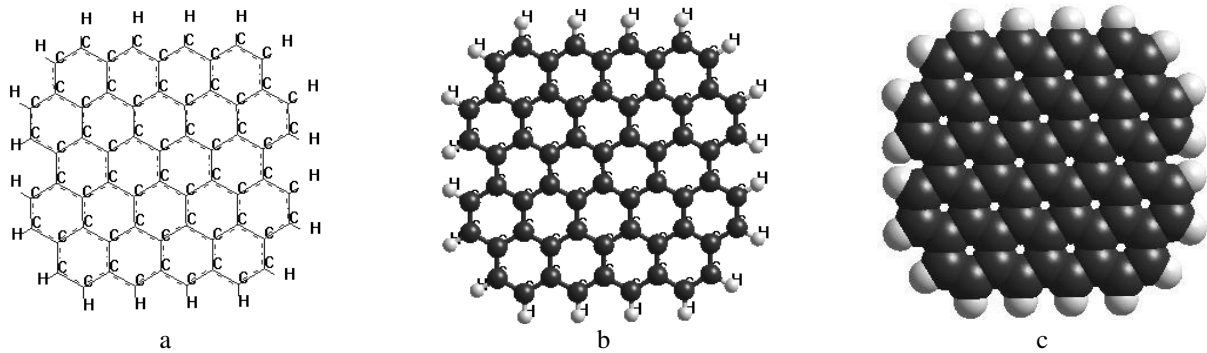
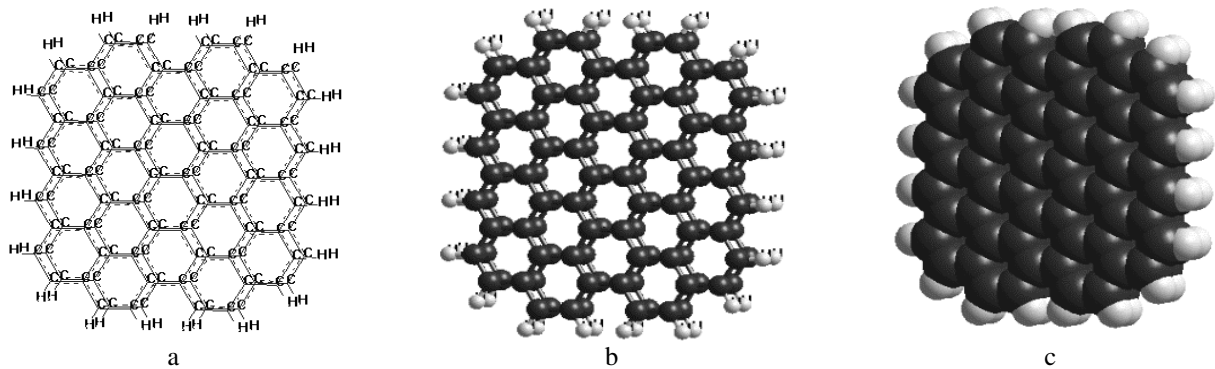
From analysing of table 2 data we can conclude that when the distance between two layers' graphene of $D=1.42$ nm then a band gap of $E_g=4.1$ eV and a strength parameter of $\eta=4.05$ eV are maximal, but a wavelength of radiated photon of $\lambda=303$ nm is minimal. The strength of two layers' graphene is much than one layer one in 5 times. Therefore, the distance between two layers' graphene we must take $D=1.4$ nm that we get very strength material (for example, for making bullet-proof vest).

In the paper, the theoretical models of shockproof material based on double layers graphenes have been constructed, and the electronic structure has been investigated by using semiempirical Extended Hukkel method, which is one of the variant of molecular orbital method. Based on the theoretical models the orbital energies, ionization potentials, full electron's energies etc. of graphene-based materials have been calculated. These materials can be used in military area, for example, for bulletproof vest making.

Table 1

The results for graphene $C_{62}H_{20}$ and two layers graphene $C_{124}H_{40}$

N	Object	Distance between graphene layers D, (nm)	ϵ_{HOMO}	ϵ_{LUMO}	Total energy E (amu)	Stability parameter ΔE (amu)	Ionization potential I_p (eV)	Band gap E_g (eV)	Strength parameter η (eV)	Wavelength of radiated photon λ (nm)
1	$C_{62}H_{20}$	--	-11,026847	-10,275221	-174,9572207	-126,7	11,03	0,751	0,375	1654
2	$C_{124}H_{40}$	1	-4,36267	-3,256325	-318,5881452	0,3	4,36	1,106	0,553	1124
3	$C_{124}H_{40}$	1.3	-5,164615	-1,469666	-332,7678576	-13,8	5,16	3,694	1,847	336
4	$C_{124}H_{40}$	1.35	-5,083723	-1,180737	-334,0786411	-15,2	5,08	3,902	1,951	319
5	$C_{124}H_{40}$	1.39	-5,012462	-0,969388	-334,9979235	-16,1	5,01	4,043	2,021	307
6	$C_{124}H_{40}$	1.4	-4,96414	-0,913609	-335,1862996	-16,3	4,96	4,050	2,025	307
7	$C_{124}H_{40}$	1.41	-4,957228	-0,869326	-335,4035616	-16,5	4,96	4,087	2,043	304
8	$C_{124}H_{40}$	1.42	-4,927879	-0,82677	-335,5958942	-16,7	4,93	4,101	2,050	303
9	$C_{124}H_{40}$	1.425	-4,957231	-0,869326	-335,4035653	-16,5	4,96	4,087	2,043	304
10	$C_{124}H_{40}$	1.43	-4,897443	-0,990988	-335,7814412	-16,9	4,90	3,906	1,953	318
11	$C_{124}H_{40}$	1.45	-4,814208	-1,476756	-336,115703	-17,2	4,81	3,337	1,668	372
12	$C_{124}H_{40}$	1.5	-4,640948	-2,741458	-336,8882522	-17,9	4,64	1,899	0,949	654
13	$C_{124}H_{40}$	2.0	-9,49594	-9,114124	-344,3934082	-25,5	9,49	0,381	0,190	3256
14	$C_{124}H_{40}$	2.5	-10,530632	-10,252486	-348,5339434	-29,6	10,53	0,278	0,139	4469
15	$C_{124}H_{40}$	2.7	-10,869238	-10,20065	-349,2005579	-30,3	10,87	0,668	0,334	1859
16	$C_{124}H_{40}$	2.8	-10,839393	-10,342786	-349,4107495	-30,5	10,84	0,496	0,248	2503
17	$C_{124}H_{40}$	2.9	-10,751153	-10,468167	-349,5493439	-30,6	349,54	0,282	0,141	4393
18	$C_{124}H_{40}$	3.0	-10,687812	-10,562207	-349,6521241	-30,7	10,69	0,125	0,062	9897

Fig. 2. The theoretical models of graphene $C_{62}H_{20}$: a-lines, b-lines and spheres, c-spheres.Fig. 3. The theoretical models of two layers graphene $C_{124}H_{40}$: a-lines, b-lines and spheres, c-spheres.

CONCLUSION

In the paper, the theoretical models of the electron structure of two layers graphenes $C_{124}H_{40}$ have been investigated by using semiempirical Extended Hukkel method. The calculated results have shown that the strength of two layers graphene material is depended on

distance between layers. When this distance is equal $D = 0.142$ nm then graphene based material is electrophile, semiconductive, stable and the strength of two layers' graphene is much than one layer one in 5 times. These materials can be applied in various areas, for example, for bulletproof vest making.

-
- [1] Grafen. <https://ru.wikipedia.org/wiki>
- [2] J.S. Bunch et. al. Electromechanical Resonators from Graphene Sheets Science 315, 490,(2007)
- [3] D.A. Abanin, S.V. Morozov, L.A. Ponomarenko, R.V. Gorbachev, A.S. Mayorov, M.I. Katsnelson, K. Watanabe, T. Taniguchi, K.S. Novoselov, S.L. Levitov, A.K. Geim. Giant Nonlocality Near the Dirac Point in Graphene. – Science. – 15 April 2011: Vol. 332 №. 6027 pp. 328–330
- [4] Ali R.Ranjbartoreh, Bei Wang, Xiaoping Shen and Guoxiu Wang. Advanced mechanical properties of graphene paper. – Journal of Applied Physics. – 109, pp. 014306-014312 (2011).
- [5] A.G. Gasanov, M.A. Ramazanov, F.G. Pashaev, M.R. Vahabova. Mathematical modeling of electron structure of $PP+(PbS)_8+(CdS)_9$ nanocomposite by semiempiric PM3 method. FIZIKA. Vol. XXIII, №3, Section: Az, October 2017, pp. 9-13
- [6] A.G. Gasanov, A.A. Bayramov, E.G. Hashimov. Mathematical modeling of the electron structure of SiO_2 nanoparticle. FIZIKA. Vol. XXIII, № 1, Section: En, April, 2017, p.34-39.
- [7] A.G. Gasanov, M.A. Ramazanov, F.G. Pashaev. Mathematical modelling and investigations of argentine sulphide nanoparticles. FIZIKA Vol. XXIII, № 2, Section: Az July, 2017, s.3-6.
- [8] A.M. Maharramov, M.A. Ramazanov, A.G. Gasanov, F.G. Pashaev. The Study of Silver Nanoparticles in Basis of Slater Functions // Physical Science International Journal. 10(3): 1-6, 2016.
- [9] M.A. Ramazanov, F.G. Pashaev, A.G. Gasanov, A.M. Maharramov, A.T. Mahmood. The quantum mechanical study of cadmium sulfur nanoparticles in basis of STO's // Chalcogenide Letters, V11(7), 359-364. (2014).
- [10] F.G. Pashaev, A.G. Gasanov and A.T. Mahmood. The Study of Gold Nanoparticles in basis of Slater Functions // J. Nano. Adv. Mat., V 2(1), 35-41. (2014).
- [11] A.G. Gasanov. Mathematical modelling and computer investigation of graphene. BDU reports, phys.-mathm. Ser., № 2, 2011, pp.171-179.
- [12] A.G. Gasanov, F.G. Pashaev. The Computer Program for the Study of Nanoparticles in Basis of Slater Atomic Orbitals. Romanian Journal of Information Science And Technology Volume 19, Number 4, 2016, 331–337.
- [13] V.I. Minkin, B.Y. Simkin, R.M. Minyaev. Theory of structure of molecule. Rostov at Don, Feniks, (2010).
- [14] K.S. Novoselov, E. McCann, S.V. Morozov, V.I. Falko, M.I. Katsnelson, U. Zeitler, D. Jiang, F. Schedin, A.K. Geim. Unconventional quantum Hall effect and Berry's phase of 2in bilayer grapheme. Nature Physics. 2006. Vol. 2. pp. 177—180.

Received: 16.04.2018

ELECTRON MOBILITY IN $\text{Ge}_{1-x}\text{Si}_x$ ($0 \leq x \leq 0.13$) CRYSTALS COMPLEX DOPED BY $\langle \text{Ga}, \text{Sb}, \text{Ni} \rangle$ IMPURITIES

E.M. ISLAMZADE¹, Z.A. AGAMALIYEV², G.H. AJDAROV¹

¹ *Institute of Physics of Azerbaijan NAS, AZ 1143, H.Javid ave., 131, Baku, Azerbaijan*

E-mail: zangi@physics.ab.az

² *Baku State University, AZ 1148, Z.Khalilov str., 23, Baku, Azerbaijan*

E-mail: zohrab@physics.ab.az

The temperature dependences of electron ohmic mobility in complex doped crystals $\text{Ge}_{1-x}\text{Si}_x \langle \text{Ga}, \text{Sb}, \text{Ni} \rangle$ ($0 \leq x \leq 0.13$) in interval 77 – 300K are defined on the base of Hall coefficient and electric conduction measurements. The concentration order of shallow impurities in matrix is $\sim 10^{16} \text{cm}^{-3}$. It is seen that experimental data by free electron mobility in crystals after sample thermal treatment at 1000 – 1050K well coincide with calculative data taking under consideration the electron scattering on phonons, melt disorders, fully ionized impurities Ga, Sb, Ni and additional thermoinduced acceptor complexes.

Keywords: Ge, Ge-Si, complex doped, mobility, electroactive complexes.

PACS: 81.10.Aj

INTRODUCTION

The mobility of free charge carriers in semiconductors is the one of fundamental parameters characterizing the material. The value of mobility of electrons and holes in matrix is defined by concrete material structure band and interaction character of free charge carriers with lattice atom heat oscillations and series of crystal structure defects. The investigations of mobilities of (μ_e) electrons and (μ_h) holes in crystal solid solutions Ge-Si are carried out by many authors [1-5]. The change regularities μ_e and μ_h in dependence on temperature at phonon and melt scattering of free charge carriers in these crystals in wide temperature interval [4] are defined. The experiments are carried out mainly with samples doped by small impurity centers with concentration of $10^{14} - 10^{15} \text{cm}^{-3}$ order. In works [6,7] it is shown that experimental data on mobility of free charge carriers in complex doped crystals $\text{Ge}_{1-x}\text{Si}_x$ ($0 < x < 0.13$) with presence of cuprum multi-acceptor impurity and small impurity centers with their general concentration by $10^{16} - 10^{17} \text{cm}^{-3}$ order well coincide with calculated data taking into consideration three-fold acceptor behavior in matrix. Note that Ge-Si solid solutions with Si content up to 13% in reference are called germanium-like ones. This is connected with the fact that the conduction-band bottom in these crystal compositions forms by valleys in crystal-graphical directions /111/ as in germanium.

In recent work [8] the investigation results of main impurity state spectrum in complex doped crystals with presence of rapid diffusing doubly charged acceptor impurity Ni and shallow impurities Ga and Sb with concentration of 10^{16}cm^{-3} order. It is shown that thermal treatment of such samples at different T in 650-800⁰ C interval leads to appearance of additional acceptor complexes (AC) including the atoms of Ni and Ga impurities. The activation energy of these complexes depends on $\text{Ge}_{1-x}\text{Si}_x$ crystal composition and is described by the expression $E_{AC}^x = E_v + (75 + 420x) \text{meV}$.

EXPERIMENT AND DISCUSSION

The results of experimental data analysis of electron mobility temperature dependences in $\text{Ge} \langle \text{Ga}, \text{Sb}, \text{Ni} \rangle$ complex doped crystals and germanium-like compositions of $\text{Ge-Si} \langle \text{Ga}, \text{Sb}, \text{Ni} \rangle$ solid solutions taking into consideration of twofold acceptor action of nickel impurity and appearance of additional acceptor complexes in matrix are given in the present work.

The purpose of the work is definition of experimental temperature dependences of electron mobility in complex doped $\text{Ge}_{1-x}\text{Si}_x$ ($0 \leq x \leq 0.13$) crystals by $\langle \text{Ga}, \text{Sb}, \text{Ni} \rangle$ impurities and establishment of quantitative interpretation possibility of obtained results within the framework of existing theories and conceptions taking into consideration the additional acceptor complexes and electron scattering on twofold ionized nickel impurities.

Ge crystals and germanium-like solid solutions Ge-Si with Si content up to 13 at% doped simultaneously by Ga and Sb are grown by modernized Bridgman method [8]. The concentration of both impurities in crystals is of 10^{16}cm^{-3} order. The doping of samples by nickel is carried by diffusion method at temperature corresponding to impurity maximum solubility in Ge-Si (875 -900⁰C) crystals. The measurement of temperature dependences of Hall coefficient and sample electric conduction in 77-300K interval is carried before and after their doping by Ni and following thermal treatments at 750-800⁰C.

At each temperature the samples are kept during a time which causes the presence of equilibrium state (3-4 hours [8]). The quenching is carried out by sample "disposal" in ethyl alcohol at dry ice temperature. The free electron concentration and their ohmic mobility in samples are defined using the data by electron Hall coefficient in Ge and corresponding compositions Ge-Si [4].

Sb, Al and Ni levels reveal in dependence on initial concentration of Ga and Sb impurities in samples after their doping by Ni at 875-900⁰C. Here we consider only that samples, which before and after Ni doping and following thermal treatments at 750-800⁰C, have electron conduction caused by excess concentration of Sb impurity under total concentration of all acceptor levels.

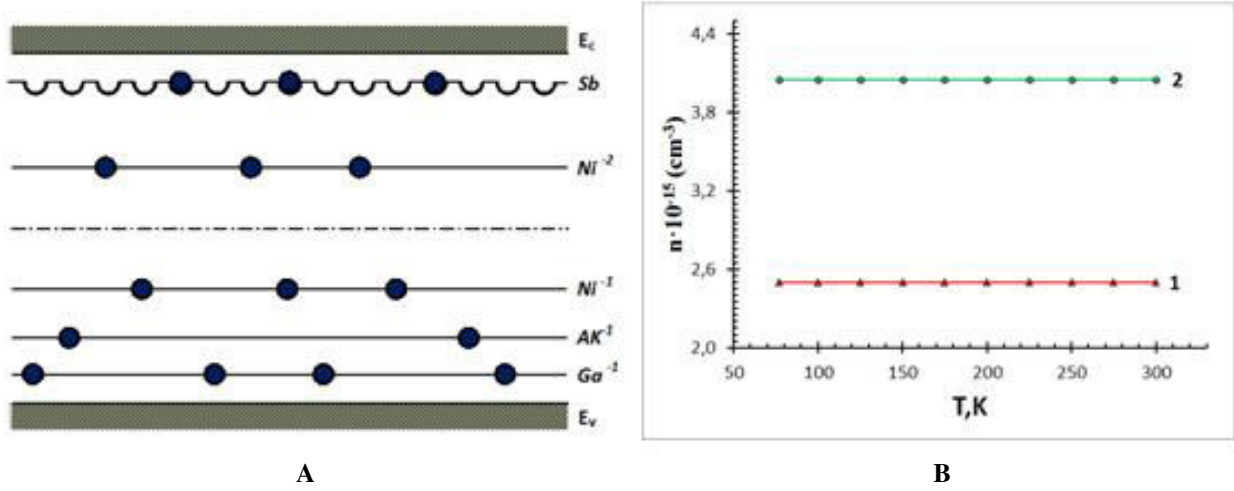


Fig.1. **A** is electron distribution scheme at $T=0$ on impurity energy levels in Ge and Ge-Si crystals complex doped by impurities Ga, Sb, Ni and thermoinduced AC with indication of center charge states; **B** is temperature dependences of free electron concentrations in $\text{Ge}\langle\text{Ga,Sb,Ni,AK}\rangle$ (1) and $\text{Ge}_{0.9}\text{Si}_{0.1}\langle\text{Ga,Sb,Ni, AK}\rangle$ (2) crystals.

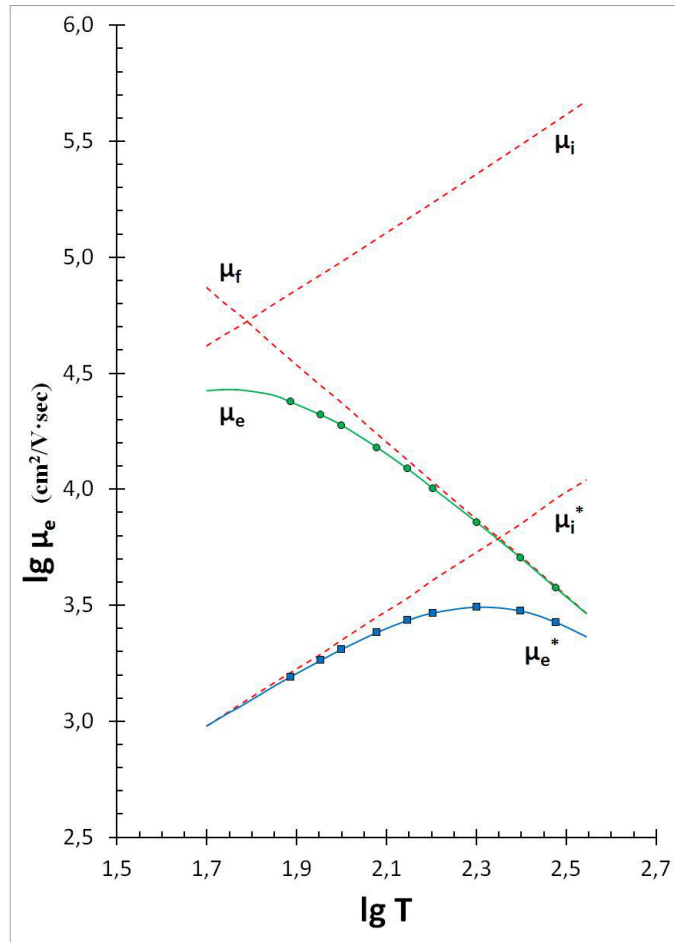


Fig.2. Temperature dependences of electron mobility in $\text{Ge}\langle\text{Sb}\rangle$ crystals with $N_{\text{Sb}}=2.5 \cdot 10^{15} \text{ cm}^{-3}$ (μ_e) and $\text{Ge}\langle\text{Ga, Sb, Ni, AK}\rangle$ ones with $N_{\text{Sb}}^*=2.3 \cdot 10^{15} \text{ cm}^{-3}$ (μ_e^*). In complex doped crystal: $N_{\text{Sb}}=5.1 \cdot 10^{16} \text{ cm}^{-3}$, $N_{\text{Ga}}=4.25 \cdot 10^{16} \text{ cm}^{-3}$, $N_{\text{Ni}}=3.1 \cdot 10^{15} \text{ cm}^{-3}$ and $N_{\text{AK}}=2.05 \cdot 10^{15} \text{ cm}^{-3}$. The signs are the experimental data. The dotted and solid lines are the calculated data. The solid lines are resulting mobilities μ_e and μ_e^* ; dotted lines are mobilities at electron scattering on phonons (μ_f) and ions of the impurities (μ_i and μ_i^*).

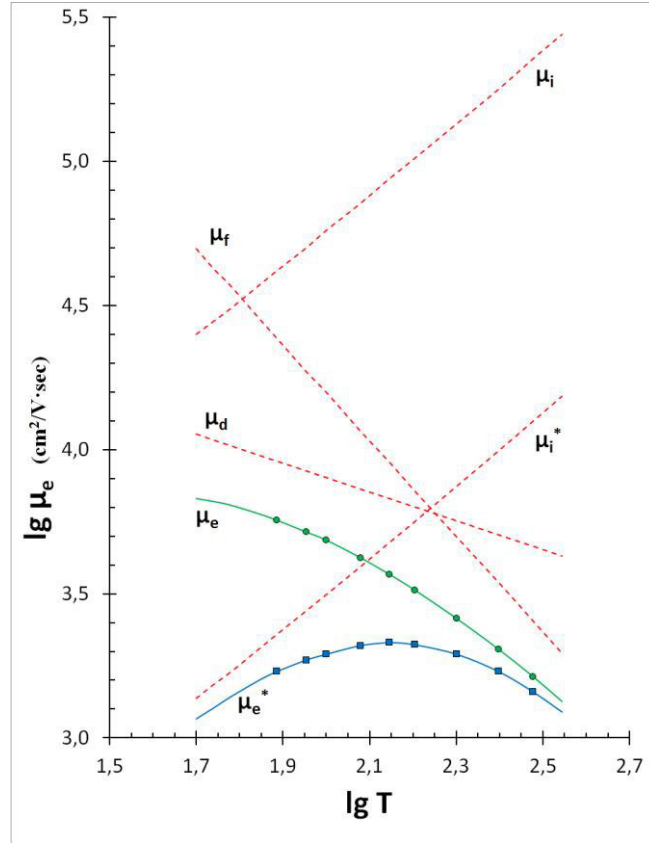


Fig.3. Temperature dependences of electron mobility in $\text{Ge}_{0.9}\text{Si}_{0.1}\langle \text{Sb} \rangle$ crystals with $N_{\text{Sb}} = 4.05 \cdot 10^{15} \text{ cm}^{-3}$ (μ_e) and $\text{Ge}_{0.9}\text{Si}_{0.1}\langle \text{Ga}, \text{Sb}, \text{Ni}, \text{AK} \rangle$ with $N_{\text{Sb}}^* = 3.1 \cdot 10^{15} \text{ cm}^{-3}$ (μ_e^*). In complex doped crystal $N_{\text{Sb}} = 3.55 \cdot 10^{16} \text{ cm}^{-3}$, $N_{\text{Ga}} = 2.92 \cdot 10^{16} \text{ cm}^{-3}$, $N_{\text{Ni}} = 2.18 \cdot 10^{15} \text{ cm}^{-3}$ and $N_{\text{AK}} = 1.95 \cdot 10^{15} \text{ cm}^{-3}$. The signs are the experimental data. The dotted and solid lines are the calculated data. The solid lines μ_e and μ_e^* are resulting mobilities; dotted lines are mobilities at electron scattering on (μ_f) phonons, (μ_d) melt defects and (μ_i , μ_i^*) impurity ions.

In this connection the scheme presented in Fig.1A is put in foundation of interpretation of μ_e temperature dependence experimental data in crystals. In these crystals the electric conduction in investigated temperature region is carried out mainly because of Sb impurity ionization with effective concentration

$$N_{\text{Sb}}^* = N_{\text{Sb}} - (N_{\text{Ga}} + 2N_{\text{Ni}} + N_{\text{AK}}).$$

Fig.1B shows the characteristic temperature dependences of free electron concentration in such crystals on example of Ge and $\text{Ge}_{0.9}\text{Si}_{0.1}$ samples. As it is seen in the given temperature interval all Sb atoms in matrix are totally ionized in connection with enough small activation energy of this impurity ($\sim 0.01 \text{ eV}$ [4]) and electron concentration in conduction band stays practically constant.

The results of μ_e temperature dependence experimental measurements in Ge and $\text{Ge}_{0.9}\text{Si}_{0.1}$ crystals correspondingly are presented by signs on fig.2 and 3. For comparison the dependences for both crystals doped by only Sb impurity with N_{Sb} concentrations and corresponding complex doped crystals with Sb effective concentrations of the same order are given on these figures. In spite of

proximity of free electron concentrations in each from couples of Ge and $\text{Ge}_{0.9}\text{Si}_{0.1}$ crystals the electron mobility in them essentially differs. It is observed in low-temperature region.

The interpretation of experimental data by electron mobility in samples is carried out taking into consideration the fact that phonons and ions of impurities in Ge, in $\text{Ge}_{0.9}\text{Si}_{0.1}$ and melt disorders are the main scattering mechanisms of free charge carriers in considered temperature region [1,3]. It is known that electron mobility in Ge and Ge-like compositions Ge-Si at scattering on (μ_f) phonons in investigated region is the temperature power function and is described by following expression [3,4]:

$$\mu_f = A_x \cdot T^{-1.66} \quad (1)$$

The mobility (μ_d) limited by electron scattering on melt disorders in solid solutions is also described by power dependence on T [1,3]:

$$\mu_d = B_x \cdot T^{-0.5} \quad (2)$$

The coefficients A_x and B_x are constant for each composition and are the following: $A_0=4.9 \times 10^7$ for Ge [4], $A_{0.1}=3.35 \times 10^7$ and $B_{0.1}=8.0 \times 10^4$ for $\text{Ge}_{0.9}\text{Si}_{0.1}$ [4].

The electron mobility in matrix at scattering (μ_i) ion impurity is defined by Brooks-Herring formula [9] taking into consideration ion Coulomb field screening by free electrons:

$$\mu_i = \frac{64\pi^{1/2}\varepsilon^2(2kT)^{3/2}}{(\sum N_i Z_i^2)e^3 m_e^{*1/2}} \left[\ln \frac{24m_e^* k^2 T^2 \varepsilon}{e^2 \hbar^2 n} \right]^{-1} \quad (3)$$

Here N_i and Z_i are concentration and charge state degree of each impurity and additional AC; ε is matrix dielectric constant; m_e^* is density effective mass of electron state. In concrete cases considered by us all Ga, Sb atoms and AC are in one-fold ionized state. Ni atoms in whole temperature interval are charged negatively with degree equal to 2 and their concentration is equal to Ni atoms substituting at T annealing [8].

The temperature dependences of electron mobility in samples at their scattering on phonons and impurity ions in Ge and in $\text{Ge}_{0.9}\text{Si}_{0.1}$ at their scattering on melt defects are shown by dotted lines in fig.2 and 3. The calculated curves of (μ_e) resulting electron mobility shown in

figures by dotted lines are calculated by following formula based on additivity of different electron scattering mechanisms:

$$\frac{1}{\mu_e} = \frac{1}{\mu_f} + \frac{1}{\mu_d} + \frac{1}{\mu_i} \quad (4)$$

As it is seen these curves coincide with corresponding experimental data on electron temperature dependence in both sample couples. The analogous results are obtained by us for all Ge-like compositions of Ge-Si solid solutions.

CONCLUSION

Summarizing the obtained data of electron mobility in $\text{Ge}_{1-x}\text{Si}_x$ ($0 \leq x \leq 0.13$) crystals complex doped by $\langle \text{Ga}, \text{Sb}, \text{Ni} \rangle$ impurities in which the additional AC appear, one can make the following conclusion: the experimental data on free electron mobility in $\text{Ge}_{1-x}\text{Si}_x \langle \text{Ga}, \text{Sb}, \text{Ni} \rangle$ crystals in 77-300 K interval after sample thermal treatment at 1000 – 1050K well coincide with calculated ones taking into consideration the electron scattering on phonons, melt defects, fully ionized impurities Ga, Sb, Ni and also therminduced AC.

-
- [1] M. Glicksman. Phys. Rev., 1958, v.111, p. 125.
 - [2] S. Ishida, E Otsuka. J. Phys. Soc. Jap., 1968, v.24, p. 509.
 - [3] G.Kh. Azhdarov, N.A. Agaev, R.A. Kyazimzade. Sol. State Commun., 1992, v. 84, p. 445.
 - [4] R.A. Kyazimzade. Dis. dok. Fiz-mat. nauk. 1998, s. 272. (In Russian).
 - [5] P.G. Ajdarov, Z.M. Zaxrabekova, Z.M. Zeynalov. Fizika, 2007, t. 13, s 327. (In Russian).
 - [6] L.A. Guseynli, Z.M. Zeynalov, V.K. Kyazimova, G.H. Ajdarov. Transactions of Azerbaijan Academy of Sciences, Series Physical and Technical Sciences, Physical-mathematical and Technical Sciences, Physics and Astronomy, 2011, t. 31, s. 12.
 - [7] G.H. Ajdarov, V.K. Kyazimova, Z.M. Zeynalov, S.O. Mamedova. Transactions of Azerbaijan Academy of Sciences, Series Physical and Technical Sciences, Physical-mathematical and Technical Sciences, Physics and Astronomy, 2008, t. 28, s. 161. (In Russian).
 - [8] E.M. Islamzade, Z.A. Agamaliyev, Z.M. Zaxrabekova, G. Kh. Azhdarov. Grystallography Reports, 2010, v.55, p.462.
 - [9] R. Smit. «Poluprovodniki», Moskva, IL, 1962, s. 467. (In Russian).

Received: 16.04.2018

HIGH-PLASTIC TRANSITION IN THERMOELEMENTS ON GeTe-Co₂Ce EUTECTIC BASE

A.A. MAGERRAMOV, K.Sh. KAKHRAMANOV, K.G. KHALILOVA

aydinm842@yandex.ru

Institute of Physics of Azerbaijan NAS, AZ 1143, H.Javid ave.,131, Baku, Azerbaijan

The level of mechanical stresses developing in thermoelements (TE) at heating and cooling is significantly decreased at the use of semiconductor-metal eutectics as intermediate between GeTe and Co because of eutectics transition into plastic state at comparatively low temperature ($T=600\text{K}$). The weakening of physical bond inside crystals of each phase, highly-stressed state of eutectic satiety by its vacancies and dislocations causes the high atomic diffusion mobility and is the reason of superplasticity effect.

Keywords: thermoelements, semiconductor-metal eutectics, plastic state, phase change materials

PACS: 68.37, 68.35.bg, 68.35.Dv, 68.35.Ja, 68.37.Ps.

INTRODUCTION

Last years the big successes in formation of thermoelectricity physical bases have been achieved, the high-effective crystals on the base of nano-structuring and intercalation have been obtained [1-5]. The transformers for electro-generation and solid-state cooling developed on this base are widely used in science and technology. As it is known, $A^{\text{IV}}B^{\text{VI}}$ compounds are used as materials for medium-temperature thermoelements (TE); $A_2^{\text{VB}}B_3^{\text{VI}}$ and their solid solutions are used for low-temperature ones [3-6].

It is required to form the reliable coupling, i.e. it is necessary to supply the chemical, mechanical and electric compatibility of contact and work materials for improvement of TE characteristics and approximation of their parameters to calculated ones [7-8]. The metals from transition group Ni, Co and Fe having the big melting temperature and high values of electric and heat conductions are used at TE coupling by conducting materials.

EXPERIMENT AND DISCUSSION

The difference of thermal expansion coefficient and big fragility of materials consisting in TE cause the strong revealing of inverse elastic aftereffect indirectly after both their formation and in work process at hot junction temperatures 700-900K that leads to its body cracking and complete destruction.

In connection with above mentioned the possibility use of GeTe - Co₂Ge system eutectic alloy in the capacity of layer coupling in TE is shown by us. The complex investigations in wide temperature interval on study of thermoelectric, mechanical and thermal properties of eutectics, their adhesion ability in relation to semiconductor and metal are necessary to carry out.

GeTe and Sb₂Te₃ belong to class of pseudo-binary alloys $(\text{GeTe})_m - (\text{Sb}_2\text{Te}_3)_n$ which are called phase change materials (PCM) because of ability to transit from crystal state into amorphous one.

Nowadays PCM are used for preparation of different types of optical rewritable random. The potential possibilities of energy-dependent electron random formation on PCM base are highly estimated [8].

Let's consider the role of nanostructuring in TE transit layers. The limits of increase of Z quality factor parameter and W power of thermoelectric materials (TEM) at nano-structuring are defined in [9]. It is shown that Z and W parameters of nano-structures (NS) change because of $\lambda_{\text{ph}} \rightarrow \alpha$ and $\lambda_e \rightarrow \alpha$ transitions in TEM (α is interatomic spacing, λ_{ph} and λ_e are average length of free path of phonons and electrons in samples).

It is revealed that $\lambda_e \rightarrow \alpha$ transition in $1 \sim \lambda_{\text{ph}} / \alpha < \lambda_e / \alpha < 2 - 3$ interval can be used for simultaneous increase of Z and W of thermoelectric materials. It is established that nano-structuring thermoelectric materials can effectively work in maximum power mode in force thermoelectric energy transformations [9]. The mismatch of Z and W parameters in TEM by optimal concentration of current carriers, increase of electric and thermal resistances of contacts, also the development of diffusion instability leads to undesirable processes and add the diffusion phenomena in metal-semiconductor transitions [7].

The formation of high-plastic transition for TE branches (TEB) on base of GeTe-eutectic GeTe - Co₂Ge satisfying to physical-chemical bases of TE coupling is the aim of the work. The reasons of plasticity rapid increase in eutectic melts and other similar systems are very multiform ones and are mainly connected with change of atom electron structure near interphase.

If the values of strength and yield point take the intermediate position between components consisting in it, then this is no observed for plasticity. The plasticity with temperature increase strongly increases and already at $T > 600\text{K}$ transforms into superplastic state (Fig.1).

The thermoelectric properties of GeTe - Co₂Ge system eutectic composition Co = 1,39 at%, Ge = 49,81 at%, Te = 48,8 at% (GeTe=98,67 height%, Co₂Ge=1,33height%) and $T_{\text{mel}}=1000\text{K}$ are considered for further analysis. The thermo-e.m.f., electric conduction, heat conduction and their temperature dependences are studied; the measurements are carried out on controlled oriented samples.

As the samples are two-phase ones then generalized "G" electric conduction, "α" thermo-e.m.f. and "α" heat conduction are measured (see fig.2, fig.3). Having G and $Z = 0,6 \cdot 10^{-3} \text{ grad}^{-1}$ values at temperatures 600-950K GeTe - Co₂Ge alloy eutectic makes the significant contribution in TE efficiency. Thermo-e.m.f. sign for GeTe - Co₂Ge eutectic is positive one.

This is very important as this eutectic is used for TE coupling. GeTe - Co₂Ge eutectic saves its high value of electric conduction in whole temperature interval (600-900K) and its thermo-e.m.f. practically doesn't change. The striving of eutectic atom components in interface to interaction is accompanied by coalescence of different phase crystal lattices on more profitable crystallographic planes.

This causes the oriented and dimensional correspondence in different phase atom disposition in near-boundary layer, high regularity and fineness of eutectic structure, mechanical strength and high-temperature strength of interface.

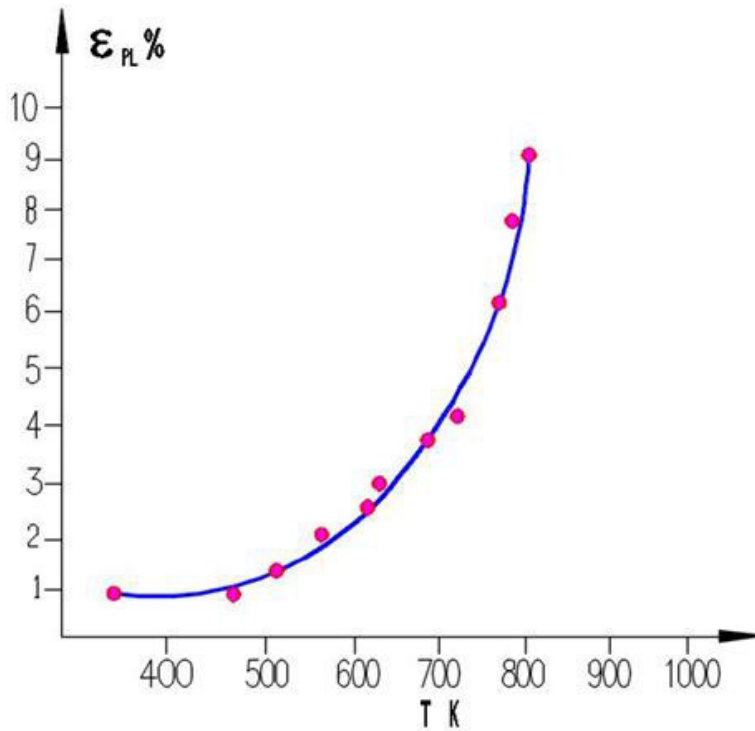


Fig.1. Temperature dependence of plasticity ϵ_{pl} % of GeTe - Co₂Ge eutectic.

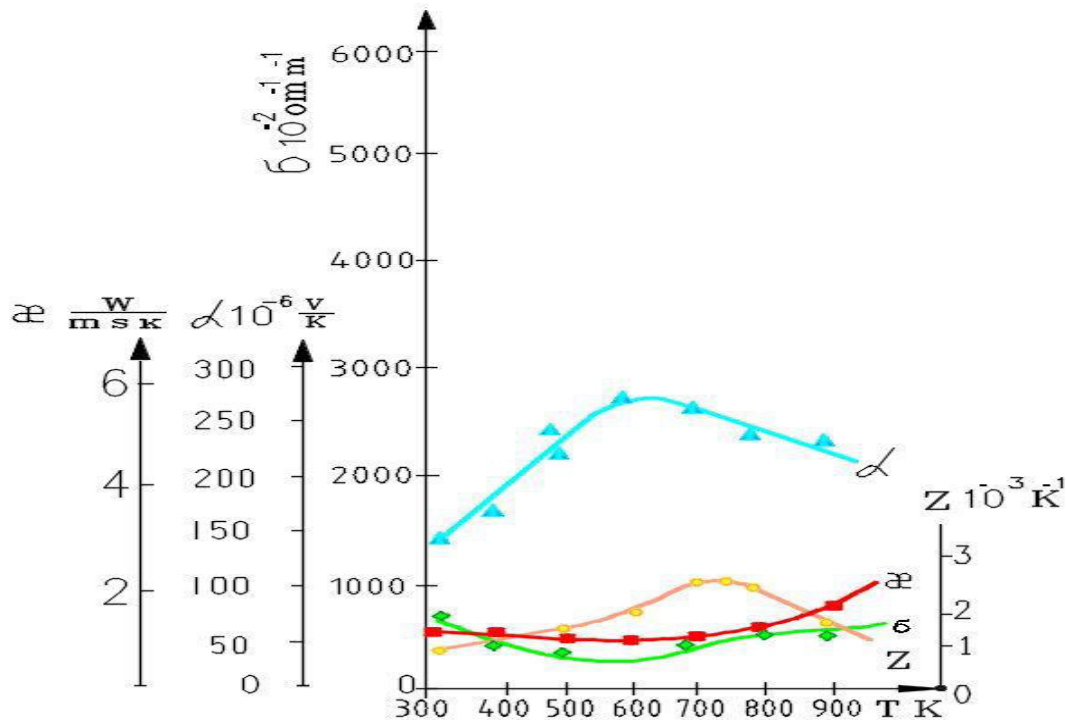


Fig.2. Temperature dependence of thermoelectric properties of TE positive branch on GeTe base.

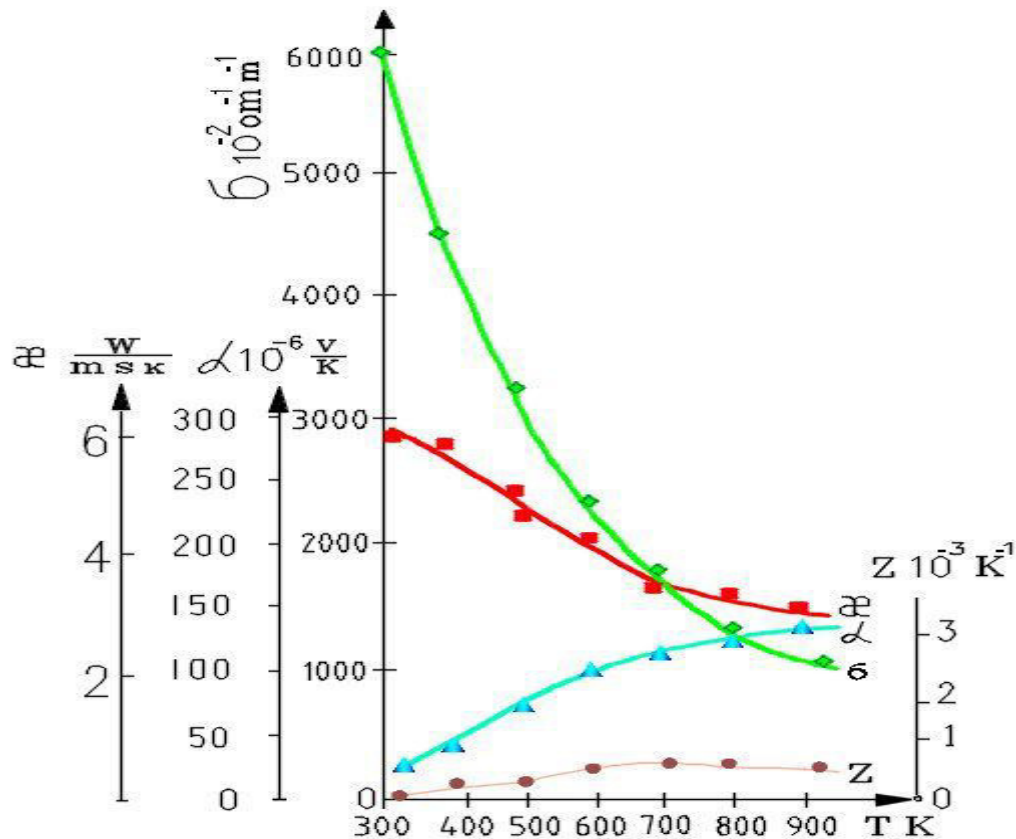


Fig.3. Temperature dependence of thermoelectric properties of GeTe - Co₂Ge eutectic.

The semicoherence of interface boundary caused by mismatch of crystal lattices causes the high-stressed state of eutectic alloy and its saturation by vacancies and dislocations that in collection with decrease of valence electron bond energy inside each phase is the reason of revealing of superplasticity effect in eutectic.

The principle of thermoelement branch coupling consisting in use their eutectic intermediate interlayer between semiconductor and mechanic current distributor that allows us to exclude the chemical interaction in thermoelement near-contact region, supply the strength contact with small thermal and electric losses, decrease the mechanical stresses appearing in thermoelement in process of its work at $T_B = 900\text{K}$ is supposed on the base of complex investigation of electron structure, physicochemical, thermoelectric, heat and mechanical properties of eutectic alloys of Co- Ge-Te system. This causes the oriented and dimensional correspondence in atom disposition of different phases in near-boundary layer, high regularity and fineness of eutectic structure, mechanical strength and high-temperature strength of interface.

CONCLUSION

Analyzing the experimental data one can make the following conclusion:

1. the linear dependence saving in temperature interval 300-800K is observed in diagram two-phase part of composition-property dependence for strength, hardness, yield point at compression, thermal expansion coefficient and thermoelectric parameters;

2. it is experimentally observed that $\epsilon_{PL}\%$ strong increase is observed in eutectic of GeTe - Co₂Ge system at temperature increase higher 650K. The eutectic transforms into superplastic state at higher temperatures;

3. the striving of eutectic atom components to chemical interaction is accompanied by coalescence of different phase crystal lattices on more profitable crystallographic directions. This is the reason of high regular and fine-dispersed eutectic structure and also high mechanical strength of interface.

- [1] F.K. Aleskerov, S.Sh. Kaxramanov, K.Sh. Kaxramanov. Sb. Termoelektriki I ix primeneniye, 2015, Sankt-Peterburq. (In Russian).
- [2] F.K. Aleskerov, K.Sh. Kaxramanov, S.Sh. Kaxramanov. Neorqan. materiali, 2012, t. 48, №5, str. 1-6. (In Russian).

- [3] B.M. Golchman, V.A. Kutasov, L.N. Lukyanova. FTT, 2009, t. 51, vip.4, str.706-708. (In Russian).
- [4] S.Sh. Kaxramanov, F.K. Aleskerov, K.Sh. Kaxramanov, S.A. Nasibova, S.B. Bagirov. Massoperenos v sloistix kristallax tipa $A_2B_3^{VI}$ <primes> Sb. Termoelektriki i ix primeneniye, 2014, str. 1-6. (In Russian).

- [5] *F.K. Aleskerov, K.Sh. Kaxramanov*. Metallofizika. Noveyshie Tekhnologii (Ukraina), 2008, t. 30, № 11, str. 1465-1477. (In Russian).
- [6] *F.K. Aleskerov, S.B. Bagirov, S.Sh. Kaxramanov, G. Kavei*. Transactions of Azerbaijan National Academy of Sciences: Series of physical-mathematical and technical sciences. Physics and Astronomy. 2010, №5, p. 52-55. (In Russian).
- [7] *K.Sh. Kaxramanov, M.I. Zargarova, A.A. Magerramov*. Izvestiya AN SSSR, seriya Neorganicheskie materialy, 1981, t.17, №1, str 43-47. (In Russian).
- [8] *V.G. Orlov, G.S. Sereev*. Fizika tverdogo tela. 2017, to 59, vip. 7, str. 1278-1285. (In Russian).
- [9] *M.A. Korjuev*. Termoelektricheskie nanostrukturi. Za I protiv. Termoelektrichestvo, 2013, № 5, str. 11-24. (In Russian).

Receved:23.04.2018

STUDY OF SPACE STRUCTURE OF DIPPU- AST5 MOLECULE

L.I. VELIYEVA, E.Z. ALIYEV

Baku State University

Lala_Veliyeva@rambler.ru

The space structure of Dippu-AST5 molecule belonging to allatostatin family is established in work by theoretic conformation analysis method. The stability quantitative estimation of possible molecule conformation states in conditions of dipolar medium is carried out on the base of calculation of intramolecular conformation energy.

Keywords: neuropeptides; structure; conformation-dynamic properties

PACS: 87.80.-y

INTRODUCTION

The investigations of structure and conformation dynamics of Dippu-AST5 [1-4] allatostatin molecule are carried out in the given work by molecular mechanics method on the base of step-by-step approach described in works [5-9]. The molecule primary structure is the linear sequence of eight amino-acid residues H-Asp1-Arg2-Leu3-Tyr4-Ser5-Phe6-Gly7-Leu8-NH₂ (DRLYSFGL) and consists in the residues with aromatic rings in positions 4 and 6 of peptide chain. The molecule also consists in the two residues with charged functional groups on ends of its side chains. This are negatively charged carboxyl group of asparaginic acid residue (Asp1) and positively charged guanidine group of arginine (Arg2). The presence of volume side chain with branching at C^γ-atom in (Leu3, Leu8) lysine residues can significantly influence on interconnection of conformation states of main and side chains of Dippu-AST5 allatostatin molecule.

CALCULATION RESULTS AND DISCUSSION

The molecular model and graph of step-by-step calculation of separate fragments of Dippu-AST5 allatostatin molecule is given in Fig.1. The molecule

space structure is studied on the base of stable metal-amid conformations of N-acetyl- α -amino-acids taking under consideration the different orientations of their side chains. The step-by-step calculation of Dippu-AST5 allatostatin molecule space structure consists in the study of conformation states of sequentially extensible fragments according to graph given in Fig.1,b.

The forms of main chain R and B are considered at calculation of Asp1-Arg2-Leu3 tripeptide fragment for asparaginic acid as these forms are isoenergetic ones for molecule first residue. The forms of its main chain R,B and L are considered for lysine residue in position 3 of peptide chain and values of side chain dihedral angles(χ_1 , χ_2) are equal to 60, 180 and -60° before procedure of conformation energy minimization. The values of χ_2 angle in side chain of Tyr4 and Phe6 residues are equal 90°. The general number of low-energy conformation states calculated for fragments Asp1-Arg2-Leu3, Leu3-Tyr4-Ser5-Phe6 and Phe6-Gly7-Leu8 is 171, 1215 and 324 correspondingly. The values of fragment conformation relative energy chosen for further calculation of overlapping parts of Dippu-AST5 allatostatin molecule in dependence on peptide chain length vary in limits 0÷5 kcal/mol.

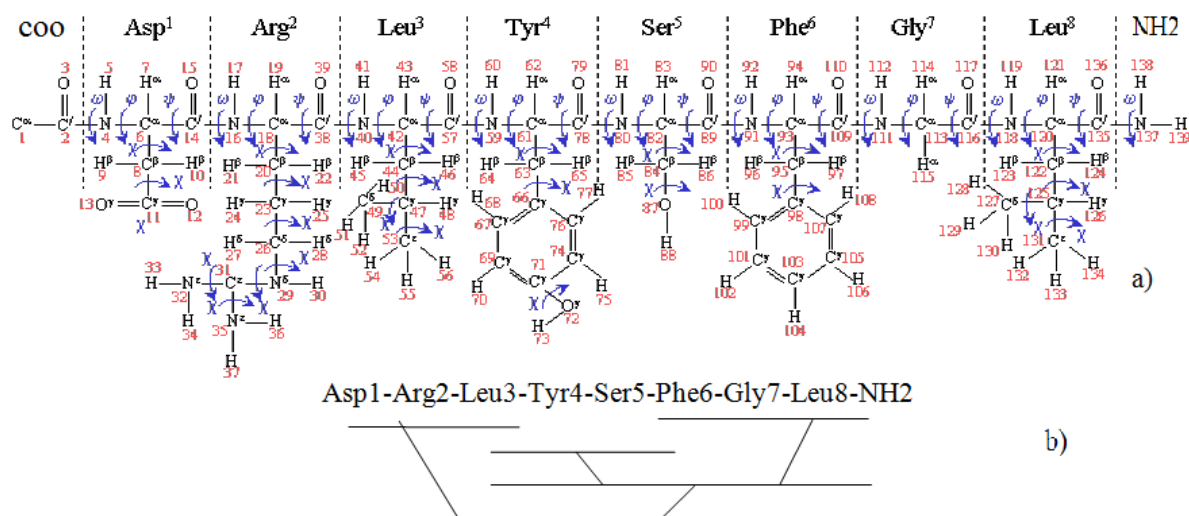


Fig.1. Molecular model, alternatives of dihedral angles (a) and calculation scheme (b) of stable Dippu-AST5 molecule conformations.

STUDY OF SPACE STRUCTURE OF DIPPU-AST5 MOLECULE

As it is followed from calculation results, the more than half of acceptable conformations on tripeptide fragments Asp1-Arg2-Leu3 (58,9%) belong to *fe* shape with semi-folded form of peptide chain. The preference of these structures is caused by effective interactions of side chains of oppositely charged side chains of arginine and asparaginic acid residues.

As a whole the sum contribution from energy of non-valence and electrostatic interactions of these residues in low-energy conformations vary in limits 5,1÷7,8 kcal/mol. The general number of low-energy conformations of tripeptide chosen for further step of calculations is 39.

The shape conformations *eef* and *eff* are the energy profitable ones for Leu3-Tyr4-Ser5-Phe6 tetrapeptide fragment. The stable structures with energy local minimums of this fragment are mainly stabilized by non-valence interactions of residues with aromatic side chains Tyr4 and Phe6 (5,0 kcal/mol order). β -bend on Leu3-Phe6 section at which the distance between C $^{\alpha}$ -atoms of Tyr4 and Phe6 residues are equal to 5,4 Å. Such bend corresponds to approximation and almost parallel disposition of residue aromatic rings so that the distance between ring centers of gravity varies in limits 4,2÷4,5Å. The presence of serine residue consisting in the hydroxyl group in side chain defines the specifics of spatial

structure of Dippu-AST5 allatostatin molecule given part. It is known that Ser has the strongly expressed tendency to take part in formation of β -structures because of electrostatic interactions between its side and main chains. The hydrogen bond between OH group of side chain and NH group of main one of serine the length of which varies in very narrow interval of 2,48÷2,51Å values forms in all calculated fragment conformations. Thus, the tetrapeptide fragments densely packed in space and mainly stabilized by non-valence interactions is presented in following calculations by shape conformations *eef*, *fee* and *eff*.

The number of calculated conformations on Phe6-Gly7-Leu8 tripeptide fragment belonging to 4 shapes and 16 forms of peptide chain is 324. The effective inter-residue interactions between Phe6 and Leu8 form in low-energy fragment conformations because of glycine residues playing the role of hinge in fragment structure. That's why the states with unfolded and semi-folded form of main chain realize with equal probability. This fact is affirmed by both the minimization results and analysis of contributions in fragment low-energy conformation states. The hydrogen bond between atoms of main chain of Phe6 and Leu8 residues the length of which varies in dependence on conformation state of main chain from 2,03 up to 2,07Å forms in fragment global conformation.

Table 1. Energy distribution of allatostatin conformations Dippu-AST5

№	Shape	Relative energy interval, kcal/mol						Conformation percentage (%)
		0÷1	1÷2	2÷3	3÷4	4÷5	>5	
1	<i>feeeefef</i>	1	6	3	7	6	26	28.1
2	<i>feeefee</i>	-	1	-	2	1	22	15.3
3	<i>feeefff</i>	-	-	-	3	4	16	13.2
4	<i>feeffff</i>	-	-	1	-	3	17	12.7
5	<i>feeeffe</i>	-	-	1	-	1	16	10.4
6	<i>fffefff</i>	-	-	-	1	-	10	6.2
7	<i>eeefefef</i>	-	1	2	1	-	2	3.4
8	<i>effeffff</i>	-	-	-	-	1	4	2.8
9	<i>eeefffff</i>	-	-	1	1	-	2	2.3
10	<i>eefeeefee</i>	-	-	-	-	1	3	2.3
11	<i>eeeeffe</i>	-	-	-	-	1	2	1.7
12	<i>fefeeefee</i>	-	-	1	1	-	1	1.6

Table 2. Energy parameters of low-energy conformations of allatostatin Dippu-AST5

№	Shape	Residue conformation								Energy contributions, kcal/mol				
		Asp	Arg	Leu	Tyr	Ser	Phe	Gly	Leu	E _{нев}	E _{эл}	E _{торс}	E _{полн}	E _{отн}
1	<i>feeeefef</i>	R ₁	B ₃	B ₃	B ₃	R ₁	R ₁	P	R ₃	-44,3	3,0	4,3	-36,9	0,0
2	<i>eeefefef</i>	R ₁	L ₃	B ₃	B ₃	R ₁	R ₁	P	R ₃	-44,9	4,5	5,1	-35,4	1,6
3	<i>feeefee</i>	R ₁	B ₃	B ₃	B ₃	R ₁	R ₁	P	L ₃	-42,4	2,3	4,9	-35,2	1,8
4	<i>feeeffe</i>	R ₁	B ₁	B ₃	B ₃	R ₁	R ₁	B	B ₃	-42,9	3,1	4,9	-34,9	2,1
5	<i>fefeeefee</i>	R ₁	B ₁	R ₂	B ₃	B ₂	B ₃	B	R ₃	-41,7	2,8	4,2	-34,6	2,4
6	<i>eeefffff</i>	R ₁	L ₃	B ₃	R ₃	R ₁	B ₃	P	R ₃	-42,4	3,9	4,1	-34,3	2,6
7	<i>feefffff</i>	B ₂	L ₃	B ₃	B ₃	R ₂	B ₃	P	R ₃	-40,0	2,5	3,8	-33,7	3,3
8	<i>fffefff</i>	R ₁	R ₃	R ₃	B ₃	R ₁	B ₃	P	R ₃	-40,0	3,2	3,4	-33,4	3,5
9	<i>feefffff</i>	R ₁	B ₁	B ₃	R ₃	R ₁	B ₃	P	R ₃	-40,1	2,6	5,8	-32,8	4,1
10	<i>eeefffff</i>	R ₁	L ₃	B ₃	B ₃	R ₂	B ₃	P	R ₃	-40,3	4,0	3,9	-32,4	4,6
11	<i>effeffff</i>	B ₁	R ₃	R ₃	B ₃	R ₁	B ₃	P	R ₃	-40,9	5,3	2,6	-32,2	4,8
12	<i>eefeeefee</i>	R ₁	L ₃	R ₂	B ₃	B ₁	B ₃	P	R ₃	-41,4	3,8	5,8	-31,8	5,1

Table 3. Energy contributions (kcal/mol) of interresidue interactions and distances between C^α-atoms of peptide chain in low-energy conformations of allatostatin Dippu-AST5

Amino-acid residues	Shape conformation <i>feeeef</i> with E _{rel} = 0,0 kcal/mol		Shape conformation <i>eeeeef</i> with E _{rel} = 1,6 kcal/mol	
	Distance between C ^α atoms (Å)	$\sum_{i,j}^8 E_{i,j}$	Distance between C ^α atoms (Å)	$\sum_{i,j}^8 E_{i,j}$
Asp1-Arg2	3.8	-7.5	3.8	-5.1
Arg2-Leu3	3.8	-1.6	3.8	-1.6
Leu3-Tyr4	3.8	-2.1	3.8	-2.1
Tyr4-Ser5	3.8	-1.9	3.8	-1.9
Ser5-Phe6	3.8	-2.2	3.8	-2.3
Phe6-Gly7	3.8	0.8	3.8	-0.8
Gly7-Leu8	3.8	-1.5	3.8	-1.5
Asp1-Leu3	6.4	-0.7	5.6	-4.8
Arg2-Tyr4	6.0	-3.3	5.9	-2.8
Leu3-Ser5	7.2	-0.2	7.2	-0.2
Tyr4-Phe6	5.4	-5.0	5.4	-5.1
Ser5-Gly7	5.0	-1.0	5.0	-1.0
Phe6-Leu8	5.7	-3.3	5.7	-3.3
Asp1-Tyr4	9.5	0.5	8.9	0.5
Arg2-Ser5	9.3	-0.1	9.3	-0.1
Leu3-Phe6	8.7	-0.1	8.6	-0.1
Tyr4-Gly7	4.3	-2.5	4.2	-2.6
Ser5-Leu8	8.4	-0.0	8.3	-0.0
Asp1-Ser5	12.9	-0.1	12.4	0.1
Arg2-Phe6	9.3	-0.3	9.2	-0.2
Leu3-Gly7	6.1	-0.2	5.9	-0.2
Tyr4-Leu8	7.4	-0.2	7.3	-0.2
Asp1-Phe6	13.0	0.1	12.9	0.1
Arg2-Gly7	6.1	-1.3	6.0	-1.1
Leu3-Leu8	8.6	-0.0	8.4	0.0
Asp1-Gly7	9.5	-0.1	9.5	-0.1
Arg2-Leu8	6.8	-3.3	6.6	-2.3
Asp1-Leu8	9.8	-0.0	10.0	0.1

Table 4. The dihedral angles of main and side chains of amino-acid residues in low-energy conformations of allatostatin Dippu-AST5

Amino-acid residue	Dihedral angles, grad		
Asp1	$\varphi = -89, \psi = -44, \omega = 178,$ $\chi_1 = 54, \chi_2 = 105$	$\varphi = -73, \psi = -43, \omega = 178,$ $\chi_1 = 61, \chi_2 = 112$	$\varphi = -89, \psi = -44, \omega = 180,$ $\chi_1 = 54, \chi_2 = 105$
Arg2	$\varphi = -134, \psi = 97, \omega = 179,$ $\chi_1 = -67, \chi_2 = 174, \chi_3 = 161$	$\varphi = 53, \psi = 57, \omega = 175,$ $\chi_1 = 57, \chi_2 = 179, \chi_3 = 181$	$\varphi = -133, \psi = 98, \omega = 183,$ $\chi_1 = -67, \chi_2 = 174, \chi_3 = 182$
Leu3	$\varphi = -99, \psi = 94, \omega = 183,$ $\chi_1 = 54, \chi_2 = 177, \chi_3 = 182$	$\varphi = -100, \psi = 94, \omega = 183,$ $\chi_1 = -56, \chi_2 = 174, \chi_3 = 187$	$\varphi = -99, \psi = 96, \omega = 182,$ $\chi_1 = -54, \chi_2 = 177, \chi_3 = 187$
Tyr4	$\varphi = -150, \psi = 165, \omega = 177,$ $\chi_1 = -67, \chi_2 = 95, \chi_3 = 180$	$\varphi = -148, \psi = 165, \omega = 178,$ $\chi_1 = -65, \chi_2 = 96, \chi_3 = 179$	$\varphi = -148, \psi = 164, \omega = 178,$ $\chi_1 = -61, \chi_2 = 95, \chi_3 = 180$
Ser5	$\varphi = -71, \psi = -52, \omega = 171,$ $\chi_1 = 56, \chi_2 = 177$	$\varphi = -69, \psi = -52, \omega = 171,$ $\chi_1 = 57, \chi_2 = 179$	$\varphi = -71, \psi = -53, \omega = 170,$ $\chi_1 = 57, \chi_2 = 180$
Phe6	$\varphi = -60, \psi = -29, \omega = 178,$ $\chi_1 = 62, \chi_2 = 81$	$\varphi = -60, \psi = -29, \omega = 178,$ $\chi_1 = 62, \chi_2 = 81$	$\varphi = -61, \psi = -35, \omega = 179,$ $\chi_1 = 57, \chi_2 = 80$
Gly7	$\varphi = 80, \psi = -77, \omega = 182$	$\varphi = 80, \psi = -77, \omega = 182$	$\varphi = 72, \psi = -89, \omega = 181$
Leu8	$\varphi = -104, \psi = -60, \omega = 179,$ $\chi_1 = 53, \chi_2 = 176, \chi_3 = 186$	$\varphi = -104, \psi = -60, \omega = 179,$ $\chi_1 = -53, \chi_2 = 176, \chi_3 = 186$	$\varphi = 50, \psi = 59, \omega = 180,$ $\chi_1 = -58, \chi_2 = 174, \chi_3 = 186$
E _{rel}	0.0 kcal/mol	1.6 kcal/mol	1.8 kcal/mol

The general number of 458 initial variants written for minimization procedure of whole molecule conformation energy is equal to 90 forms and 41 shapes of peptide chain. They are combinations of low-energy conformation states of Arg1-Leu3, Leu3-Phe6, Phe6-Leu8 fragments and their overlapping parts the relative energy of which doesn't exceed 5kcal/mol. The conformation analysis of sequentially expansion and overlapping fragments of Dippu-AST5 allatostatin molecule reveals the significant succession of results with length increase of considered peptide chain (table 1). The low-energy conformations of Dippu-AST5 allatostatin molecule are found in the result of energy minimization of written structural variants (table 2).

The conformations of octapeptide 12 structural types are included in relative energy interval 0÷10 kcal/mol. As a whole, 53% of calculated structures have the unfolded form of Arg2-Tyr4 section and differ only by conformation states of C-end fragment Ser5-Leu8 (i.e. NH₂). The distances between C^α-atoms of peptide chain

are given in table 3; the values of dihedral angles in molecule conformation state with global minimum of intramolecular conformation energy are given in table 4.

β-turn of peptide chain that evidences the distance between C^α-atoms of Tyr4 and Gly7 residues (4,3 Å; table 3) and hydrogen bonds between main chain atoms Tyr4 and Gly7 forms in molecule global conformation.

CONCLUSION

Generalizing the investigation results one can suppose that Dippu-AST5 allatostatin molecule can realize the series of low-energy conformation states differing mainly by conformation states of C-end fragment. The obtained results can serve as the base for purposeful modification of Dippu-AST5 allatostatin with the aim of analogue formation of more selective and prolonged action.

-
- | | |
|---|---|
| <p>[1] G.E. Pratt, D.E. Farnsworth, N.R. Siegel, K.F. Fok, R. Feyereisen. "Identification of an Allatostatin from Adult <i>Diploptera Punctata</i>" <i>Biochem. Biophys. Res. Commun.</i>, 1990, v.29, Iss.163(3), p.1243-1247.</p> <p>[2] B. Stay, S. Fairbairn, C.G. Yu. "Role of Allatostatins in the Regulation of Juvenile Hormone Synthesis" <i>Arch. Insect. Biochem. Physiol.</i>, 1996, v.32, No.3-4, p.287-297.</p> <p>[3] A.P. Woodhead, B. Stay, S.L. Seidel, M.A. Khan, S.S. Tobe. "Primary Structure of Four Allatostatins: Neuropeptide Inhibitors of Juvenile Hormone Synthesis" <i>Proc. Natl. Acad. Sci. USA</i>, 1989, v.85, No.15, p.5997-6001.</p> <p>[4] A.P. Woodhead, M.A. Khan, B. Stay, S.S. Tobe. "Two New Allatostatins from the Brains of <i>Diploptera Punctata</i>" <i>Insect. Biochem. Mol. Biol.</i>, 1994, v.24, No.3, p.257-263.</p> | <p>[5] E.M. Popov. "Quantitative Approach to Conformations of Proteins" // <i>Int. J. Quantum Chem.</i>, 1979, 16, p.707-737.</p> <p>[6] E.M. Popov. <i>Strukturnaya organizatsiya belkov</i>. M.: Nauka, 1989, 352s. (In Russian).</p> <p>[7] I.S. Maksumov, L.I. Ismailova, N.M. Godjaev. <i>Jurnal strukturnoy khimii</i>, 1983, t.24, No4, s.147-148. (In Russian).</p> <p>[8] F.A. Momany, R.F. McGuire, A.W. Burgess, H.A. Scheraga. "Energy Parameters in Polypeptides: Geometric Parameters, Partial Atomic Charges, Nonbonded Interaction for Naturally Occurring Amino Acid" <i>Phys. Chem.</i>, 1975, v.79, p.2361-2381.</p> <p>[9] IUPAC-IUB Commission on Biochemical Nomenclature Abbreviations and Symbols for Description of Conformation of Polypeptide Chains <i>Pure Applied Chem.</i>, 1974, v.40, p.291-308.</p> |
|---|---|

Received: 02.05.2018

INFLUENCE OF FULLERENES ON DIELECTRIC AND CONDUCTIVITY PROPERTIES OF LIQUID CRYSTAL MBBA

T.D. IBRAGIMOV, A.R. IMAMALIYEV, G.F. GANIZADE

Institute of Physics of Azerbaijan National Academy of Sciences,

H.Javid av.131, Baku, AZ1143, Azerbaijan

E-mail : tdibragimov@mail.ru

Influence of fullerenes C^{60} on dielectric and conductivity properties of liquid crystal MBBA has been investigated. It has been revealed that dielectric permittivity, dielectric losses and conductivity decrease in the frequency range of 20 Hz-1MHz at addition of fullerenes in liquid crystal. The activation energy has been defined from the temperature dependence of conductivity for both the pure liquid crystal and the colloid. It is established that the additive of fullerenes reduces the activation energy in both nematic and isotropic phases. Experimental results are explained by reduction of an order parameter and suppression of ionic conductivity at presence of fullerenes.

Key words: liquid crystal, MBBA, fullerenes, dielectric permittivity, electric conductivity

PACS: 64.70.mj; 64.70.pv; 78.15.e; 82.70.d.

1. INTRODUCTION

More recently, an alternative direction of physics and technology of liquid crystals (LC) has been the creation of hybrid liquid crystal systems and their application in various photonic devices. At this case a special role plays liquid crystal colloids. Herewith, not only properties of the liquid crystal are improved, but there are novel effects. Even at enough large sizes of particles the effect of an operated filtration and selective modulation of light [1-13] is observed. At the particle sizes of 100-600 nm, the electro-optical properties of liquid crystal are improved [14-32], and also generation of the second optical harmonic is observed in ferroelectric liquid crystal colloids [33]. Logically, to assume that there can be new effects when the particles sizes are very small. In particular, such particles may be fullerenes which are nanoparticles and have spherical form.

In the present work the results of investigation of influence of fullerenes on dielectric and conductive properties of nematic liquid crystal 4-methoxybenzilidene – 4' – butylaniline (MBBA) are presented.

2. EXPERIMENTAL

We used the nematic liquid crystal 4-methoxybenzilidene – 4' – butylaniline (MBBA) (NIOPIK, Russia) as a matrix having negative anisotropy of dielectric permittivity. The fullerenes C^{60} (U.S. Research Nanomaterials, Inc.) was added into the liquid crystal with 0.5 wt.% and was shaken in a vortex mixer for 1 hour, followed by sonication for 4 hours.

The cell had a sandwich structure and consisted of two plane-parallel glass plates whose inner surfaces were coated with thin transparent and conductive indium-tin-oxide (ITO) layer. The thin polyamide film rubbed in one direction was used for the planar orientation of LC molecules while a small amount of lecithin was added in the colloid and the pure LC for the homeotropic configuration. The cell thickness was fixed with calibrated 50 μ m polymer spacers for measurements. Both the colloid and the pure LC were injected into the empty cell by capillary action at the isotropic state. The filled cell

was kept in the special heater in which the copper-constantan thermocouple was used for temperature measurements. Accuracy of temperature determination was 0.1°C.

Dielectric and conductivity measurements were carried out by the Precision LCR Meter 1920 (IET Labs. Inc., USA) in the frequency range of 20 Hz – 1 MHz and at temperatures between 18°C – 60°C.

3. RESULTS

Observation under the polarization microscope has shown that the presence of fullerenes in MBBA shifts the clearing point from 42.2°C to 41.6°C. It is necessary to notice that the clearing temperature increases and reaches 47 °C at keeping of the pure LC in vacuum for 6 days.

Fig. 1 and Fig. 2 show frequency dependences of real ϵ' and imaginary ϵ'' parts of dielectric permittivity in both the pure LC and the corresponding colloid in homeotropic and planar configurations, accordingly, at temperature 23°C. Apparently, the longitudinal component $\epsilon_{||}'$ of dielectric permittivity of the pure LC varies a little up to 150 kHz and it is equal to 4.72 at frequency of 10 kHz while it makes 4.12 in the colloid. The transverse component ϵ_{\perp}' of dielectric permittivity in the pure LC is equal 5.22 at 10 kHz and remains almost invariable up to the highest frequencies while it makes 5.11 in the colloid at the same frequency. Namely, the real part of dielectric permittivity decreases in both cases at additive of fullerenes. Hereat, the parallel component decreases more than perpendicular component. The additive of particles also reduces an imaginary part of dielectric permittivity in both configurations.

Temperature dependence of parallel and perpendicular components of dielectric permittivity of both the pure MBBA and the colloid is resulted in Fig.3. As one can see, longitudinal component of dielectric permittivity of the pure LC increases from 4.72 (23°C) to 5.07 (41°C) while the transverse component changes from 5.22 to 5.07 at the same temperatures. As increasing temperature it decreases in the isotropic phase and reaches 4.99 at 49°C. Longitudinal component of dielectric permittivity

of the colloid decreases from 4.12 (23°C) to 4.02 (41°C) then it increases up to 4.06 (49°C) in the isotropic phase. The transverse component decreases from 5.11 at 23°C

to 4.06 near to transition in the isotropic state, then dielectric permittivity decreases and reaches 3.97 at 49°C.

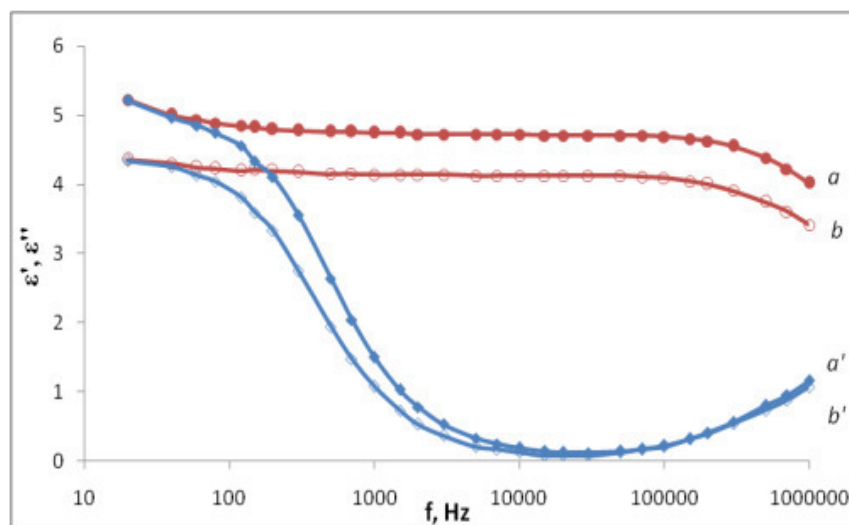


Fig.1. Frequency dependence of longitudinal components of dielectric permittivity and losses of the pure LC and the colloid: (a) ϵ' of LC; (b) ϵ' of the colloid; (a') ϵ'' of LC; (b') ϵ'' of the colloid.

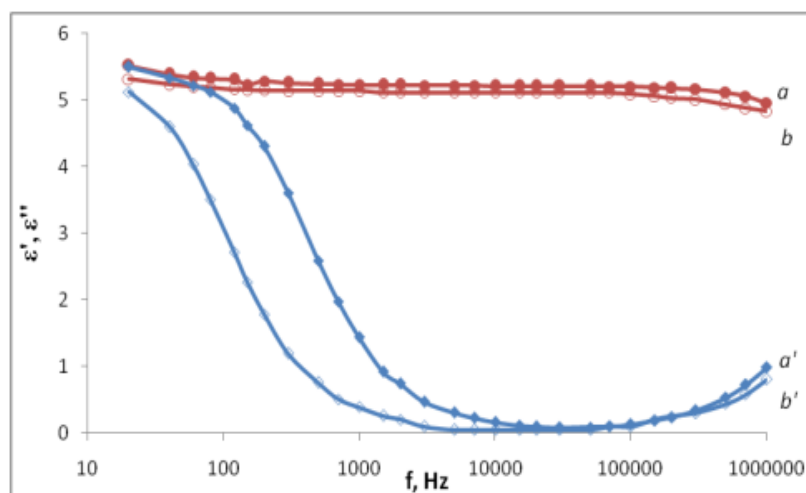


Fig.2. Frequency dependence of transverse components of dielectric permittivity and losses of the pure LC and the colloid: (a) ϵ' of LC; (b) ϵ' of the colloid; (a') ϵ'' of LC; (b') ϵ'' of the colloid.

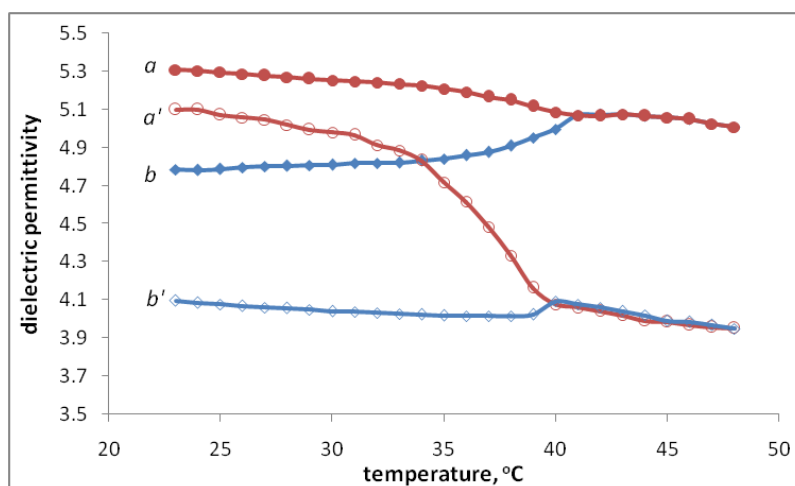


Fig.3. Temperature dependence of dielectric permittivity components of the pure LC and the colloid: (a) ϵ'_{\perp} of LC; (b) ϵ'_{\parallel} of LC; (a') ϵ'_{\perp} of the colloid; (b') ϵ'_{\parallel} of the colloid.

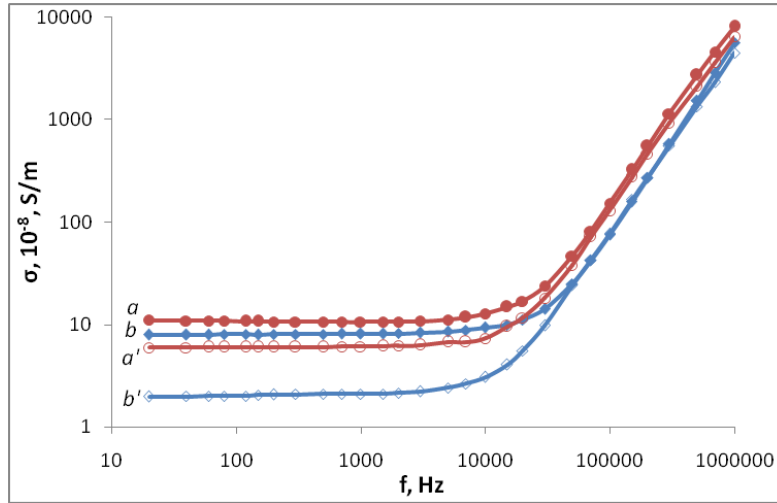


Fig.4. Frequency dependence of components of electric conductivity of the pure LC and the colloid: (a) $\sigma_{||}$ of LC; (b) σ_{\perp} of LC; (a') $\sigma_{||}$ of the colloid; (b') σ_{\perp} of the colloid.

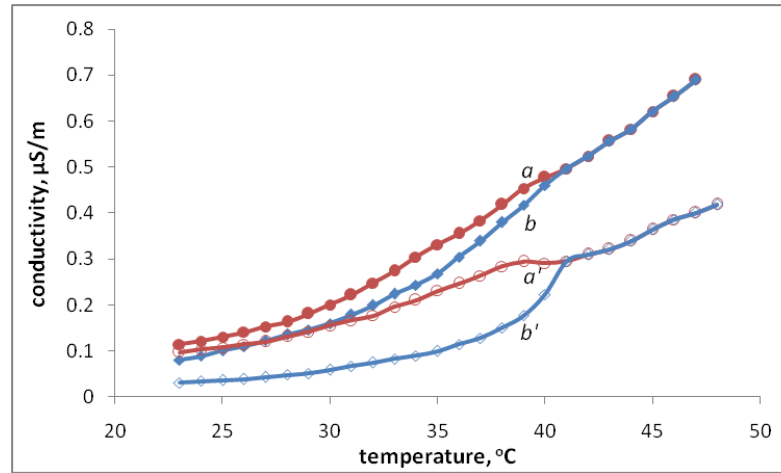


Fig.5. Temperature dependence of electric conductivity components of the pure LC and the colloid: (a) $\sigma_{||}$ of LC; (b) σ_{\perp} of LC; (a') $\sigma_{||}$ of the colloid; (b') σ_{\perp} of the colloid.

The frequency dependences of conductivity of both the pure LC and the colloid at temperature 23°C are presented in Fig.4. One can see, parallel component of the pure MBBA conductivity varies a little up to 10 kHz and equal to $1.1 \cdot 10^{-7}$ S/m, then it rises drastically and makes $6.5 \cdot 10^{-5}$ S/m at 1 MHz. At the additive of fullerenes conductivity remains unchanged and equal to $6.0 \cdot 10^{-8}$ S/m then it increases and also reaches $6.5 \cdot 10^{-5}$ S/m at 1 MHz. The transverse component makes $8.0 \cdot 10^{-8}$ S/m at low frequencies then also sharply increases after 10 kHz and reaches $4.5 \cdot 10^{-5}$ S/m at 1 MHz. The frequency dependence of conductivity has similar character at additive of fullerenes. But conductivity equals to $2.0 \cdot 10^{-8}$ S/m at low frequencies and it has the same value as well as for the pure LC. Therefore, values of conductivity of the colloid lower than for MBBA at low frequencies while it coincide for certain directions concerning the director. In addition, conductivity along the director is above than across.

An increase in temperature results to increasing of conductivity in both pure MBBA and the colloid (Fig.5). The parallel component of conductivity of MBBA rises

from $1.3 \cdot 10^{-7}$ S/m (23°C) to $4.8 \cdot 10^{-7}$ S/m near the clearing point on the frequency of 10 kHz. The transverse component of conductivity varies from $1.1 \cdot 10^{-7}$ S/m to $4.8 \cdot 10^{-7}$ S/m at the same frequencies and temperatures. Then it increases up to $7.7 \cdot 10^{-7}$ S/m at 49°C in the isotropic phase. The parallel component of conductivity of the colloid increases from $9.5 \cdot 10^{-8}$ S/m (23°C) to $2.9 \cdot 10^{-7}$ S/m (40°C) while the transverse component does from $3.0 \cdot 10^{-8}$ S/m to $2.8 \cdot 10^{-7}$ S/m (40°C). In the isotropic state, it increases up to $4.0 \cdot 10^{-7}$ S/m at 49°C.

4. DISCUSSION

According to [34], particles do not disturb the director field of LC, if the anchoring parameter $\zeta = WR/K$ is much smaller than 1, where W is the anchoring energy of LC molecules with particle surfaces, $2R$ is a particle size and K is the LC average elastic constant. The value of anchoring energy is within $10^{-5} - 10^{-6}$ J/m², the elastic constant of LC has an order of 10^{-12} N, and the particles (fullerenes) have sizes of 0.6-0.7 nm. Simple calculations

show that ζ has an order within 10^{-2} - 10^{-3} , in other words, such colloid has to behave as a pure liquid crystal but with modified properties.

According to [35] embedded particles abate interaction between LC molecules. At this case, for the spherical form and low concentration of isotropic particles, the clearing temperature T_c of a colloid is defined by the expression:

$$T_c = (1 - f) T_0$$

where f is the volume fraction of particles, T_0 is the clearing temperature of the pure LC. The fullerene particles are isotropic and have spherical form. Their volume fraction equals to 0.003. The simple calculations give the values of 42.0°C which are higher than the experimental data but they agree qualitatively with them.

Experiments have shown that the real part both parallel and perpendicular components of dielectric permittivity at addition of fullerenes decreases. In this case the longitudinal component $\epsilon_{||}$ decreases by 0.58 while the transverse component ϵ_{\perp} by 0.11. According to the Mayer-Meyer theory for dielectric permittivity of liquid crystal, $\epsilon_{||}$ and ϵ_{\perp} depend on number N of LC molecules in single volume, and also on the order parameter S . Inclusion of fullerenes between LC molecules reduces their number per unit volume but negligible degree. The order parameter S also decreases as it depends on an angle between the directions of long axes of individual LC molecules with the general direction field of the nematic phase. Imbedded nanoparticles increase corresponding angles and, accordingly, reduce the order parameters. Thus, N and S act similarly, namely, both parameters reduce the longitudinal components $\epsilon_{||}$ of dielectric permittivity. While a decrease in N and S have diverse effect on $\epsilon_{||}$. As a result, the value of the longitudinal component decreases in a greater degree than the value of its transverse component of dielectric permittivity.

Dielectric anisotropy $\Delta\epsilon$ of the pure LC at temperature 23°C and middle frequencies equals -0.50 while it does -0.99 in the colloid. That is the dielectric anisotropy increases almost in 2 times, namely, 1.98 times

at addition of fullerenes. It is obvious, the similar increase in dielectric anisotropy will strongly reduce threshold voltages of the Freedericksz effect and formation of Williams' domens.

As it has been noted earlier, an inclusion of fullerenes into the liquid crystalline matrix reduces its conductivity. It proves to be true also reduction of dielectric losses. It is obvious, that the reason of reduction of conductivity consists that fullerenes suppress the ionic conductivity in the LC. It, its turn, indicates on a decrease of critical frequency of disappearance of the Williams' domens.

Arrhenius law for conductivity is defined by following expression:

$$\sigma = Ae^{-\frac{E_a}{k_B T}}$$

where E_a is activation energy, k_B is the Boltzmann constant, T is absolute temperature, and A is the parameter connecting with properties of the medium. Using this expression it is possible to calculate the activation energy for pure LC and the colloid. The activation energy along the long axis of molecules of the pure MBBA is equal to 0.87 eV while it does 0.58 eV for the colloid. The activation energy perpendicular to the long axis of molecules makes 1.1 eV for the pure LC while it is equal to 0.71 eV for the colloid. The additive of fullerenes also decreases the activation energy in isotropic phase from 0.54 eV to 0.35 eV. Apparently, a decrease of the activation energy connects with decreasing of ionic conductivity.

5. CONCLUSIONS

It is shown that the additive of fullerenes C^{60} into the liquid crystal MBBA decreases dielectric permittivity and losses, electric conductivity, and also the activation energy of both nematic and isotropic phases of liquid crystal. Experimental results are explained by reduction of the order parameter and suppression of ionic conductivity at presence of fullerenes.

-
- [1] *T.D. Ibragimov*. Christiansen effect in an Al_2O_3 particles-liquid crystal system. // *Journal of Applied Spectroscopy*, 2009, v.76, No 5, pp.752-755
 - [2] *T.D. Ibragimov, G.M. Bayramov, A.R. Imamaliyev*. Tunable filters on the base of the small particles-liquid crystal system / *Book of Abstracts of 13 Topical Meeting on the Optics of Liquid Crystals (OLC2009)*: Erice, Italy, 2009, p.26
 - [3] *T.D. Ibragimov, G.M. Bayramov, A.R. Imamaliyev*. Christiansen effect in the small particles-liquid crystal system / *Book of Abstracts of Progress in Electromagnetics Research Symposium (PIERS)*: Moscow, Russia, 2009, p.877
 - [4] *T.D. Ibragimov, G.M. Bayramov, A.R. Imamaliyev*. Tunable infrared filters on the base of the small particles-liquid crystal / *Book of Abstracts of 10 International Conference on Advanced Laser Technologies*. (ALT 09): Antalya, Turkey, 2009, p. 206
 - [5] *T.D. Ibragimov, E.A. Allakhverdiyev, G.M. Bayramov, A.R. Imamaliyev*. Investigation of Christiansen effect in the small particles of aluminum oxide-liquid crystalline system // *Azerbaijan Journal of Physics*, 2011, v.17, No 1, pp.61-69
 - [6] *T.D. Ibragimov, E.A. Allakhverdiyev, G.M. Bayramov, A.R. Imamaliyev*. Selective modulation of infrared radiation by an Al_2O_3 particles – liquid crystal system // *Journal of Applied Spectroscopy*, 2011, v.78, p.445-449.
 - [7] *T.D. Ibragimov, G.M. Bayramov*. Novel type of tunable infrared filters based on the Al_2O_3 particles – liquid crystal system // *Infrared Physics and Technology*, 2012, v.55, No 1, pp.56-59
 - [8] *T.D. Ibragimov, N.D. Ismaylov, E.A. Allakhverdiyev*.

- Upravlyaemiy jidkokristallicheskiy filtr. Evraziyskiy Patent № 016161, 28 fevral 2012 (In Russian).
- [9] T.D. Ibragimov, G.M. Bayramov. Application of dual-frequency liquid crystal for tunable selective filtration of infrared radiation // Journal for Light and Electron Optics (Optik), 2013, v.124, pp.6666-6668.
- [10] T.D. Ibragimov, E.A. Allakhverdiev, G.M. Bayramov. Transactions of ANAS, 2013, v. 33, No 2, pp.35-43.
- [11] T.D. Ibragimov, A.R. Imamaliyev, A.K. Mammadov, G.M. Bayramov. About possibility of using a dual-frequency liquid crystal for selective modulation of radiation // Azerbaijan Journal of Physics, 2014, No 1, pp.7-9.
- [12] T.D. Ibragimov, G.M. Bayramov, A.R. Imamaliyev. Filtration and modulation of infrared radiation by the small particles: dual-frequency liquid crystal system, Technical Summaries of SPIE Photonic West: Emerging Liquid Crystal Technologies X (9384-27): Sun Diego, USA, 2015, p.371.
- [13] T.D. Ibragimov, E.A. Alahverdiyev. Tunable dispersion filters based on liquid crystalline systems. Book of Abstracts of 5 International School and Conference on Photonics: Belgrade, Serbia, 2015, p.124-125
- [14] T.D. Ibragimov, G.M. Bayramov, A.R. Imamaliyev. Influence of small particles on Clark-Lagerwall effect in the ferroelectric liquid crystal. Abstract of the European Conference on Liquid Crystals: Maribor, Slovenia, 2011, p. P3-19
- [15] T.D. Ibragimov, G.M. Bayramov, A.R. Imamaliyev. Investigation of Clark-Lagerwall effect in the small particles-liquid crystalline system. Azerbaijan Journal of Physics, 2011, v.17, No 2, p.42-47.
- [16] T.D. Ibragimov, G.M. Bayramov, A.R. Imamaliyev. Clark-Lagerwall effect in the small particles-ferroelectric liquid crystal system. International Journal for Light and Electron Optics (Optik), 2013, v. 124, pp.343-346
- [17] T.D. Ibragimov, G.M. Bayramov. Influence of small particles on Carr– Helfrich electrohydrodynamic instability in the liquid crystal // International Journal for Light and Electron Optics (Optik), 2013, v. 124, pp.3004-3006
- [18] T.D. Ibragimov, Ch.O. Qacar, Sh.Yu. Samedov, G.M. Bayramov. Influence of small particles on electrohydrodynamic instability in the nematic liquid crystal // Azerbaijan Journal of Physics, 2013, v.19, No 1, pp. 42-45
- [19] T.D. Ibragimov, G.M. Bayramov. Influence of small particles on electrooptic effects in liquid crystals / Abstracts of SPIE Organic Photonics + Electronics (8828-40): San Diego, USA, 2013, p.271
- [20] T.D. Ibragimov, A.K. Mamedov, G.M. Bayramov. Influence of small particles on electrohydrodynamic instability in the liquid crystal. Programme and Abstracts of 20th Conference on Liquid Crystals. (Chemistry, Physics and Applications): Mikolajki, Poland, 2013, p.PC-19
- [21] Ibragimov T.D., Bayramov G.M. Electrooptic effects in liquid-crystalline colloids. Book of Abstracts of 12th European conference on Liquid Crystals: Kallithea, Rhodes island, Greece, 2013, p.PL-46.
- [22] Ibragimov T.D., Bayramov G.M., Imamaliyev A.R. Influence of small BaTiO₃ particles on electro-optic properties of liquid crystal 5CB / Abstract Book of the 2nd Asian Conference on Liquid Crystals (12-5): Busan, Korea, 2015, p.129
- [23] Ибрагимов Т.Д., Имамалиев А.Р., Байрамов Г.М.. Влияние малых частиц титаната бария на электрооптические характеристики жидкого кристалла 5CB при слабом сцеплении // Transactions of ANAS, 2015, v. 35, No 2, pp. 23-29
- [24] Ibragimov T.D., Imamaliyev A.R., Bayramov G.M. Electro-optic characteristics of liquid crystalline mixture H37 doped by ferroelectric particles // Azerbaijan Journal of Physics, 2015, v.21, No 2, pp.27-31
- [25] Ibragimov T.D., Imamaliyev A.R., Bayramov G.M. Peculiarities of Electro-Optic Properties of the Ferroelectric Particles-Liquid Crystal Colloids / Book of Abstracts of 5th International Advances in Applied Physics and Materials Science Congress & Exhibition (APMAS2015): Fethiya, Turkey, 2015, p.404
- [26] Ibragimov T.D., Imamaliyev A.R., Bayramov G.M. Formation of local electric fields in the ferroelectric BaTiO₃ particles-liquid crystal colloids / Book of Abstracts of 15th International Conference on Ferroelectric Liquid Crystals: Challenges in polar self-assembling systems: Prague, Czech Republic, 2015, p.120
- [27] Ibragimov T.D., Imamaliyev A.R., Allahverdiyev E.A., Azizov S.T., Aliyev O.A., Bayramov G.M. Dielectric relaxation in the BaTiO₃ particles – liquid crystal colloids // Azerbaijan Journal of Physics, 2015, v.21, No 4, pp.31-33
- [28] Ibragimov T.D., Imamaliyev A.R., Bayramov G.M. Electro-optic parameters of ferroelectric particles-liquid crystal composites / Abstracts of 17th International Conference on Photonics: Amsterdam, The Netherlands, 2015, p.45438 (International Science Index, Physical and Mathematical Sciences, 2015, v.2, No 8)
- [29] Ibragimov T.D., Imamaliyev A.R., Bayramov G.M. Influence of barium titanate particles on electro-optic characteristics of liquid crystalline mixture H37 // International Journal for Light and Electron Optics (Optik), 2016, v.127, pp. 1217–1220
- [30] Ibragimov T.D., Imamaliyev A.R., Bayramov G.M. Electro-optic properties of the BaTiO₃-Liquid crystal 5CB colloid // International Journal for Light and Electron Optics (Optik), 2016, v.127, pp. 2278–2281
- [31] Ibragimov T.D., Imamaliyev A.R., Bayramov G.M. Formation of local electric fields in the ferroelectric BaTiO₃ particles-liquid crystal colloids // Ferroelectrics, 2016, v.495, No 1, pp. 60-68
- [32] Ibragimov T.D., Imamaliyev A.R., Bayramov G.M. Peculiarities of electro-optic properties of the ferroelectric particles-liquid crystal colloids // AIP Conference Proceedings, 2016, v.1727, pp.020011-1-8
- [33] Ибрагимов Т.Д., Салманов В.М., Гусейнов А.Г., Мамедов Р.М. Излучательная рекомбинация в

жидкокристаллическом коллоиде 5CB+ BaTiO₃//
Transactions ANAS, 2018, No 2, 35-42

- [34] Liquid crystals beyond displays. Chemistry, physics, and applications / Edited by Li Q. New Jersey, Hoboken: John Wiley and Sons, Inc., 2012, 573 p.

- [35] Haragushi F., Inoue K., Toshima N. et al. Reduction of the threshold voltages of nematic liquid crystal electrooptical devices by doping inorganic nanoparticles // Japanese Journal Applied Physics, 2007, v. 46, pp. L796-L797

Received: 12.04.2018

THE FLUCTUATION CONDUCTIVITY IN $\text{Bi}_{1.7}\text{Pb}_{0.3}\text{Sr}_2\text{Ca}_2\text{Cu}_3\text{O}_y$

V.M. ALIYEV, R.I. SELIM-ZADE, V.I. EMINOVA, S.Z. DAMIROVA

v_aliev@bk.ru

*Institute of Physics of Azerbaijan National Academy of Sciences,**AZ 1143, Baku, H.Javid av.131*

The mechanism of formation of excess conductivity in cuprate HTSC $\text{Bi}_2\text{Sr}_2\text{CaCu}_2\text{O}_x$ and $\text{Bi}_{1.7}\text{Pb}_{0.3}\text{Sr}_2\text{Ca}_2\text{Cu}_3\text{O}_y$ was considered in the framework of the Ginzburg-Landau theory model, with the Varlamov and Livanov correction. The temperature transition T_0 from the 2D fluctuation region to the 3D region (the temperature of the 2D-3D crossover) was calculated. The values of the coherence length $\xi_c(0)$ along the axis c Cooper couples and their interplanar coupling constant (J) have been calculated.

Keywords: superconductivity, pseudogap, excess conductivity, coherence length, composition.

PACS: 74.25.Fy, 74.20.Mn, 74.72.+h, 74.25.+q, 74.25.Jb

INTRODUCTION

Although more than thirty years have passed since the discovery of bismuth-containing high-temperature superconducting materials, their synthesis is an unsolved problem. The main disadvantages of traditional production of HTSC materials methods of this homologous series are low speed, incomplete completion of the solid-phase reaction, and also the complexity of directional formation of the real structure of the final material, which determines its structure-sensitive properties [1,2]. To date, three superconducting phases with the general formula $\text{Bi}_2(\text{SrCa})_{n+1}\text{Cu}_n\text{O}_x$ ($n = 1, 2, 3$), abbreviated as Bi Sr Ca Cu, are found in the Bi-Sr-Ca-Cu-O system as 2201, 2212, 2223. The critical temperature T_c increases with increasing Ca and Cu content and reaches 10K-35K, 80K-90K and 100-110K for phases 2201, 2212 and 2223, respectively [1-4].

It is known that the HTSC ceramics on Bi-based are of great interest in connection with the existence in it of a phase with $T_c > 100$ K. However, the synthesis of this phase is a complex problem, since along with the $\text{Bi}_2\text{Sr}_2\text{Ca}_2\text{Cu}_3\text{O}_x$ phase, for which $T_k > 100\text{K}$, a $\text{Bi}_2\text{Sr}_2\text{CaCu}_2\text{O}_x$ phase with $T_c \approx 80\text{K}$ is formed, as well as non superconducting phases [1].

We note that $\text{Bi}_{1.7}\text{Pb}_{0.3}\text{Sr}_2\text{Ca}_2\text{Cu}_3\text{O}_y$ is a convenient object for studying the formation mechanism of excess conductivity in cuprate compounds. We note that the partial substitution of bismuth by lead in the composition $\text{Bi}_2\text{Sr}_2\text{Ca}_2\text{Cu}_3\text{O}_x$ leads to an increase in the volume fraction of 2223 in the polycrystal [5,6]. Also, the presence of lead in polycrystals $\text{Bi}_2\text{Sr}_2\text{Ca}_2\text{Cu}_3\text{O}_x$ (B1) and $\text{Bi}_{1.7}\text{Pb}_{0.3}\text{Sr}_2\text{Ca}_2\text{Cu}_3\text{O}_y$ (B2) promotes an increase in the ratio of $\text{Cu}^{3+} / \text{Cu}^{2+}$ and, correspondingly, an increase in the critical temperature T_c , as well as decrease in the specific resistivity. This means that such a substitution leads to an increase in the state density of charge carriers [7-10].

It is known that the longitudinal and transverse coherence lengths in HTSC materials are very small [1, 2]. Short coherence lengths lead to a rather small volume of coherence. As a result, thermodynamic fluctuations play an important role in these systems. The study of the fluctuation conductivity above T_c is directly related to the formation of coupled electrons and also it considers the mechanisms of their occurrence. The method of

fluctuation conductivity is an effective method of obtaining information about the behavior of a superconductor in the region of a phase transition. Substitution in HTSC leads to a change in the electronic system and, as a consequence, to a change in the microscopic parameters of the superconductor.

The aim of this work is to determine the effect of partial substitution of bismuth by lead in Bi-Sr-Ca-Cu-O on parameters of fluctuation conductivity.

EXPERIMENTAL RESULTS AND DISCUSSION

The procedure for obtaining $\text{Bi}_2\text{Sr}_2\text{Ca}_2\text{Cu}_3\text{O}_x$ (B1) and $\text{Bi}_{1.7}\text{Pb}_{0.3}\text{Sr}_2\text{Ca}_2\text{Cu}_3\text{O}_y$ (B2) compounds is described in our work [11]. The powdered oxides and carboxyls of Bi_2O_3 , PbO , SrCO_3 , CaCO_3 , and CuO of purity of 99.99% have been used in the synthesis of samples B1 and B2. The ratio of the initial components corresponded to the 2: 2: 2: 3 phase. The solid-phase reaction was carried out in two stages: first, at the temperature 1223K for 10 h, the intermediate products $\text{Sr}_2\text{Ca}_2\text{Cu}_3\text{O}_x$ and $\text{Pb}_{0.3}\text{Sr}_2\text{Ca}_2\text{Cu}_3\text{O}_y$ have been synthesized. The cooled mixture was triturated, the required amount of Bi_2O_3 was added to it and mixed well. Then the mixture was pressed into a tablet, sintering was carried out at 1123K for 48 hours, followed by quenching in air. Thus, $\text{Bi}_2\text{Sr}_2\text{Ca}_2\text{Cu}_2\text{O}_x$ polycrystals (containing up to (70-80)% phase 2212 with a mixture of 2202 and 2223 phases) and $\text{Bi}_{1.7}\text{Pb}_{0.3}\text{Sr}_2\text{Ca}_2\text{Cu}_3\text{O}_y$ (the content of the 2223 phase in the polycrystal was about 90%) were obtained.

The X-ray phase analysis was carried out for polycrystalline B1 and B2 samples [11]. On the basis of the radiograph, the percentage of 2212 and 2223 phases was calculated and the present additional was determined. The content of the 2212 phase in polycrystalline B1 was 70-80%, whereas the content of phase 2223 in polycrystalline B2 was already about 90%.

The temperature dependences of the resistivity of the B1 and B2 specimens are shown in Fig1. The critical temperatures of the SC transition T_c were determined from the maximum $d\rho/dT$, obtaining by differentiating the curve $\rho(T)$ fig.2.

As seen from Fig.1, partial substitution of Bi by Pb in the Bi-Sr-Ca-Cu-O system leads to an increase in the critical temperature from $T_{c1} = 90.5\text{K}$ (sample B1) to $T_{c2} = 100.09\text{K}$ (sample B2).

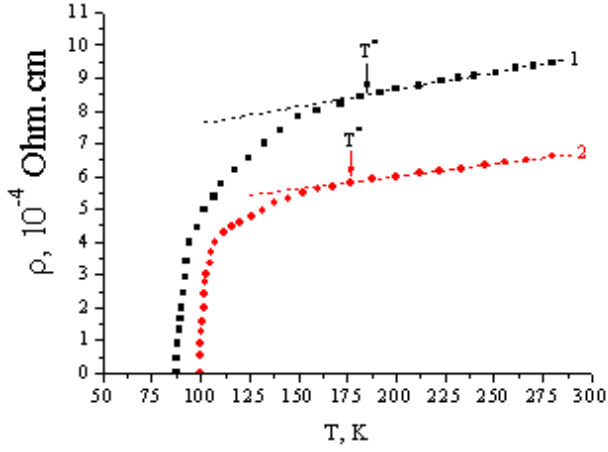


Fig.1. Temperature dependence of specific resistivity in B1 and B2, correspondingly 1 and 2.

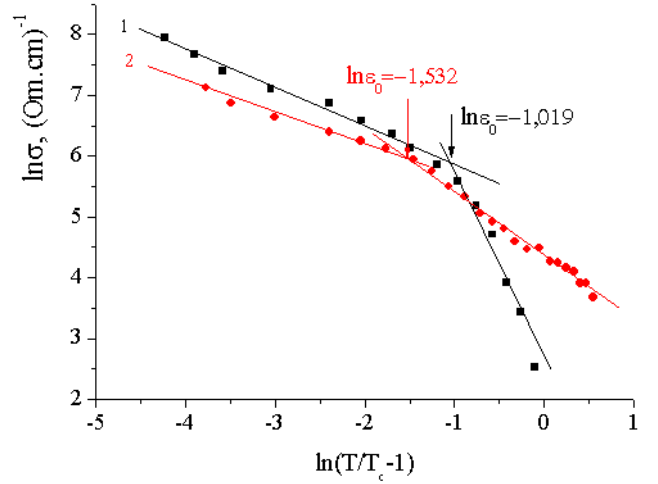


Fig.3. Dependence of excess conductivity logarithm from $\ln(T/T_c - 1)$ in composition B1 and B2, correspondingly 1 and 2.

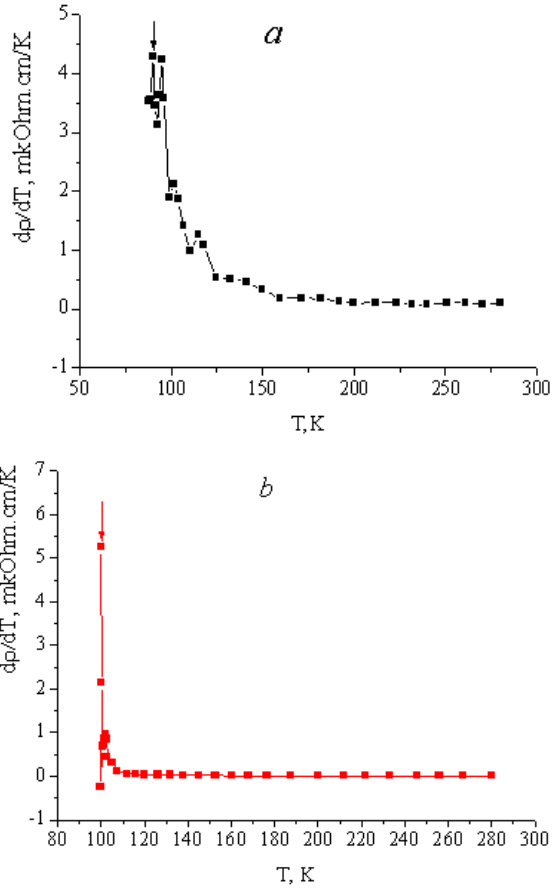


Fig.2. Temperature dependence of $d\rho/dT$ in the area of HS in composition B1 and B2, correspondingly a and b.

In this case, the resistivity ρ of the sample $\text{Bi}_{1.7}\text{Pb}_{0.3}\text{Sr}_2\text{Ca}_2\text{Cu}_3\text{O}_y$ in the normal phase decreases by almost 1.5 times in comparison with $\text{Bi}_2\text{Sr}_2\text{Ca}_2\text{Cu}_3\text{O}_x$.

It is known that there are two fluctuation contributions to the conductivity. A direct contribution, theoretically substantiated by Aslamazov and Larkin (AL) [12], arises as a result of spontaneous formation above T_c of Cooper couples created by fluctuations. The additional contribution introduced by Maki and Thompson (MT) [13, 14] to the development of AL theory is interpreted as the result of the interaction of already existing fluctuation couples with normal charge carriers and is determined by the processes of ancoupling in a particular sample. The contribution of the MT contribution depends on the lifetime of the fluctuation couples and it dominates in the region of two-dimensional 2D fluctuations in the case of weak ancoupling. The AL mechanism dominates in the three-dimensional 3D region of the phase transition near T_c . Thus, as the temperature approaches T_c , a change in the fluctuation mechanisms must be observed experimentally. In the layered structures, including HTSC, the AL contribution is usually determined by the Lawrence-Donijah (LD) model, which predicts a smooth dimensional crossover from 2D to 3D fluctuation behavior at $T \rightarrow T_c$.

In the framework of the Ginzburg-Landau theory, the fluctuation correction to conductivity in HTSC materials was calculated by Varlamov and Livanov [15]. According to this theory, the additional conductivity has the form.

$$\Delta\sigma = \left(\frac{e^2}{16\hbar d} \right) \left(\frac{T}{T_c} - 1 \right)^{-1} \left[1 + J \left(\frac{T}{T_c} - 1 \right)^{-1} \right]^{-1/2} \quad (1)$$

Where $J = (2\xi_c(0)/d)^2$ – the constant of interlayer coupling, d – distance between layers.

It can be seen from equation (1) that at high temperatures, $T \gg T_c$ (where $J \ll \varepsilon$; $\varepsilon = (T/T_c - 1)$), $\Delta\sigma$ is proportional to ε^{-1} (2D-conductivity), and when

approaching the transition temperature T_c (where $J \gg \varepsilon$), $\Delta\sigma$ varies to proportion $\varepsilon^{-1/2}$ (3D – conductivity).

The Figure 3 shows the dependence of the reduced electrical conductivity on temperature in the studied samples. This dependence shows a transition from 2D to 3D conductivity. The temperatures of the 2D-3D crossover (T_{cr}) of the studied samples are determined from the condition $\varepsilon=4\gamma$; where $\varepsilon=(T-T_c)/T_c$ and $\gamma=(\xi_c(0)/d)^2$, i.e.

$$T_{cr}=T_c\{1+4(\xi_c(0)/d)^2\} \quad (2)$$

For the bismuth system, $d(2212) = 15 \text{ \AA}$ and $d(2223) = 19 \text{ \AA}$ [16].

The interlayer coupling constant J ($0.377\text{-Bi}_2\text{Sr}_2\text{Ca}_2\text{Cu}_3\text{O}_x$ and $0.21274\text{-Bi}_{1.7}\text{Pb}_{0.3}\text{Sr}_2\text{Ca}_2\text{Cu}_3\text{O}_y$), the coherence length $\xi_c(0)$ ($4.606\text{ \AA-Bi}_2\text{Sr}_2\text{Ca}_2\text{Cu}_3\text{O}_x$, and $0.442\text{-Bi}_{1.7}\text{Pb}_{0.3}\text{Sr}_2\text{Ca}_2\text{Cu}_3\text{O}_y$) are also estimated.

As seen from these experimental data, the partial substitution of bismuth by lead in $\text{Bi}_2\text{Sr}_2\text{Ca}_2\text{Cu}_3\text{O}_x$ leads to an increase in the volume fraction of 2223 in the polycrystalline and also leads to a decrease in both the

constant interlayer coupling and the coherence length of Cooper couples.

CONCLUSION

The influence of the partial substitution of Bi by Pb on the mechanism of excess conductivity in the Bi–Sr–Ca–Cu–O system is studied. It was found that partial substitution of Bi for Pb leads to an increase in the critical temperatures of the sample $\text{Bi}_{1.7}\text{Pb}_{0.3}\text{Sr}_2\text{Ca}_2\text{Cu}_3\text{O}_y$ (B2) in comparison with $\text{Bi}_2\text{Sr}_2\text{Ca}_2\text{Cu}_3\text{O}_x$ (B1) ($T_c(\text{B2}) = 100.09 \text{ K}$ and $T_c(\text{B1}) = 90.5 \text{ K}$, respectively). Simultaneously, the resistivity ρ of $\text{Bi}_{1.7}\text{Pb}_{0.3}\text{Sr}_2\text{Ca}_2\text{Cu}_3\text{O}_y$ in the normal state decreases and is a factor of ≈ 1.5 smaller than that found for $\text{Bi}_2\text{Sr}_2\text{Ca}_2\text{Cu}_3\text{O}_x$.

The mechanism of formation of excess conductivity in cuprate HTSC $\text{Bi}_2\text{Sr}_2\text{Ca}_2\text{Cu}_3\text{O}_x$ and $\text{Bi}_{1.7}\text{Pb}_{0.3}\text{Sr}_2\text{Ca}_2\text{Cu}_3\text{O}_y$ was considered within the framework of the model in the framework of the Ginzburg-Landau theory, with the Varlamov and Livanov correction. The T_0 transition from the 2D fluctuation region to the 3D region (i.e., the temperature of the 2D-3D crossover) was calculated.

-
- | | |
|---|---|
| <p>[1] V.D. Gorobchenko, A.V. Irodova, M.V. Jarnikov, O.A. Lavrova, Q.V. Laskova, G. V.Pilyagin. SPChT, v.2, №7, pp. 55-60 (1989)</p> <p>[2] I.F. Kononyuk, V.V. Vashuk, L.V. Makhnach, Yu.G. Zonov. SPChT, v.2, №7, pp.77-81(1989)</p> <p>[3] J.B.Torrance, Y.Tokura, S.L.LaPlaca, T.C. Huang, R.J. Savoy, and A.I. Nazzal. Solid State Commun., v.66, №7, pp.703-706 (1988).</p> <p>[4] T.Kondo, Y. Hamaya, A.Palczewski, T.Takeuchi, J.S.Wen, G.Z.J.Xu, GendaGu, J.Schmalian and A.Kaminski, Nature physics, 1-9, (2010)</p> <p>[5] P. Upadhyay, S. Rao, K. Nagpal, R. Sharma. Mat. Res. Bull. v.27, №5, pp.109-116, (1992)</p> <p>[6] W. Lo, B.A. Glowacki. Cryogenics.v.32, pp.544-547, (1992)</p> <p>[7] A. Oota, A. Kiriigashi, Y. Sasaki, K. Ohba. Jpn. J. Appl. Phys. v.27, №12, pp.2289-2292, (1988)</p> <p>[8] W. Yugui, J. Xinping, W. Jinsong, W.Nanling, H.Guchang, Inter. J. Mod. Phys. B. v.3, №4, pp.595-601, (1989)</p> | <p>[9] G. Padam, R. Tripathi, M. Sharma, D.K. Suri, S.U.M. Rao, K.C. Nagpal, and B.K. Das, Sol. State Comm. v.80, №4, pp.271-275, (1991)</p> <p>[10] M. Awan, M. Maqsood, A. Maqsood, M. Arshad, S.A. Mirza, and S.A. Siddiqui, J. Mater. Sci. Lett. v.13, pp.1198-1200, (1994)</p> <p>[11] V.M. Aliyev, S.A. Ragimov, R.I. Selim-zade, S.Z. Damirova, B.A. Tahirov, Low Temperature Physics, v.43, №12, pp.1707-1714 (2017)</p> <p>[12] L.G.Aslamazov and A.L. Larkin, Phys. Lett., v.6, pp.238-239 (1968)</p> <p>[13] K.Maki, Prog.Theor. Phys., 39, 897-901 (1968)</p> <p>[14] R.S.Tompson, Phys.Rev.B1, v 327-332(1970)</p> <p>[15] A.A. Varlamov, D.V. Livanov, JETPh, v.98, pp.584-592 (1990)</p> <p>[16] P.Villier, R.A.Doyle, V.V.Griidin J. Phys. Condens. Matter, 1992, 4, p. 9401-9410</p> |
|---|---|

Received:25.04.2018

TEMPERATURE DEPENDENCE OF ELECTRICAL CHARACTERISTICS OF Ag/n-GaAs SCHOTTKY BARRIER DIODES

A.A. ASIMOV, A.M. KERIMOVA, Kh.N. AHMEDOVA, İ.A. NASİBOV

Institute of Physics of Azerbaijan NAS, AZ 1143,

H.Javid ave., 131, Baku, Azerbaijan

The electrical characteristics of Ag/ n-GaAs Schottky barrier diodes have been investigated. Measurements were carried out in the temperature range of 140-300 K. The I-V analysis based on thermionic emission (TE) theory has revealed an abnormal decrease of apparent barrier height and increase of ideality factor at low temperature region. Such behavior of barrier height (ϕ_b) and ideality factor (n) is attributed to barrier height inhomogeneities prevailing at the metal-semiconductor interface. The inhomogeneities are considered to have a Gaussian distribution with a mean barrier height of $\phi_b = 0,79$ eV and a standard deviation of $\sigma_{s0} = 0,12$ V at zero bias. Moreover, Richardson constant value obtained from modified Richardson plot, $\ln(I_0/T^2) - q^2\sigma_0^2/2(kT)^2$ versus $10^3/T$ was found to be $3,51 \text{ A/K}^2\text{cm}^2$ which is much closer to the theoretical value than that obtained from conventional Richardson plot.

Keywords: Schottky barrier diode, barrier height, ideality factor, Richardson constant.

PACS: 72.10-d, 73.40 GK

INTRODUCTION

Interfaces between thin metal layers and semiconductors are used in optical detectors, solar cells [1] and chemical sensors [2-3]. The transport properties of such Schottky diodes and the dependence of the transport parameters on preparation are essential importance for the device performance. Metal-semiconductor interfaces may be characterized by photoelectrical and current-voltage ($I - V$) measurements [4-5].

Due to the technological importance of Schottky barrier diodes, a full understanding of the nature of their electrical characteristics is of greater interest [6-7]. Analysis of the current-voltage ($I-V$) characteristics of the Schottky barrier measured only at room temperature does not give detailed information about the conduction process and the nature of barrier formation at the metal-semiconductor (MS) interface. The temperature dependence of the $I-V$ characteristics allows us to understand different aspects of the conduction mechanism.

Detailed knowledge of the conduction process involved is essential to extracting the barrier parameters, namely, the barrier height and ideality factor. Analysis of the $I-V$ characteristics of SBDs based on thermionic emission theory usually reveals an abnormal decrease in the BH and an increase in the ideality factor with a decrease in temperature [8-9]. This abnormal behavior of the BH and ideality factor [8-9] have been successfully explained on the basis of a TE mechanism with Gaussian distribution of the BHs by some studies.

In this report, the $I-V$ characteristics of the Ag/n-GaAs SBHs were measured in the temperature range of 140-300 K. The temperature dependence of the barrier height and ideality factor is discussed using TE theory with a Gaussian distribution of the barrier heights around a mean value due to BH inhomogeneities prevailing at the metal-semiconductor interface.

EXPERIMENTAL

Before the fabrication the n-GaAs wafers were chemically cleaned by methanol and acetone and then

rinsed in deionized water. For the oxide present on the semiconductor, the samples were etched by $\text{H}_2\text{O}:\text{HCl}(1:1)$ solution. Then rinsed deionized water and finally samples were blown dry with nitrogen gas. After cleaning, for ohmic contact fabrication the samples were placed into the electron beam deposition system. The metal layers Ni ($\sim 10\text{nm}$)/AuGe($\sim 200\text{nm}$)/Au (300nm) were evaporated at a pressure of $\sim 5 \times 10^{-6}$ torr on the backside of the samples. The samples were then annealed in a furnace for 5 minutes at 450°C under N_2 gas atmosphere. For Schottky barrier diode fabrication Al and Ag metals were evaporated through a metal contact mask to give dots 2mm diameter and $\sim 150\text{nm}$ thick.

RESULT AND DISCUSSION

The electrical characterizations of the device were obtained through current-voltage ($I-V$) measurements in the temperature range of 140-300 K. $I-V$ characteristics of the Ag/n-GaAs Schottky barrier diode at several temperatures are shown in Fig.1.

The current through a Schottky barrier diode at a forward bias V based on the thermionic emission theory is given by the relation [10],

$$I = I_0 \exp\left(\frac{qV}{nkT}\right) \left[1 - \exp\left(-\frac{qV}{kT}\right)\right] \quad (1)$$

$$I_0 = AA^*T^2 \exp\left(-\frac{q\phi_{B0}}{kT}\right) \quad (2)$$

where V is the forward bias voltage, T is the absolute temperature, q is the electron charge, k is the Boltzmann constant, A is the effective diode area, $A^* = 4\pi qm^*k^2/h^3$ is the effective Richardson constant of $8,16 \text{ A/cm}^2\text{K}^2$ for n type GaAs, ϕ_{B0} is the zero bias apparent barrier height (BH) and n is the ideality factor. The ideality factor is calculated from the slope of the linear region of the forward bias $\ln I-V$ plot and can be written from Eq.(1) as

$$n = \frac{q}{kT} \left(\frac{dV}{d(\ln I)} \right) \quad (3)$$

The zero bias barrier height ϕ_{bo} is determined from extrapolated I_0 , and is given by

$$\phi_{bo} = \frac{kT}{q} \ln \left(\frac{AA^* T^2}{I_0} \right) \quad (4)$$

The experimental values of ϕ_{bo} and n were determined from intercepts and slopes of the forward bias $\ln I$ versus V plot of each temperature, respectively.

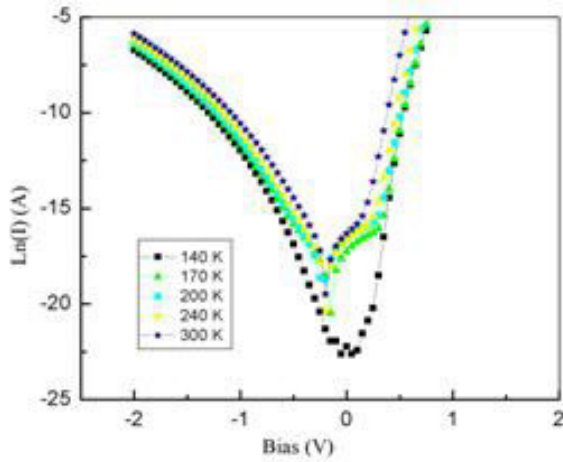


Fig.1. Experimental current-voltage characteristics of Ag/n-GaAs Schottky barrier diode at various temperatures where I_0 is the saturation current derived from the straight line intercept of $\ln I$ at $V=0$ and is given by.

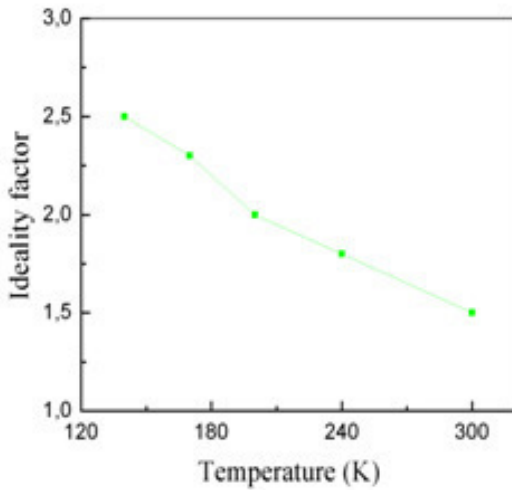


Fig.2. Temperature dependence of the ideality factor for Ag/n-GaAs Schottky diode in the range 140-300 K.

The ϕ_{bo} and n were found to be a strong function of temperature. The ideality factor n was found to increase, while the ϕ_{bo} decrease with decreasing temperature as can be seen in Figs. 2 and 3. ($n=2,5$ and $\phi_{bo}=0,43$ eV at 140 K, $n=1,5$ and $\phi_{bo}=0,65$ eV at 300K)

As explained in [11-13], once current transport across the metal-semiconductor (MS) interface is a temperature-activated process; the electrons at low temperatures are able to surmount the lower barriers and therefore current transport will be

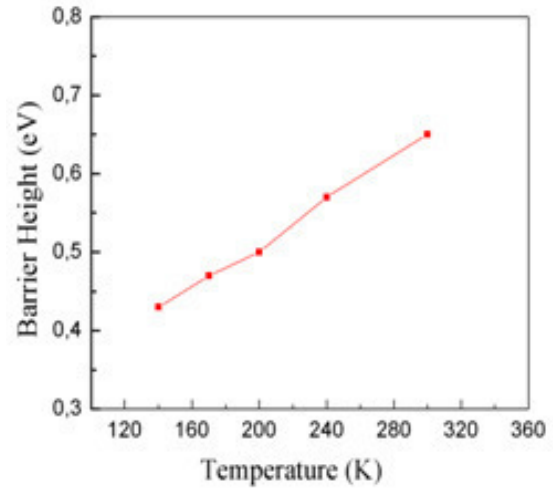


Fig.3. Temperature dependence of the zero-bias apparent barrier height for Ag/n-GaAs Schottky diode

dominated by current owing through the patches of lower Schottky barrier height and a larger ideality factor. As a result, the dominant barrier height will increase with the temperature and bias voltage. An apparent increase in the ideality factor and a decrease in the barrier height at low temperatures are possibly caused by other effects such as inhomogeneities of thickness and non-uniformity of the interfacial charged. This gives rise to an extra current such that the overall characteristics still remain consistent with the TE process[14]. This result is attributed to inhomogeneous interfaces and barrier heights because of a linear relationship between the barrier height and ideality factor.

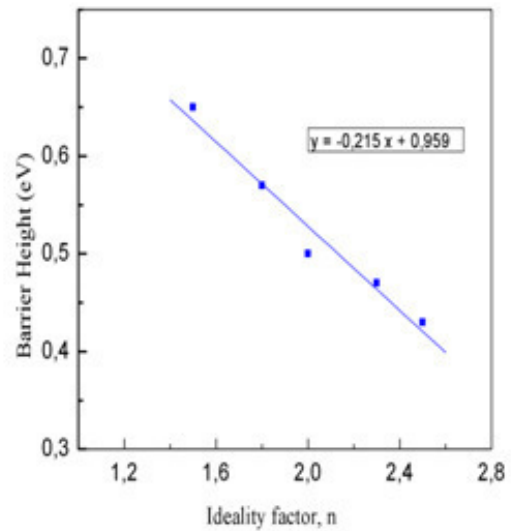


Fig.4. Zero-bias apparent barrier height vs. ideality factor of a Ag/n-GaAs Schottky diode at different temperatures.

Figure 4 shows a plot of the experimental BH versus the ideality factor for various temperatures. As can be seen from Fig. 4, there is a linear relationship between the experimental effective barrier heights and the ideality factor of the Schottky contact that was explained by lateral inhomogeneities of the BHs in the Schottky diodes [13]. The extrapolation of the experimental BHs versus ideality factors plot to $n=1$ has given a homogeneous BH of approximately 0.74 eV. Thus, it can be said that the significant decrease of the zero-bias BH and increase of the ideality factor especially at low temperature are possibly caused by the barrier inhomogeneities.

The Richardson constant is usually determined from the intercept of the $\ln(I_0/T^2)$ versus $1000/T$ plot. Figure 5 shows the conventional energy variation of $\ln(I_0/T^2)$ against $1000/T$. The non-linearity of the $\ln(I_0/T^2)$ versus $1/T$ plot is caused by the temperature dependence of the barrier height and ideality factor.

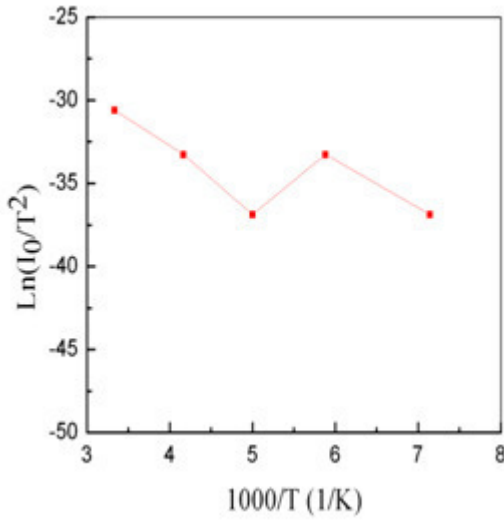


Fig.5. Richardson plot of the $\ln(I_0/T^2)$ versus $1000/T$ for Ag/n-GaAs Schottky barrier diode.

In order to explain the abnormal behavior between the theoretical and experimental values of Richardson constant, it is assumed that the distribution of the barrier heights is a Gaussian distribution of the barrier heights with a mean value ϕ_b and a standard deviation σ_s [8,15]

$$I(V) = A^* T^2 \exp \left[-\frac{q}{kT} \left(\phi_b - \frac{q\sigma_s^2}{2kT} \right) \right] \times \exp \left(\frac{qV}{n_{ap} kT} \right) \exp \left[1 - \exp \left(-\frac{qV}{kT} \right) \right] \quad (5)$$

with

$$I_0 = AA^* T^2 \exp \left(\frac{q\phi_{ap}}{kT} \right) \quad (6)$$

where n_{ap} and ϕ_{ap} are the apparent ideality factor and apparent barrier height at zero bias, respectively, and are given by

$$\phi_{ap} = \phi_{b0}(T=0) - \frac{q\sigma_{s0}^2}{2kT} \quad (7)$$

$$\left(\frac{1}{n_{ap}} - 1 \right) = \rho_2 - \frac{q\rho_3}{2kT} \quad (8)$$

The temperature dependence of σ_s is usually small and thus can be neglected.[9] However, it is assumed that σ_s and ϕ_b are linearly bias dependent on Gaussian parameters such that $\bar{\phi}_b = \bar{\phi}_{b0} + \rho_2 V$ and standard deviation $\sigma_s = \sigma_{s0} + \rho_3 V$, where ρ_2 and ρ_3 are voltage coefficients which may depend on T , and they quantify the voltage deformation of the BH distribution [9-17]

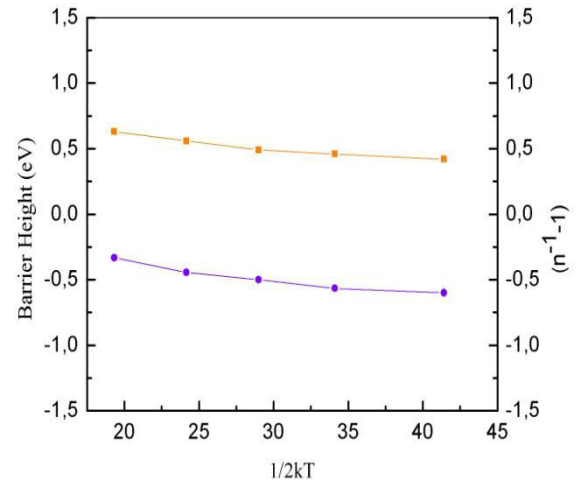


Fig.6. Zero bias apparent barrier height and ideality factor versus $1/2kT$ of Ag/n-GaAs Schottky barrier diode according to the Gaussian distribution of the barrier heights.

Fitting of the experimental data to Eqs. (2) and (3) gives ϕ_{ap} and n_{ap} , respectively, which should in turn obey Eqs. (7) and (8). Thus, the plot of ϕ_{ap} versus $1/2kT$ shown in Fig. 6 should be a straight line giving ϕ_{b0} and σ_{s0} from the vertical intercept and slope. As can be seen in Fig. 6, the values of $\phi_{b0} = 0.79$ eV and $\sigma_{s0} = 0.12$ V were obtained from the experimental ϕ_{ap} versus $1/2kT$ plot and in the same figure, the plot of n_{ap} versus $1/2kT$ should be a straight line that gives voltage coefficients ρ_2 and ρ_3 from the vertical intercept and slope, respectively. The values of $\rho_2 = 0.48$ V and $\rho_3 = 0.027$ V were obtained from the experimental n_{ap} versus $1/2kT$ plot. By comparing the ϕ_{b0} and σ_{s0} parameters, it is seen that the standard deviation which is a measure of the barrier homogeneity is 12% of the mean barrier height. Since the lower value of σ_{s0} corresponds to a more homogeneous barrier height, this result indicates that the Ag/n-GaAs device has larger inhomogeneities at the interface. This inhomogeneity and potential fluctuations dramatically affect low temperature I-V characteristics.

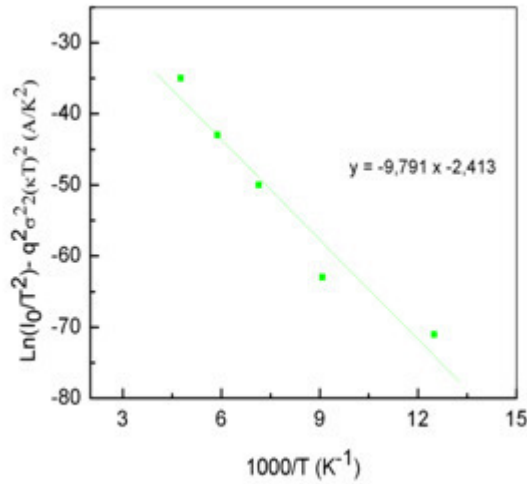


Fig.7. Modified Richardson $\ln(I_0/T^2) - q^2\sigma_0^2/2(kT)^2$ versus $1000/T$ plot for Ag/n-GaAs Schottky barrier diode according to the Gaussian distribution of the barrier heights.

The conventional Richardson plot is now modified by combining with Eqs. (6) and (7) in the following:

$$\ln\left(\frac{I_0}{T^2}\right) - \left(\frac{q^2\sigma_0^2}{2k^2T^2}\right) = \ln(AA^*) - \frac{q\phi_{b0}}{kT} \quad (9)$$

The modified $\ln(I_0/T^2) - (q^2\sigma_0^2/2k^2T^2)$ versus $1000/T$ plot, given in Fig. 7, should give a straight line with the intercept at the ordinate determining A^* . As shown in

Fig.7, the modified Richardson plot gives as $A^* = 3,51 \text{ A/cm}^2\text{K}^2$, without using the temperature coefficient of the barrier heights. It can be seen that the value of the modified Richardson constant $A^* = 3,51 \text{ A/cm}^2\text{K}^2$ is in closer agreement with the theoretical value of $A^* = 8,16 \text{ A/cm}^2\text{K}^2$.

CONCLUSION

The current-voltage characteristics of Ag/n-GaAs Schottky barrier diodes were measured in the temperature range of 140

-300 K. It was observed that while the zero-bias barrier height ϕ_{b0} decrease, the ideality factor n increases with a decrease in temperature. The characteristics of the structure have been interpreted on the basis of the assumption of a Gaussian distribution of barrier heights due to barrier height inhomogeneities that prevail at the interface. It was noted that barrier inhomogeneities at the interface cause deviation in the zero-bias barrier height and ideality factor at low temperatures. The inhomogeneities can be described by the Gaussian distribution of the barrier heights with a mean barrier height $\phi_{b0} = 0,79 \text{ eV}$ and standard deviation $\sigma_0 = 0,12 \text{ V}$. The experimental results of σ_{ap} and n_{ap} fit very well with the theoretical calculations related to the Gaussian distribution of σ_{ap} and n_{ap} . The Richardson constant obtained as $A^* = 3,51 \text{ A/cm}^2\text{K}^2$, by means of the modified Richardson plot. This value of the Richardson constant is in close agreement with the theoretical value of $8,16 \text{ A/cm}^2\text{K}^2$.

- [1] S.M. Sze. Physics of Semiconductor Devices, 2nd ed. (Willey, New York, 1981).
- [2] H. Nienhaus, H.S. Bergh, B. Gergen, A. Majumdar, W.H. Weinberg, and E.W. McFarland. Phys. Rev. Lett. 82, 446 (1999).
- [3] W. Göpel and K.D. Schierbaum, in Sensors, edited by W. Göpel, J. Hesse, and J.N. Zemel (VCH, Weinheim, 1991) Vol.2, p.429ff.
- [4] B.B. Kuliev, B. Lalavich, M. Yousuf, and D.M. Safarov. Sov. Phys.Semicon. 17, 875(1983).
- [5] M. Prietsch. Phys. Rep. 253,163 (1995).
- [6] R.T. Tung. Mater. Sci. Eng. R35, 1 (2001).
- [7] S. Zhu, R.L. Van Meirhaeghe, C. Detavernier, G. P. Ru, B. Z. Li and F. Cardon. Solid-State Commun. 112, 611 (1999).
- [8] Y.P. Song, R.L. Van Meirhaeghe, W.H. Laere and F. Cardon. Solid-State Electron. 29, 633 (1986).
- [9] S. Zhu, R. L. Van Meirhaeghe, C. Detavernier, F. Cardon, G. P. Ru, X. P. Qu and B. Z. Li. Solid-State Electron. 44, 663 (2000).
- [10] E.H. Rhoderick and R.H. Williams. Metal{Semiconductor Contacts (Clarendon Press, Oxford, 1988).
- [11] Zs. J. Horva'th. Solid-State Electron. 39, 176 (1996).
- [12] S. Karatas, S. Altindal, A. Turut and A. Ozmen. Appl. Surf. Sci. 217, 250 (2003).
- [13] R.T. Tung. Phys. Rev. B 45, 13509 (1992).
- [14] S. Chand and J. Kumar. Semicond. Sci. Technol. 10, 1680 (1995).
- [15] J.H. Werner and H.H. Güttler. J. Appl. Phys., 69, 1522 (1991)

Received:15.03.2018

MECHANISM OF OPTICAL VORTEX GENERATION FROM SELF-ASSEMBLED TFCD ARRAY IN SMECTIC LC AND TFCD APPLICATION TO OPTICAL DEVICES

K. KÄLÄNTÄR

*Japan Global Optical Solutions, R&D Center, 2-50-9 Sanda-Cho,
Hachi-Ouji-Shi, Tokyo 193-0832, Japan*

The smectic liquid crystal (SmLC) is used to fabricate an array of self-assembled defects in which each has a spindle torus structure. Each defect is a toroidal focal conic domain (TFCD) with an optical vortex generation function. The mechanism of optical vortex generation in TFCD was studied in details and found that a TFCD is an integration of radial graded-index (GRIN) layers and axially GRIN shells. The light focusing and polarization transformation characteristics of the GRIN layers are formulated to realize a single millimetric optical device with vortex generation function.

Keywords: Optical vortex, Focal Conic Defect, Toroidal FCD, Smectic LC, Graded Index, GRIN

PACS: 64.70; 61.46; 61.30

1. INTRODUCTION

Optical vortex or phase singularity generation has been found to be one of the challengeable topics in the integrated optics [1]. The space-variant polarization, (transversely nonuniform), and dislocations such as optical vortices (Fig.1) are studied and applied to high resolution microscopy development, optical manipulation, quantum computing, and astronomical imaging. Single optical vortex generating devices have been reported in recent years. However, the requirements for an array of optical vortices in large size have also been increasing for applications such as opto-mechanical pumping, multichannel optical communicating, quantum computing, and astronomical holography.

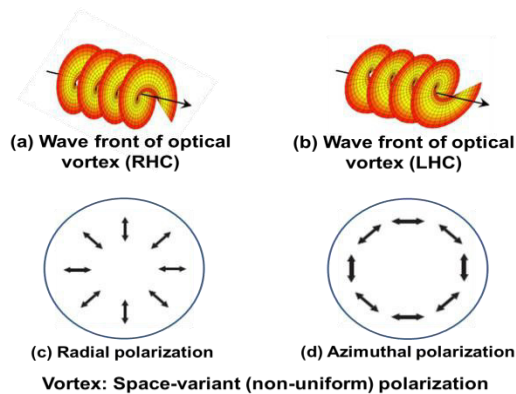


Fig. 1. Helical wave fronts or optical vortices and radial / azimuthal polarizations

Optical beam with helical wave front, i.e., an optical vortex; (a) right hand circular (RHC) wave front, (b) left hand circular (LHC) wave front. Space-variant polarizations; (c) radial polarization. (d) azimuthal polarization.

Variety of methods have been developed to generate optical vortex arrays, such as electron-beam, lithography, photo-polymerization, and direct laser writing of radial birefringence. Among these methods liquid crystals (LCs) have been used to generate optical vortex arrays because of quick and simple stabilization of molecular ordering and structure. Recent studies show the realization of arrays of microscopic optical vortex generators using cholesteric or nematic LCs [2].

However the mechanism of optical generation in toroidal focal conic defect (TFCD) has not been reported yet. In this study, the vortex array generation was analyzed and the light field propagation was clarified in a single smectic LC (SmLC) TFCD [3]-[4]. The analysis results are reflected on fabrication of a novel millimeter order single optical vortex generator, namely a novel optical device.

2. STRUCTURING TFCD ARRAY

Among the aforementioned methods SmLC is used for TFCD fabrication because of quick and simple stabilization of molecular ordering and structure. To fabricate TFCDs, the crystalline LC material is deposited on the substrate, and the substrate is heated to temperature exceeding 65 °C, i.e., corresponding to the isotropic phase of the LC. The glass substrate is cooled at a rate of -5°C/min to form the smectic A phase. The TFCDs are self-assembled on the substrate.

In this study the vortex array generation was analyzed in a single torus SmLC defect to clarify the behavior of light field propagation in the TFCD.

3. TFCD STRUCTURE

In the aforementioned fabrication method the SmLC defects are self-assembled in a large number (about 1000 TFCDs). Each defect is a TFCD that generates optical vortex. The fabricated feature size is about 35 μm.

The geometry of a TFCD is shown in a cylindrical coordinate systems in Fig.2. A TFCD is found to be a spindle torus as shown the cross section in Fig.3. The TFCD cross-section is defined as $B_1C_1C_2AB_2$ in Fig.3. The status of SmLC directors are shown at point B_1 and C_1 in gray colors. The bottom director is in ρ -direction (or y-axis) in cylindrical coordinate system. These directors are distributed along ρ -axis, i.e., from side walls (B_1B_2 or C_1C_2) toward the center of the TFCD. The extra ordinary refractive index (director laid on the bottom of the TFCD along ρ) is $n_e[n_e(\rho, \pi/2)]$ for propagated light wave along the z-axis ($\theta = \pi/2$). The directors are standing up gradually with decrease in zenith angle, and finally are vertical along the B_1B_2 or C_1C_2 . The refractive index (director standing up along the wall of the TFCD) is $n_o[n_o(\rho_{max}/2, 0)]$ for the propagating light along the z-axis. The refractive index difference along the vertical axis of

TFCD (z-axis) at an arbitrary ρ is given by the following equation,

$$\Delta n(\rho, \theta) = \frac{n_o\left(\frac{\rho_{\max}}{2}, 0\right) \times n_e\left(\rho, \frac{\pi}{2}\right)}{\sqrt{n_e^2\left(\rho, \frac{\pi}{2}\right) \times \cos^2 \theta + n_o^2\left(\frac{\rho_{\max}}{2}, 0\right) \times \sin^2 \theta}} - n_o\left(\frac{\rho_{\max}}{2}, 0\right) \quad (1)$$

The first term is the effective local refractive index of the extraordinary wave. The zenith angle θ is given by

$$\theta = \frac{\pi}{2} - \tan^{-1}\left(\frac{z}{\frac{\rho_{\max}}{2} - \rho}\right) \quad (2)$$

Since the directors are perpendicular to the radius of the spindle torus, i.e., the front surface of the TFCD, there is small differences between the TFCD height at the center ($\rho=0$) and that at the side wall boundaries. Because a TFCD is a part of torus, the aspect ratio is 1:1, i.e., the diameter of the TFCD is equal to its height (Fig.3). The height of TFCD (on the front surface, z_s) at an arbitrary ρ is given

$$by z_s(\rho) = \sqrt{\rho_{\max}^2 - (\rho_{\max}/2 - \rho)^2}. \quad (3)$$

Using the above equations, the normalized refractive index difference can be shown by the following equation.

$$\Delta n(\rho, \theta) / \Delta n_{\max} \approx \sin^2(\rho, \theta) \quad (4)$$

The TFCD has a funnel shape front surface. The height variation, i.e., Eq.(3) is shown in Fig.4.

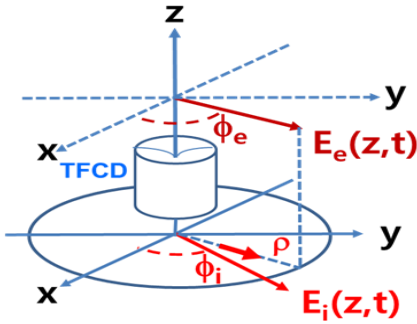


Fig.2 Geometry of a TFCD

Cylindrical coordinate system is used to show the polarization transformation of the TFCD. $E_i(z, t)$ at azimuth angle of ϕ_i is the amplitude of the incident electric field and $E_e(z, t)$ at ϕ_e is the emergent electric field.

The normalized refractive index difference causes phase change of the propagating light. The normalized refractive index has a $\sin^2(\rho, \theta)$ variation. Therefore, the squared *sine* is used for the normalized refractive index variation and for calculating the phase change.

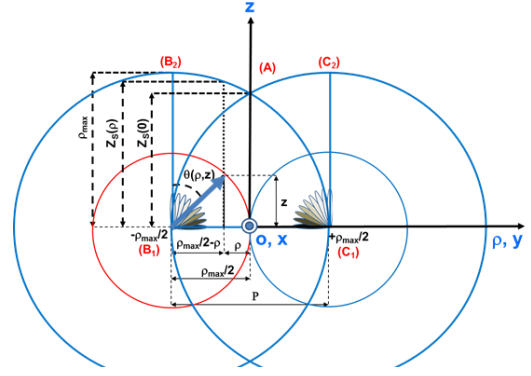


Fig.3. TFCD structure

Outer overlapped circles are the cross section of a spindle torus. The rectangle of $B_1C_1C_2B_2$ is the cross section of the TFCD.

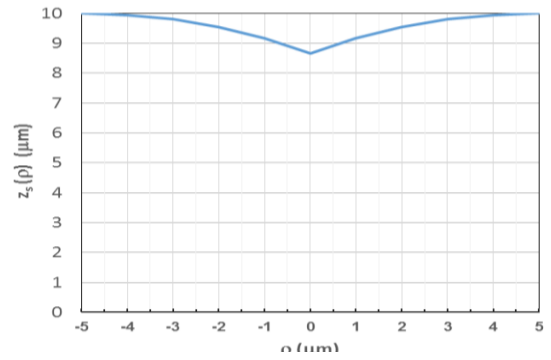


Fig.4. TFCD's height vs. radius

Front surface of TFCD has a shape of funnel. The cross section of the funnel is plotted versus the radius of the TFCD (cylindrical body).

The normalized phase is plotted versus ρ and z as in Fig.5.

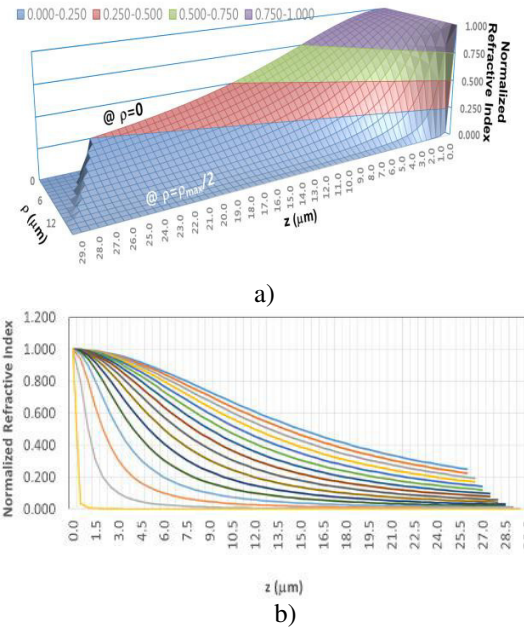


Fig.5. Parabolic refractive index distribution

On axis refractive index changes from n_e to n_o . (a)

Normalized refractive index along ρ and z in the TFCD.

(b) Normalized refractive index along z-axis.

The refractive index on the bottom of the TFCD is n_e that is decreasing along the z -axis.

4. PHASE RETARDATION

The phase retardation is calculated in terms of wavelength, thickness and birefringence distribution of optical media. Because the direction of molecular director varies along the propagation axis (z -axis), the birefringence should be integrated over the propagation path to get averaged effective birefringence. The resultant averaged phase retardation at an arbitrary position (ρ_0) is given by the following equation

$$\Delta\Phi(\rho_0, z_s) = \frac{2\pi\Delta n_{\max}}{\lambda} \int_0^{z_s} \sin^2 \left[\frac{\pi}{2} - \tan^{-1} \left(\frac{z}{\frac{\rho_{\max}}{2} - \rho_0} \right) \right] dz \quad (5)$$

Eq.(5) shows the variation of the phase along the z -axis as well as the ρ -axis. This is due to refractive index change along the z -axis and ρ -axis that is shown schematically in Fig.6.

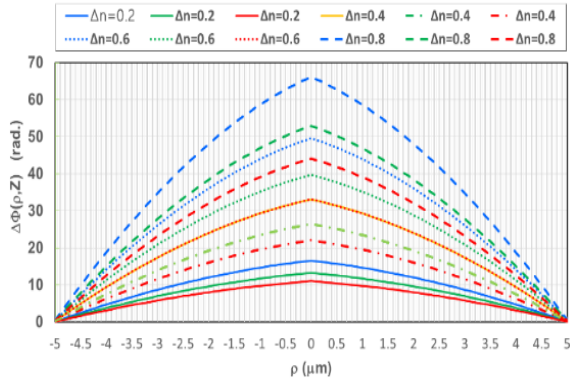


Fig.6. Phase retardation along the z -axis
Refractive index variation along z -axis at arbitrary radius results in phase retardation $[\approx \sin^2(\rho, \theta)]$ along the z -axis that changes with wavelength. The blue, green and red colors represents the wavelengths of 400, 500 and 600 nm. Two graphs have been overlapped.

The circular polarized light transmitted through TFCD has a phase difference with respect to original incident beam and has an intensity given in Eq.(6) as below. Here K is the fraction of the original field ($K \leq 1$). Final polarization distribution of output field modulated by TFCD is characterized by Jones matrix of the optical system:

$$\begin{aligned} |E_{\text{out}}(\rho, \phi, z)|^2 = & \left[\cos(m\phi) * \sin \left[\frac{\Delta\Phi(\rho, z)}{2} \right] \right]^2 + \\ & + \left[\sin(m\phi) * \sin \left[\frac{\Delta\Phi(\rho, z)}{2} \right] \right]^2 + \\ & \cos \left[\frac{\Delta\Phi(\rho, z)}{2} \right] K \end{aligned} \quad (6)$$

Here, m is a topological charge that designates the number of cyclic changes in polarization state or phase along a closed path surrounding the center of the beam, defined as $m=2q$. This parameter is an integer value when the medium is rotationally symmetric. The topological charge (m) is twice the topological strength (q).

Substituting these parameters into the Jones matrix, the TFCD's Jones matrix can be obtained. Using the Eq.(6), the coronagraphs of the transmitted light wave and vortices can be obtained on the TFCDs. The term of squared *cosine* changes with azimuth angle, resulting bright and dark zones. The term of squared *sine* changes with phase retardation in which the retardation itself changes with ρ and z or θ . The multiplication of these two functions results in a coronagraph (not shown) in which the zero-intensity regions; the dark rings and dark Maltese cross along the radial and azimuthal directions. The bright and dark regions are the spatially polarization changing areas, presenting vortices.

5. TFCD AS GRIN LAYERS AND GRIN SHELLS

As explained the refractive index of a TFCD in Eq.(4), a TFCD can be assumed as an integration of graded-index (GRIN) layers (in ρ -direction) (Fig.7(a)) that have parabolic refractive index distributions with different on-axis refractive indices and focusing parametric. The refractive index distribution of a TFCD is shown in Fig.7(b).

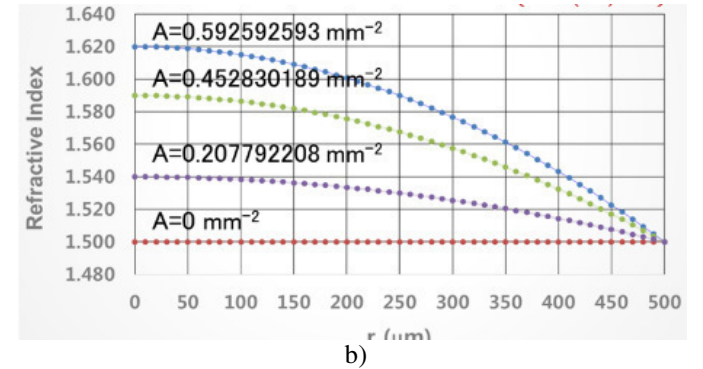
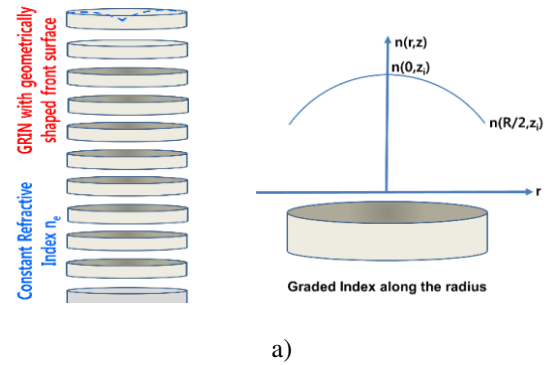


Fig.7. Parabolic refractive index distribution (Eq.7)

a) On axis refractive index changes from n_e to n_0 . The bottom and side wall refractive indices, n_e and n_0 , are constant ($r \cong \rho$). Focusing parameter (A) is different for each layer.

In addition the refractive index change can be extended to vertical direction and assumed that a TFCD is an integration of GRIN shells as shown schematically the structure in Fig.8 (a) and (b).

Each layer (disc shape) has a parabolic refractive index distribution that has a light focusing characteristic. The parabolic refractive index is given by the following equation in which the focusing parameter is given by “ A ”.

$$n_G(\rho) = n_G(0) \left\{ 1 - \left(\sqrt{\frac{A}{2}} \right)^2 \rho^2 \right\} \quad (7)$$

Since two types of light rays exist in a medium with parabolic refractive index distribution, Eq.(7) is a common refractive index distribution for both meridional and helical rays.

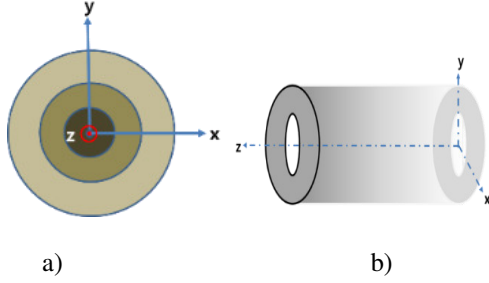


Fig.8 Parabolic refractive index distribution for each layer along z axis.

On axis refractive index changes from n_e to side wall refractive index, n_o . (a) Top view of the shells, (b) Perspective of a single shell.

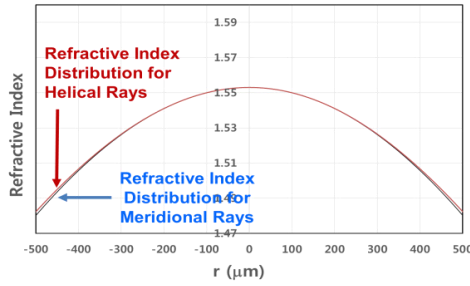


Fig.9. Parabolic refractive index distribution for each TFCD layer. The distributions for helical and meridional rays.

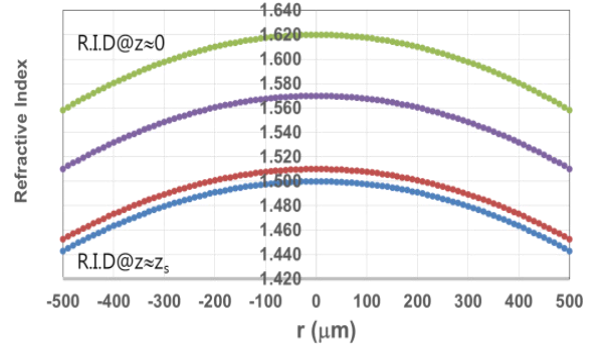


Fig.10. Parabolic refractive index distribution for each layer
The center refractive index is different for each layer and changes with z as well as r ($r \equiv \rho$).

The difference in the optimized refractive index distributions are shown in Fig.9. The refractive index distributions for the layers are shown in Fig.10.

6. CONCLUSIONS

The mechanism of optical vortices generation from toroidal focal conic domains that are self-aligned in SmLC was studied to realize a functional optical device in millimetric size to generate a single or multi-phase singularities. The refractive index distribution and the phase retardation for a single TFCD were formalized. The Jones matrix of the TFCD for vortex generation and layer light transmission were developed. The structure of a single TFCD was found to be an integration of graded-index horizontal layers (in ρ -direction) or vertical shells (in z -direction). The analogue integration of thin GRIN layers can lead to realization of a single TFCD for optical vortex generation.

- [1] B.S. Son, S.J. Kim, Y.H. Kim, K. Käläntär, H.M Kim, H.S. Jeong, S.Q. Choi, J.H. Shin, H.T. Jung, and Y.H. Lee: "Optical vortex arrays from smectic liquid Crystals," Vol. 22, No. 4/OE.22.004699 (Feb.2014).
- [2] R. Barboza, U. Bortolozzo, G. Assanto, E. Vidal-Henriquez, M. G. Clerc, and S. Residori. "Harnessing optical vortex lattices in nematic liquid crystals," Phys. Rev. Lett. 111(9), 093902 (2013).
- [3] D.K. Yoon, M.C. Choi, Y.H. Kim, M.W. Kim,

- O.D. Lavrentovich, H.T. Jung. "Internal structure visualization and lithographic use of periodic toroidal holes in liquid crystals," Nature Materials 6, 866 - 870 (October 2007).
- [4] Y.H. Kim, D.K. Yoon, H.S. Jeong, H.T. Jung. "Self-assembled periodic liquid crystal defects array for soft lithographic template," Soft Matter 6 (7), 1426-1431, 2010.

Received: 29.03.2018

CONTENTS

1.	The structure and physical parameters of chalcogenide glass-like semiconductors of system As- Ge – Se S.I. Mekhtiyeva, A.I. Isayev, R.I. Alekberov, H.I. Mamedova	3
2.	New method of decrease of transit-time broadening of spectral resonances Azad Ch. Izmailov	10
3.	The analysis of dielectric absorption dispersion of glycine water solution S.T. Azizov, O.A. Aliyev	14
4.	Investigation of semipolar GaN templates and InGaN multiplies quantum wells grown by HVPE and MOVPE Sevda Abdullayeva, Gulnaz Gahramanova, Rasim Jabbarov, Cesare Frigeri	17
5.	Magnetoresistive properties of Dirac semimetal Cd_3As_2 ferromagnetic semiconductor at high pressure M.M. Gadjaliev, I.A. Saipulaeva, A.G. Alibekov, A.Yu. Mollaev, V.S. Zakhvalinsky, S.F. Marenkin, T.N. Efendieva	23
6.	Method to determine the inverted layer M.M. Gadjaliev, Z.SH. Pirmagomedov, T.N. Efendieva, L.A. Saypulaeva	27
7.	Modelling of component axial concentration profiles in InSb-GaSb solid solution single crystals grown by zone melting method using InSb and GaSb seeds Z.M. Zakhrebekova, A.I. Alekperov, V.K. Kazimova, G.H. Ajdarov	29
8.	Electron structure of graphene based material Arzuman G. Gasanov, Azad A. Bayramov	33
9.	Electron mobility in $\text{Ge}_{1-x}\text{Si}_x$ ($0 \leq x \leq 0.13$) crystals complex doped by <Ga,Sb,Ni> impurities E.M. Islamzade, Z.A. Agamaliyev, G.H. Ajdarov	37
10.	High-plastic transition in thermoelements on GeTe- Co_2Ce eutectic base A.A. Magerramov, K.Sh. Kakhramanov, K.G. Khalilova	41
11.	Study of space structure of Dippu-AST5 molecule L.I. Veliyeva, E.Z. Aliyev	46
12.	Influence of fullerenes on dielectric and conductivity properties of liquid crystal MBBA T.D. Ibragimov, A.R. Imamaliyev, G.F. Ganizade	50
13.	The fluctuation conductivity in $\text{Bi}_{1.7}\text{Pb}_{0.3}\text{Sr}_2\text{Ca}_2\text{Cu}_3\text{O}_y$ V.M. Aliyev, R.I. Selim-zade, V.I. Eminova, S.Z. Damirova	56
14.	Temperature dependence of electrical characteristics of Ag/n-GaAs Schottky barrier diodes A.A. Asimov, A.M. Kerimova, Kh.N. Ahmedova, I.A. Nasibov	59
15.	Mechanism of optical vortex generation from self-assembled TFCD array in smectic LC and TFCD application to optical devices K. Kälántár	63